UNIVERSITY OF GENOVA

NATIONAL PHD PROGRAM IN ROBOTICS AND INTELLIGENT MACHINES

Design, Development and Characterization of Tactile Sensors Solutions in Multi-Modal Sensing Systems for Robot Self-Aware Control

by

Marco Staiano

Thesis submitted for the degree of *Doctor of Philosophy* (38° cycle)

2026

Prof. Giorgio Cannata — Supervisor

Dr. Francesco Grella — Co-supervisor

Prof. Antonio Sgorbissa — Head of the PhD program

Thesis Jury:

Prof. Adolfo Muñoz Orbañanos, *Universidad de Zaragoza* — External examiner

Dr. Ilze Aulika, *Institute of Solid State Physics, University of Latvia* — External examiner

Prof. Enrico Simetti, *Universita' Degli Studi di Genova* — Internal examiner

Dibris

Department of Informatics, Bioengineering, Robotics and Systems Engineering

I-RIM

Italian Institute of Robotics and Intelligent Machines

To Giuseppe, Lucia, Chiara, Mattia and my beloved family:
A fernut e chiovr.

Declaration

I hereby declare that except where specific reference is made to the work of others, the contents of this dissertation are original and have not been submitted in whole or in part for consideration for any other degree or qualification in this, or any other university. This dissertation is my own work and contains nothing which is the outcome of work done in collaboration with others, except as specified in the text and Acknowledgements. This dissertation contains fewer than 65,000 words including appendices, bibliography, footnotes, tables and equations and has fewer than 150 figures.

Marco Staiano
April 2026

Acknowledgements

Three years of my life has been dedicated to this PhD with moments of joy and dark times, but at the end i did it, with the support of many marvelous people, friends and in particular my family.
First of all, I would like to thank my supervisor Giorgio to accept my proposal and support my ideas through these years, and to his kind guide not only in the lab, but also in ordinary life. I grow up on how to be independent, how to solve and approach problems and how to build a solid scientific mind.
My gratitude goes also to my supervisors and team at RISE in Norrköping: Peter, Lars, Darius and Jan, but also Rob, Valerio and Astrid, and all the great people met in RISE. They helped me in my period abroad making the distance from home less sad and tragic, by rising a light in the dark winter Sweden times.
Another thank goes to my supervisors at ERMIT Emanuele and Simone and all the people in the company for their kindness and support.
From now on i will switch in Italian.
Questo periodo non e' stato facile da affrontare. Ci sono state sfide difficili in laboratorio e complicazioni anche fuori dal laboratorio, periodi in cui avrei voluto mollare. Ma questo percorso mi ha anche regalato momenti di soddifazione e ricordi indelebili.
Soddisfazioni condivise con i ragazzi del MACLAB. inizialmente con solo Francesco e Francesco, ma poi anche con Alessandro, Simone, Pedro, Parisa e Danial. Il vostro supporto e' stato fondamentale per questo PhD e l'aiuto e l'affetto che mi avete mostrato hanno reso tutto molto piu' leggero. E per questo ringrazio anche i vecchi membri del MACLAB come Alessandro e Perla, ma soprattutto le persone e i professori degli altri laboratori in Universita': Andre, Luca, Alle, Zoe, Titti, Giulia, Marco, Francesca, Alice, Samu, Enzo, Juri, Fra Wander, Omotoye, Gio, Michele, Gio Mottola, Lucrezia, Carmine, Antonio ed Enrico.
Un ringraziamento speciale va a coloro che hanno creato altri momenti indelebili: Laura e Lorenzo. Un grazie non puo' bastare, senza di voi probabilmente non avrei avuto modo di realizzare questo traguardo. Le serate, le camminate e i viaggi condivisi sono state gioia e rimarranno sempre gioia, sperando sempre di rivederci ogni tanto.

Ringrazio anche chi fuori dall'Uni si e' intrattenuto per birre e cene: Jacopo e di nuovo Zoe, Serena, Gianluca e Merilu'.
Speravo di essere breve ma i ringraziamenti non sono finiti.
Un immenso grazie ai miei amici d'infanzia sempre vicini ad ogni mio passo: Enri, Pino, Anto, Magno, Eddy, Chri, Coro, Teo, Giuli, Noe, Fre, Michi, Ele, Tizi, Bella e Tulli. Ma anche ai loro +1 che si sentiranno minimizzati, ma Marghe, Gio, Giuli, Noe state tranquille.
Menzione speciale anche per il gruppo salottino Ari e Camilla che fanno parte anche dell'ultimo gruppo cammini con Alessio, Ale e Benny.
Inoltre ringrazio anche il gruppo di beach storico che ha reso le estati leggere e indimenticabili: Liam, Fala, Frizzy, Lele, Gimmi, Ello, Jack, Vanno, Azzu e ancora Ari ed Ale.
A rendere tutto speciale ci sono state anche le amiche di sempre: Giada, Giuli e Ceci.
Menzione anche per coloro che mi hanno supportato sempre anche da lontano: Taru, Ceci, Luci, Spiedo e Fede.
Sono quasi alla fine. Ultimi ringraziamenti.
In questo ultimi mesi mi hanno spronato per l'ultimo passo anche i miei nuovi colleghi di lavoro: Ema, Lisa, Enri, Michi, Zag, Pola, Ani, Marci e Luca.
Vorrei anche ringraziare colei che ho conosciuto negli ultimi mesi di dottorato e che mi ha spinto a non mollare fino all'ultimo giorno, grazie Alessia per cio' che mi stai dando e per quello che verra'.
Infine il tutto e' stato possibile con il supporto amorevole e senza giudizio della mia famiglia a cui dedico tutto e a cui saro' per sempre grato, dal nonno e le nonne da lassu', alle zie, agli zii e i cugini.
Grazie mamma Lucia, papa' Giuseppe, Chiara e Mattia.
Questo e' per tutti quelli che ci sono stati e anche per quelli che sono passati e hanno contribuito al mio vivere.
E questo e' anche un po' per me.
Fine.

Abstract

This doctoral research addresses the development of scalable, printable, and mechanically compliant capacitive tactile sensing solutions for robot self-aware control and large-area robotic skin integration. As robots increasingly operate in close proximity to humans, tactile sensing becomes a fundamental technology for safe physical interaction, compliant manipulation, and whole-body perception. However, significant challenges remain in terms of fabrication scalability, sensitivity enhancement, communication bandwidth, and integration on curved and articulated robot geometries.

The thesis proposes and experimentally validates three complementary technological contributions.

First, multilayer capacitive tactile sensors based on vertically stacked architectures are introduced to enhance sensitivity and dynamic range without increasing the in-plane dimensions of the sensing element. Analytical modeling and finite element simulations demonstrate that vertical stacking systematically increases capacitance variation under applied pressure. Experimental results obtained through inkjet and screen-printing fabrication confirm a monotonic sensitivity improvement up to five stacked layers, validating the scalability of the approach while preserving compact taxel geometry.

Second, CySkin+ is presented as an evolution of an established distributed tactile architecture. The work introduces substrate optimization, improved fabrication strategies based on lamination and printing techniques, and the integration of an EtherCAT-based communication backbone. Experimental characterization confirms compliant sensitivity, repeatability, and robustness compared to the original CySkin design. The adoption of industrial real-time communication enables deterministic, synchronized, and scalable distributed acquisition, strengthening compatibility with industrial robotic control frameworks.

Third, PeSkin is introduced as a large-area tactile sensing solution based on screen-printed air-gap capacitive technology. The laminated PET–air-gap architecture demonstrates high low-force sensitivity (up to 5870 $fF/N \mid 57\ fF/kPa$), limited hysteresis (3.11 %), high repeatability (1.77 %), fast dynamic response (4.17 ms), and an effective dynamic range of approximately 15 $bits$. A cylindrical integration demonstrator composed of 12 patches

and 1728 taxels validates mechanical conformability, modular acquisition scalability, and real-time distributed tactile visualization over curved surfaces.

Overall, this thesis contributes a complete pipeline—from sensor architecture modeling and material selection to electronic readout design and system-level robotic integration—toward scalable and printable tactile skins. By exploiting vertical stacking, industrial communication protocols, and additive manufacturing techniques, the proposed solutions demonstrate that high-performance capacitive tactile sensing can be effectively integrated into distributed robotic platforms.

List of Publications

The following publications have been produced during the course of this doctoral research:

1. **M. Staiano**, G. Baldini, F. Grella, M. Frascio, P. Maiolino, and G. Cannata, **"Mathematical Model and Experimental Characterization of Vertically Stacked Capacitive Tactile Sensors,"** *IEEE Sensors Journal*, vol. 23, no. 18, pp. 21341–21354, 2023.

2. F. Giovinazzo, A. Perri, **M. Staiano**, F. Grella, M. Sartore, M. Adami, R. Galletti, and G. Cannata, **"Design, Implementation and Testing of an EtherCAT-based Network for Multi-Modal Distributed Sensing Architectures,"** in *Proc. IEEE 20th International Conference on Automation Science and Engineering (CASE)*, pp. 830–837, 2024.

3. F. Grella, F. Giovinazzo, **M. Staiano**, A. Albini, G. Cannata, and P. Maiolino, **"The ProxySkin Sensor: an Interactive Demo of a Multi-modal Large-area Network for Robotic Applications,"** *IEEE 41st International Conference on Robotics and Automation (ICRA EXPO)*, Yokohama, Japan, 2024.

Table of contents

List of figures

List of tables

Chapter 1

Overview

Robots in recent years have become crucial in industries. They have significantly cut down production costs, improved workers' safety, and highly enhanced overall efficiency.
In the beginning, robots have been deployed to handle severe and hazardous tasks such as heavy lifting, die casting, and welding. At this early stage, the machines followed rigid instructions with no awareness of their surroundings. The lack of sensors or feedback mechanisms led robots to perform repetitive motions inside fenced-off enclosures to prevent accidents. In this scenario workers were relieved from physically demanding efforts and secure from dangerous environments, enabling them to focus on tasks requiring skills and dexterity.
During the 1980s, With the advancements in electronics, mechanics and computer science, robots began to evolve rapidly. Due to the integration of different type of sensors - such as torque sensors and vision-based systems - robots were able to gather information about their current state and workspace. This allowed machines to operate faster and with reliable accuracy, handling autonomously entire production stages without human supervision. Although, robots were still confined in cells to ensure workers' safety.
In the early 2000s, with the rising of new technologies and tools such as Machine Learning (ML) and Artificial Intelligence (AI) robots have been pushed beyond repetitive work, reaching high levels of automation, complexity, reliability, and customization. Advanced sensors systems such as laser scanners and force detectors gave modern machines a limited sense of "sight" and "touch" allowing them to interact with objects, learn, adapt and make decision to optimize task performance. These are no longer *"Intelligent Machines"* confined to isolated robot cells but instead collaborate with humans on joint tasks, enhancing the flexibility, synergy, and the overall quality of the production process.

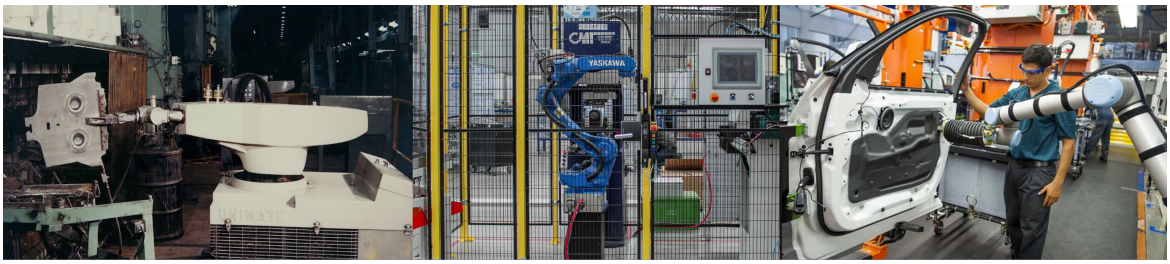

(a) (b) (c)

Figure 1.1 Evolution of robots in manufacturing: **(a)** The first "Unimate" used on an assembly line. It was installed at the General Motors plant in Trenton, New Jersey, in 1961 to unload a die-casting press.[1]; **(b)** YASKAWA Motoman robot confined in a cell[2]; **(c)** UR10e cobot, collaborating with an operator[3].

Nowadays, robots are not limited to factories but they are part of our daily activities to perform tasks in fields such as warehouse, healthcare, agriculture, and public spaces. In warehouses, autonomous robots manage inventory, transport goods, and facilitate deliveries. In healthcare, precision surgical robots like *da Vinci* enable minimally invasive procedures with extremely high accuracy. Social robots, such as Pepper and Lynx, provide company and cognitive stimulation for elders, while rehabilitation robots assist patients in physical therapy and recovery. In agriculture, drones and mobile robots inspect and analyze vineyard and farms. Robotic assistants are also deployed in airports, shopping malls, and hospitals to provide guidance, information, and customer support.
To efficiently and safely work in these dynamic and harsh environments, robots need to be equipped with advanced sensing devices and optimal control systems. This grants the machines to have self awareness in the workspace and proper reactions to external stimuli. This challenge is at the core of the Horizon Europe project Sestosenso, which aims to develop technologies for next-generation collaborative robots.
In this context, this dissertation presents the development of *PeSkin*, *CySkin+* and *multi-layer capacitive sensors (MLC)*, tactile technologies designed to cover small and large areas of a robot's body. This work will explore in details the fabrication, characterization and implementation of the technologies to demonstrate their relevant effectiveness and novelty.

[1] https://www.youtube.com/watch?v=-Xl2c91pWGc&ab_channel=TheHenryFord
[2] Robot from Yaskawa. https://www.motoman.com/en-us
[3] Cobots from Universal Robots. https://www.universal-robots.com/

1.1 Multi-Modal Sensing

As mentioned in the Overview, robots to operate efficiently and safely in harsh and dynamic environments need to rely on advanced sensing architectures. Thus, by leveraging various sensors - such as cameras, lidars, force-torque, proximity and tactile sensors - machines can autonomously react to unexpected events, learn and adapt to changing operating conditions, and anticipate the actions of other entities within the shared workspace. The integration of various type of sensors into a unified framework leads to a robust, seamless, cohesive sensing infrastructure that allows robots to perceive their surroundings more effectively. For instance, while cameras provide high-resolution spatial information, they may struggle under poor lighting conditions or occlusions; tactile or proximity sensors, on the other hand, offer reliable feedback during physical interaction or in close-range environments. By combining such modalities, robots can overcome the limitations of individual sensors, leading to improved perception accuracy, redundancy, and resilience in the face of uncertainty. Exploiting such technologies reduce robot setup times and costs and significantly increase the flexibility of the shop-floor configuration. The existing literature offers numerous solutions for distributed multi-modal sensing architectures. These examples showcase innovative approaches and practical implementations which demonstrate the benefit and versatility of such systems.
In *Mittendorfer and Cheng (2011)*, the authors design and develop HEX-O-SKIN, small hexagonal active tactile modules to approach multimodal whole-body-touch sensation for humanoid robots. These modules are small printed circuit boards (PCBs) equipped with MEMS accelerometers, optical reflective sensors for proximity and resistive temperature sensors. The functionality of the architecture is demonstrated in *Bergner et al. (2016)*; *Cheng et al. (2019)* and *Mittendorfer et al. (2015, 2013)*, but the size, rigidness and thickness of the modules do not allow to place the skin on any robot surface.
Zhou et al. (2024) introduce TacSuit. This multi-modal, modular, large-area skin for collaborative robots integrates pressure, proximity, acceleration and temperature sensors. TacSuit technology is similar to HEX-O-SKIN in dimensions and geometry, but to achieve conformity, scalability and easy integration on the robot surface, the sensing elements lay in custom-designed 3D printed capsules. TacSuit is integrated onto a humanoid robot and validated with different control strategies in safe human-robot interaction applications.

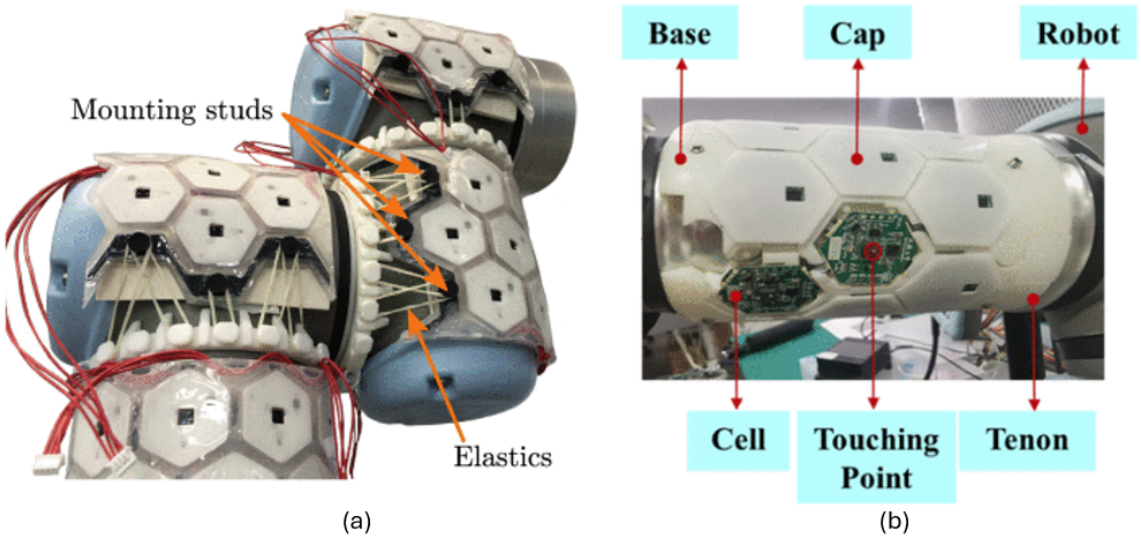

Figure 1.2 Examples of multi-modal distributed sensing architectures for robotic applications: **(a)** HEX-O-SKIN technology integrated on UR5 *(Cheng et al. (2019))*. **(b)** TacSuit technology equipped on robot arm *(Zhou et al. (2024))*.

Despite the advances in multi-modal sensing architectures, physical interaction between robots, humans, and the environment is often made through touch. Among the different sensing modalities, tactile sensing plays a central role in enabling safe human–robot interaction, contact detection, and manipulation tasks, as it provides direct and localized information during physical contact, even in visually occluded or cluttered environments.

Designing tactile sensing systems suitable for robotic applications, however, involves significant technological challenges. Tactile sensors must combine high sensitivity, wide dynamic range, fast response, mechanical robustness, and scalability over large and complex surfaces. These requirements have led to develop a wide variety of tactile sensing technologies, characterized by different transduction principles, materials, fabrication processes, and sensor architectures.

For this reason, the following section reviews the state of the art in tactile sensing technologies, with particular focus on capacitive tactile sensors, highlighting their performance characteristics and limitations in robotic skin applications.

1.2 Tactile Sensing Technologies

Tactile sensing technologies aim to provide robots with the ability to perceive physical interactions with the environment by measuring contact-related quantities such as normal and shear forces, pressure distributions, contact points, and, in some cases, material properties. This sensing modality is fundamental for tasks involving manipulation, grasp stability, collision detection, and safe human–robot interaction, where reliable perception must be maintained independently of lighting conditions or visual occlusions (*Dahiya et al. (2010)*).

Over the years, a wide range of tactile sensing solutions has been proposed, which vary according their transduction principles, materials, fabrication techniques, and sensor architectures. Each approach offers specific advantages and limitations in terms of sensitivity, dynamic range, response time, robustness, scalability, and ease of integration on robotic structures (*Meribout et al. (2024); Mishra et al. (2021)*). As a result, there exists no tactile sensing technology that can be considered universally optimal, and the choice of the sensing principle is strongly application-dependent.

The most widely investigated transduction mechanisms are piezoresistive, piezoelectric, optical, magnetic, iontronic, and capacitive sensing. Piezoresistive tactile sensors exploit changes in electrical resistance induced by mechanical deformation and are often chosen for their simple readout circuitry and straightforward fabrication (*Shu et al. (2024)*). However, they may suffer from hysteresis, drift, and limited long-term stability, especially under repeated loading cycles (*Kurnaz et al. (2023)*). Piezoelectric sensors, on the other hand, provide high sensitivity and fast response but are intrinsically unsuitable for static force measurements, as they primarily respond to dynamic stimuli (*Meribout et al. (2024)*).

Optical and magnetic tactile sensors have also been explored, offering high spatial resolution and, in some configurations, decoupled multi-axis force sensing (*Lee et al. (2008)*). Recent developments in optical tactile sensing include LIDAR-based approaches embedded within flexible wave guides, capable of detecting both touch and pressure with high accuracy (*Bacher et al. (2024)*). Nevertheless, these solutions typically require complex assemblies, bulky components, or external sensing elements, which limit their applicability for large-area and conformable robotic skins. More recently, iontronic tactile sensors have demonstrated extremely high sensitivities by exploiting electric double-layer capacitance at ionic interfaces (*Bai et al. (2023); Shi et al. (2023)*). Despite their promising performance, concerns related to long-term reliability, environmental stability, and integration complexity remain open research challenges.

Capacitive tactile sensors represent one of the most established and widely adopted tech-

nologies in robotic applications. Their operating principle relies on variations in capacitance induced by mechanical deformation of a dielectric layer placed between conductive electrodes. Capacitive sensors are particularly attractive due to their high sensitivity, low power consumption, good repeatability, and compatibility with a wide range of flexible substrates and fabrication techniques (*Li et al. (2021); Ma et al. (2023)*). Moreover, capacitive transduction enables both static and dynamic force measurements, making it well suited for robotic tasks.

In literature a branch of research has focused on improving the performance of capacitive tactile sensors through material engineering, micro-structured dielectric layers, and novel sensor geometries. Techniques such as porous or patterned elastomers, hierarchical microstructures, and bio-inspired designs have been proposed to enhance sensitivity while preserving a wide operational pressure range (*Choi et al. (2020); Xu et al. (2023); Zhang et al. (2022)*). At the same time, fabrication approaches based on screen printing, inkjet-printing, spin coating, and additive manufacturing have been extensively investigated to reduce costs and enable scalable production of tactile sensing systems (*Aubeeluck et al. (2024); Eshkeiti et al. (2014); Salim and Lim (2017)*).

Despite these advances, several challenges remain open, particularly when capacitive tactile sensors are deployed as large-area robotic skins. Scaling from single taxels to dense sensor arrays introduces issues related to crosstalk, wiring complexity, signal routing, and data acquisition bandwidth (*Chen et al. (2020); Lee et al. (2006)*). Furthermore, achieving high sensitivity without excessively increasing sensor thickness or compromising mechanical robustness is still a critical trade-off. These limitations have motivated the exploration of alternative architectures, such as vertically stacked capacitive sensors and distributed sensing networks, aimed at enhancing spatial resolution, dynamic range, and system-level scalability (*Chandra et al. (2017); Staiano et al. (2023)*).

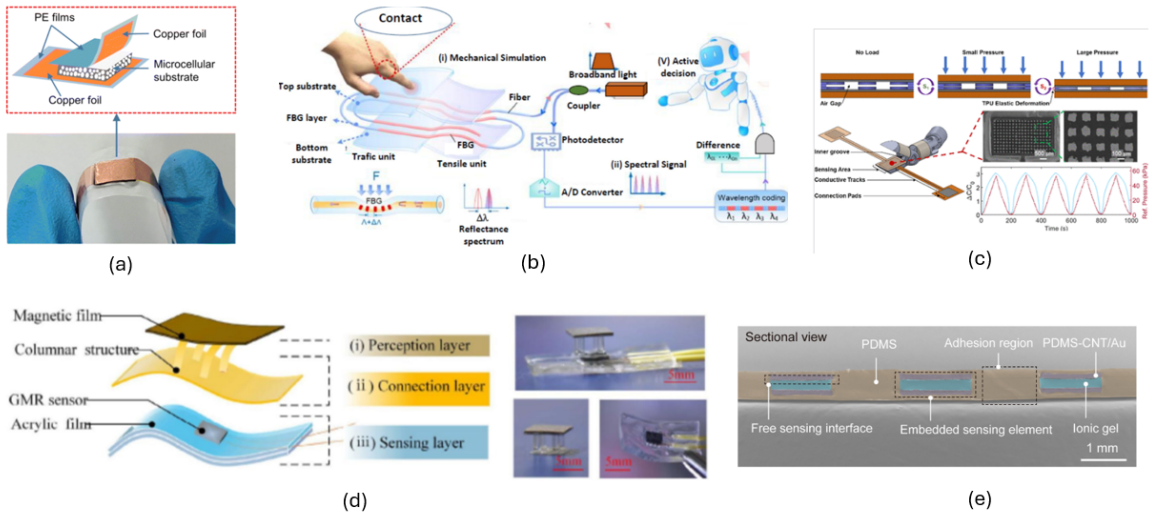

Figure 1.3 Tactile sensing technologies: **(a)** Schematic of flexible piezoresistive sensor with closed-cell structures structure *(Shu et al. (2024))*. **(b)** fiber Bragg gratings (FBGs) base tactile sensor *(Meribout et al. (2024))*. **(c)** schematic of a capacitive tactile sensor *(Aubeeluck et al. (2024))*. **(d)** Magnetic tactile sensor *(Meribout et al. (2024))*. **(e)** SEM image of the cross-sectional view of the iontronic sensor array *(Shi et al. (2023))*.

1.2.1 Performance Metrics and Comparative Analysis

To evaluate tactile sensing technologies for robotic applications it is important to perform characterizations on both sensor-level characteristics and system-level constraints.
One of the most relevant parameters is **sensitivity**, typically defined as the variation of the electrical output with respect to the applied pressure or force:

$$S = \frac{\Delta O}{\Delta P} \tag{1.1}$$

where:
O is the sensor output (capacitance, resistance, voltage charge)
P is the applied pressure

In the case of capacitive sensors:

$$S_C = \frac{\Delta C}{\Delta P} \tag{1.2}$$

High sensitivity is particularly desirable in low-pressure regimes, where gentle contacts and early collision detection are required. However, sensors characterized by high sensitivity often exhibit a limited operational range, reaching saturation at relatively low or moderate

pressure levels. This trade-off between sensitivity and measurable pressure range is widely reported in the literature and represents a common limitation across many tactile sensing technologies.

Dynamic range represents another critical performance metric, particularly for robotic manipulation tasks that require the perception of both low-intensity contacts and higher interaction forces.Sensors designed to operate over a wide pressure range often exhibit reduced resolution in the low-pressure regime, whereas sensors optimized for fine touch perception may show limited performance when subjected to higher loads. Achieving a consistent and reliable response across different pressure regimes remains an open challenge, especially in the context of large-area tactile sensing systems.
The metric is often defined as the interval of measurable pressure values over which the sensor provides a reliable and non-satured output:

$$DR = P_{\max} - P_{\min} \tag{1.3}$$

But in some scenarios tactile data are acquired and processed in the digital domain, dynamic range can be expressed in terms of the number of effective usable bits of the sensor output.

$$DR_{\text{bits}} = \frac{20\log_{10}(C_{\max} - C_{\min})}{8} \tag{1.4}$$

In this formulation, the dynamic range corresponds to the interval of measurable raw counts and provides an estimate of the effective bit resolution of the sensing system.

Temporal characteristics, such as **response time** and **relaxation time**, are equally important. Fast response enables timely detection of contacts and rapid feedback for control loops, while short relaxation times reduce signal lag and hysteresis effects during repetitive interactions. Hereafter the equations:

$$\Delta T_{\text{RES}} = t_{\text{RESmax}} - t_{\text{RESmin}} \tag{1.5}$$

$$\Delta T_{\text{REL}} = t_{\text{RELmax}} - t_{\text{RELmin}} \tag{1.6}$$

where:
t_{RESmax} and t_{RESmin} are respectively the point in time of the rising response on an applied pressure and the point before.
t_{RELmax} and t_{RELmin} are respectively the point in time after the falling response on an applied

pressure and the point of the falling response.

Hysteresis and **repeatability** have a significant impact on the long-term reliability of tactile sensors, particularly under repeated loading and unloading conditions. Materials with viscoelastic behavior, commonly employed to enhance sensitivity, often introduce nonlinearities and memory effects that degrade measurement consistency. Repeatability under cyclic loading is therefore a key indicator of sensor robustness, especially for applications involving continuous physical human–robot interaction.
Hereafter the equations of hysteresis and repeatability:

$$H(P) = \frac{|O_{\text{load}}(P) - O_{\text{unload}}(P)|}{O_{\max}} \times 100 \tag{1.7}$$

$$R_{\%} = \sigma_O \times 100 \tag{1.8}$$

where:
σ_O is the standard deviation of the response.

When scaling from single sensing elements to dense arrays or large-area skins, additional system-level metrics must be considered. Crosstalk between adjacent taxels can degrade spatial resolution, while wiring complexity and signal routing increasingly limit the integration of dense tactile sensor arrays. Moreover, the large volume of data generated by high-resolution tactile arrays introduces constraints on data acquisition bandwidth and communication infrastructures, thereby impacting the overall system architecture rather than the sensing element alone *(Dahiya et al. (2010); Ma et al. (2023); Mishra et al. (2021))*.

Besides that, a qualitative comparison among the tactile sensing technologies is presented in Table 1.1 to highlight how each transduction principle addresses specific application requirements while introducing characteristic limitations. As a result, the suitability of a tactile sensing solution strongly depends on the intended robotic task, the required performance metrics, and the integration constraints *(Cannata et al. (2008); Chandra et al. (2017); Maiolino et al. (2013); Staiano et al. (2023))*.

Although a wide range of tactile sensing technologies has been investigated in the literature, none of the existing solutions fully satisfies the combined requirements of robotic skin applications. In particular, achieving high sensitivity in low-pressure regimes while

Technology	Sensitivity	Dynamic Range	Static Force	Scalability	Limitations
Piezoresistive	Medium	Medium	Yes	High	Hysteresis, drift, repeatability
Piezoelectric	High (dynamic)	Low	No	Medium	No static response
Optical / Magnetic	High	Medium	Yes	Low	Complexity, bulkiness
Iontronic	Very high	Low–Medium	Yes	Medium	Stability, integration
Capacitive	Medium–High	Medium–High	Yes	High	Crosstalk, wiring complexity

Table 1.1 High-level comparison of tactile sensing technologies for robotic applications.

maintaining a wide dynamic range, mechanical robustness, and scalability over large and complex surfaces remains a challenging task.

Capacitive tactile sensors represent a well-established solution for robotic applications, as they enable both static and dynamic force measurements and can be implemented on flexible substrates using scalable fabrication processes. However, typical capacitive sensor designs are often affected by trade-offs involving sensitivity, sensor thickness, spatial resolution, and system-level integration, especially when implemented as dense arrays or large-area skins. These limitations motivate the exploration of alternative sensor architectures and design strategies aimed at improving tactile performance while preserving integration feasibility. In this context, multilayer and vertically stacked capacitive sensing approaches offer a promising direction to address the limitations of single-layer designs and to support the development of scalable tactile sensing systems for robotic applications.

1.3 The SESTOSENSO Project

The development of advanced tactile sensing technologies addressed in this dissertation is framed within the context of **SESTOSENSO** (GA 101070310), a Horizon Europe research project which has the aim of guarantee safe, efficient, and flexible human–robot collaboration in industrial environments. The project focuses on the design and integration of distributed multi-modal sensing systems capable of providing robots with enhanced perception of their surroundings, with particular emphasis on physical interaction and proximity awareness.
Modern industrial scenarios require robots to operate outside traditional fenced work cells and to share the workspace with human operators. In such contexts, safety cannot rely solely on pre-programmed trajectories or external sensing infrastructures, such as vision systems or motion capture setups, which may limit flexibility and increase deployment costs. Instead, sensing capabilities must be embedded directly on the robot body, allowing continuous monitoring of contacts, distances, and interaction forces in a distributed and redundant manner.
Within this framework, SESTOSENSO investigates sensing architectures that combine tactile and proximity information to support human-centered robotic applications. The project addresses key challenges related to large-area sensorization, mechanical adaptability to complex robot geometries, data acquisition scalability, and real-time communication. By embedding sensing capabilities into flexible skin-like systems, robots can achieve a form of spatial awareness that extends beyond the end-effector, enabling earlier contact detection, safer interactions, and more adaptive control strategies.
A central technological outcome of the SESTOSENSO project is the development of ProxySKIN, a multi-modal distributed sensing architecture that integrates tactile sensing with time-of-flight (ToF) proximity sensors *(Giovinazzo et al. (2024a))*. ProxySKIN is conceived as a modular and scalable robotic skin capable of covering large portions of a robot manipulator, providing both contact-based and pre-contact information. The tactile component of ProxySKIN is based on CySkin technology *(Maiolino et al. (2013))*, while proximity sensing is achieved through arrays of compact ToF sensors embedded within the same flexible substrate.
From a system-level perspective, ProxySKIN serves as a testbed for validating sensing technologies, data acquisition architectures, and communication protocols under realistic robotic conditions. The integration of hundreds to thousands of sensing elements generates a significant data flow, requiring reliable and deterministic communication infrastructures. For this reason, the project explores distributed acquisition architectures based on industrial real-time communication protocols, enabling synchronized data transfer and scalable network

topologies.

The technologies developed within SESTOSENSO are evaluated through multiple demonstrators addressing representative industrial use cases, including collaborative manipulation, human–robot interaction, and robot-assisted operations in unstructured environments. These demonstrators provide a concrete validation of the proposed sensing solutions and highlight the practical constraints associated with large-area tactile sensing, such as sensor integration, wiring, robustness, and system-level reliability.

In this context, the research presented in this dissertation contributes to SESTOSENSO by addressing key technological aspects of robotic tactile sensing, ranging from sensor design and fabrication to system integration and large-scale deployment. The proposed solutions, including multilayer capacitive tactile sensors, CySkin+, and PeSkin, are developed and validated within the SESTOSENSO framework, ensuring their relevance to real-world robotic applications.

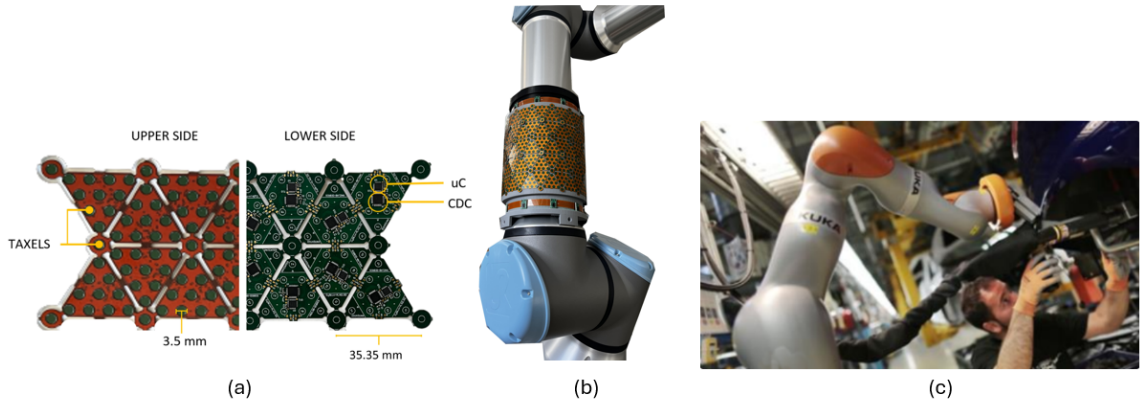

Figure 1.4 (a) Upper side and lower side of CySkin technology *(Maiolino et al. (2013))*. **(b)** Integration of ProxySKIN technology on UR10 robot *(Giovinazzo et al. (2024))*. **(c)** SESTOSENSO context *(sestosenso.eu)*.

1.4 Objectives and Outline

The research activity presented in this dissertation is motivated by the need for tactile sensing solutions that can be effectively integrated on robotic platforms operating in close proximity to humans. While tactile sensing has been widely investigated in the literature, several technological and system-level challenges remain open, particularly with respect to large-area coverage, fabrication scalability, data acquisition, and integration on complex robot geometries.

The main objective of this thesis is the design, fabrication, and experimental characterization of capacitive tactile sensing technologies that address these challenges and support the development of scalable robotic skin systems. The work focuses on solutions that reduce integration complexity while preserving sensing performance, robustness, and adaptability to different robotic applications.

More specifically, the scientific and technological objectives of this project are summarized as follows:

- Investigate capacitive tactile sensing architectures with enhanced sensitivity and dynamic range, suitable for both low-pressure interactions and higher contact forces;
- Develop multilayer and vertically stacked capacitive sensor designs aimed at improving sensing performance without increasing sensor footprint or thickness;
- Explore low-cost and scalable fabrication techniques, such as inkjet printing, screen printing, and additive manufacturing, for the realization of small- and large-area tactile sensor patches;
- Design tactile sensing solutions that can conform to curved and complex robot surfaces, supporting modular and distributed integration;
- Analyze the system-level implications of large-area tactile sensing, including data acquisition, communication bandwidth, and scalability;
- Validate the proposed technologies through experimental characterization.

Based on these objectives, this dissertation presents three main tactile sensing solutions, each addressing specific aspects of the problem. **Multilayer capacitive tactile sensors** are introduced as a means to improve sensitivity and dynamic range through architectural design. **CySkin+** is presented as an evolution of an existing large-area capacitive skin technology, with a focus on material selection, robustness, and system integration. **PeSkin** is introduced

as a large-area tactile sensing solution based on printed electronics, designed to simplify fabrication and deployment over extended robot surfaces.
The remainder of this dissertation is organized as follows:

- **Chapter 2** introduces multilayer capacitive tactile sensors, describing the underlying working principles, sensor design, fabrication process, and experimental characterization.
- **Chapter 3** focuses on CySkin+, detailing its design evolution, material and substrate choices, system integration, and communication architecture within a distributed sensing framework.
- **Chapter 4** presents PeSkin, a large-area tactile sensing technology based on printed electronics, including fabrication techniques, sensor layout, embedded architecture, and experimental validation.
- **Chapter 5** summarizes the main contributions of this work and discusses future research directions related to scalable tactile sensing for robotic applications.

Chapter 2

Multilayer Capacitive Tactile Sensors

2.1 Working Principle of Capacitive Tactile Sensors

Capacitive tactile sensors rely upon the variation of capacitance made by mechanical deformation under applied load. The simplest and most commonly adopted configuration consists of two conductive electrodes separated by a deformable dielectric layer. When an external pressure is applied, the dielectric compresses, resulting in a change in the distance between the electrodes and, consequently, in the measured capacitance.
For a parallel-plate capacitor, the capacitance C is expressed as:

$$C = \varepsilon_0 \varepsilon_r \frac{A}{d} \tag{2.1}$$

where:

- ε_0 is the vacuum permittivity,
- ε_r is the relative permittivity of the dielectric material,
- A is the overlapping area of the electrodes,
- d is the separation distance between the electrodes.

In tactile sensing applications, the applied pressure P produces a deformation of the dielectric layer, reducing the effective thickness d. Assuming small deformations and linear elastic behavior, the capacitance variation ΔC can be related to the applied pressure through the mechanical properties of the dielectric material. As a result, capacitive sensors provide a direct transduction from mechanical stimuli to an electrical quantity, which can be measured using capacitance-to-digital converters (CDCs) or dedicated analog front-end circuits.

One of the main advantages of capacitive tactile sensors lies in their ability to measure both static and dynamic loads with good repeatability and low power consumption. Moreover, their operating principle is compatible with a wide range of flexible substrates and fabrication techniques, making them suitable for conformable and large-area sensing applications *(Cannata et al. (2008); Maiolino et al. (2013))*.

Despite these advantages, single-layer capacitive tactile sensors exhibit inherent limitations when deployed in robotic skin applications. In particular, sensitivity is strongly influenced by the initial thickness and mechanical stiffness of the dielectric layer. Thin and compliant dielectrics improve sensitivity in the low-pressure regime but tend to saturate rapidly, limiting the operational pressure range. On the other hand, thicker or stiffer dielectrics extend the dynamic range at the cost of reduced sensitivity. This trade-off represents a fundamental constraint of conventional single-layer capacitive sensor designs *(Ma et al. (2023); Mishra et al. (2021))*.

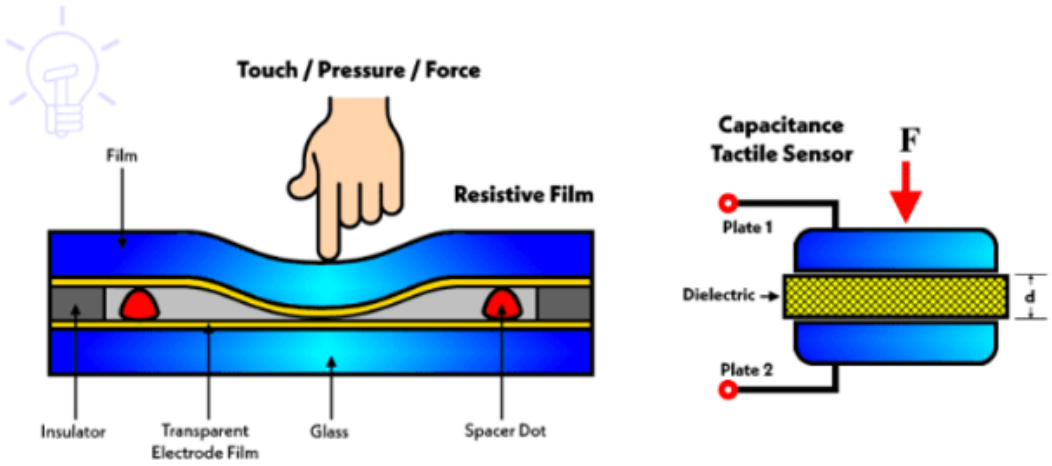

Figure 2.1 Working principle of Capacitive Tactile Sensors

2.2 Multilayer and Vertically Stacked Architectures

The limitations observed in single-layer capacitive tactile sensors motivate the investigation of alternative architectural solutions aimed at improving sensing performance while maintaining compatibility with robotic skin applications. In robotic scenarios, tactile sensors are required to operate across different pressure regimes, ranging from low-intensity contacts to higher interaction forces, while maintaining consistent sensing behavior.

In single-layer designs, sensitivity is mainly determined by the thickness and mechanical properties of the dielectric layer. Reducing the dielectric thickness or using compliant materials improves sensitivity in the low-pressure regime, but often results in early saturation and reduced stability when higher loads are applied. Although, designs intended to operate over a wider pressure range typically exhibit lower resolution for small deformations. This trade-off between sensitivity and dynamic range represents a well-known limitation of single-layer capacitive tactile sensors.

A further constraint in robotic skin applications concerns the lateral size of the sensing element. Increasing sensitivity by enlarging the electrode area is often not practical, as tactile sensors are expected to be densely distributed over curved and articulated robot surfaces. For this reason, improvements in sensing performance must be achieved without increasing the in-plane dimensions of the sensor.

Multilayer and vertically stacked capacitive architectures address these limitations by exploiting the thickness direction of the sensor rather than its surface area. By arranging multiple capacitive elements along the vertical axis, the applied mechanical load is shared among several dielectric layers, each contributing to the overall electrical response. This approach allows an increase in the capacitance variation under applied pressure while keeping the lateral footprint unchanged.

From a modeling perspective, a vertically stacked capacitive sensor can be represented as a set of capacitive layers subjected to the same external load. The combined response of the stacked elements leads to improved sensitivity compared to a single-layer configuration, without requiring larger sensing areas or complex surface geometries. This characteristic makes vertically stacked architectures suitable for robotic skin applications, where high spatial resolution and dense sensor integration are required.

Previous studies have explored stacked capacitive configurations to improve sensor performance at the element level *(Chandra et al. (2017), Jen et al. (2021))*, and also for other applications purposes like in *Momota et al. (2023)* to create supercapacitors. However, a detailed analysis that combines analytical modeling, numerical simulations, fabrication

methods, and experimental characterization is required to assess the potential of these architectures in scalable tactile sensing systems. The following sections address this aspect through a systematic investigation of multilayer capacitive tactile sensors.

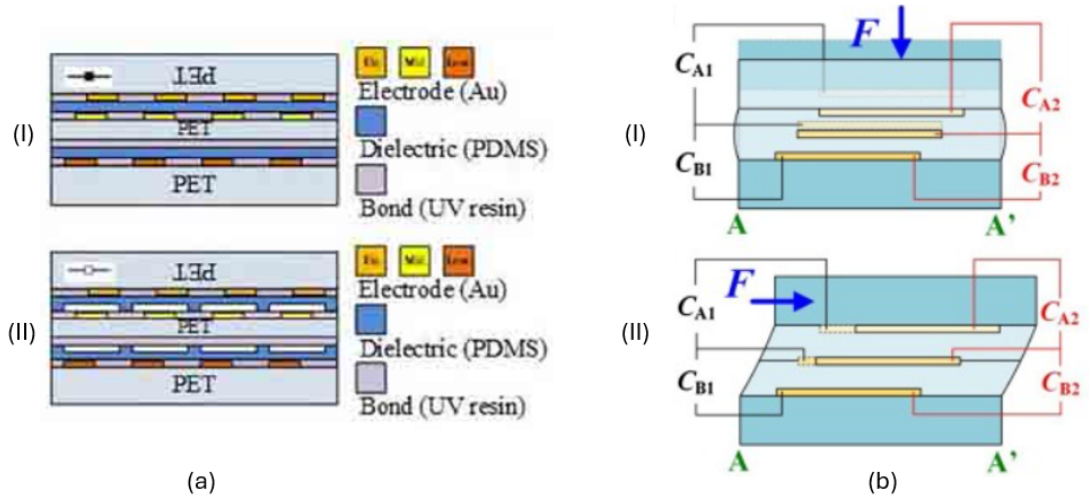

Figure 2.2 (a) Cross-sectional view of 3-layers vertically stacked capacitive sensors introduced in *Jen et al. (2021)*: **(I)** structure with solid dielectrics, **(II)** structure with hollow dielectrics. **(b)** Cross-sectional view of 3-layers vertically stacked capacitive sensor proposed in *Chandra et al. (2017)*: **(I)** sensor under normal force, **(II)** sensor under shear force.

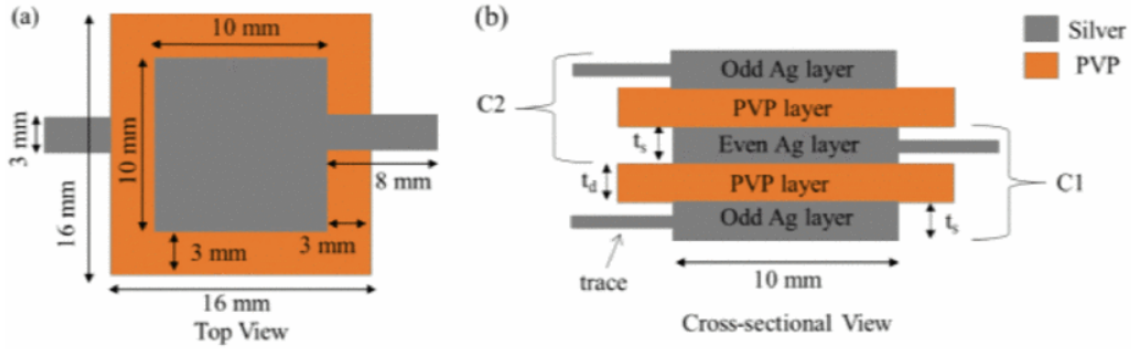

Figure 2.3 Design of the vertically stacked supercapacitor proposed in *Momota et al. (2023)*. **(a)** Top view, and **(b)** cross-sectional view

2.3 Mathematical Model of Vertically Stacked Capacitive Tactile Sensors

While single-layer capacitive sensors are well described by the standard parallel-plate model, extending this formulation to vertically stacked configurations is not straightforward. In a multilayer structure, the applied load is distributed across multiple deformable layers whose mechanical coupling determines the overall electrical response. Understanding how sensitivity scales with the number of stacked layers requires an analytical framework that captures this interaction. Without such a model, the design of multilayer sensors would rely entirely on empirical fabrication and testing, making it difficult to predict performance trends or to guide the selection of materials and geometric parameters. Establishing an analytical relationship between stacking configuration and sensitivity is therefore a necessary step to support systematic sensor design and to provide a reference for numerical and experimental validation.

The behavior of vertically stacked capacitive tactile sensors can be described by extending the classical model of a single parallel-plate capacitive element to a multilayer configuration. The objective of this model is to quantify the relationship between the applied mechanical load and the resulting electrical response, and to highlight the advantages of vertical stacking in terms of sensitivity and dynamic range.

2.3.1 Single-layer Capacitive Sensor Model

For a single capacitive tactile sensor, the capacitance at rest C_0 is given by the parallel-plate expression:

$$C_0 = \varepsilon_0 \varepsilon_r \frac{A}{d_0} \tag{2.2}$$

When a normal pressure P is applied to the sensor, as shown in Fig 2.4 the dielectric layer undergoes a compression Δd:

$$d = d_0 - \Delta d \tag{2.3}$$

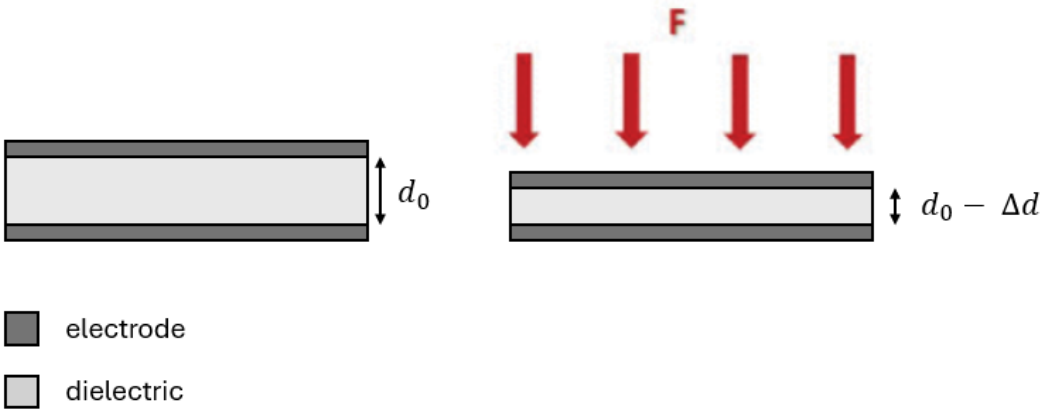

Figure 2.4 Cross-sectional view of the sensor compression under applied pressure

Assuming a linear elastic behavior of the dielectric material and uniform pressure distribution, we can compare the deformation of the dielectric material with the deformation of the equivalent spring.
Knowing that pressure equation is:

$$F = P \cdot A \tag{2.4}$$

And spring equation is:

$$F = -k \cdot \Delta d, \quad \Delta d > 0 \tag{2.5}$$

Where k is the elastic constant of the equivalent spring that can be expressed using the standard stiffness engineering model as in *LaCroix et al. (2013)*:

$$k = \frac{E \cdot A}{d_0} \tag{2.6}$$

Where E is the Young's Modulus of the material.
Then we compare equations 2.5 and 2.4:

$$-\frac{E \cdot A}{d_0} \cdot \Delta d = A \cdot P \tag{2.7}$$

Thus, we can write the deformation as:

$$\Delta d = -\frac{P \cdot d_o}{E} \tag{2.8}$$

Now, considering the capacitance when pressure is applied as:

$$C = \varepsilon_0 \varepsilon_r \frac{A}{d_0 - \Delta d} \tag{2.9}$$

But since for small deformations ($\Delta d << d_0$) a first-order Taylor expansion can be applied, we can rewrite the equation as:

$$C \approx \varepsilon_0 \varepsilon_r \frac{A}{d_0} \left(1 + \frac{\Delta d}{d_0}\right) \tag{2.10}$$

At this point we compute the capacitance variation:

$$\Delta C = C - C_0 \approx \varepsilon_0 \varepsilon_r \frac{A}{d_0^2} \Delta d \tag{2.11}$$

Finally we use equation 2.8 into 2.11:

$$\Delta C \approx -\varepsilon_0 \varepsilon_r \frac{A}{d_0} \frac{P}{E} \tag{2.12}$$

The negative sign in the obtained expression reflects the reduction of the dielectric thickness under applied pressure.
In the following analysis, we focus on the magnitude of the capacitance variation, which represents the relevant quantity for sensitivity evaluation and comparison.

$$|\Delta C| \approx \varepsilon_0 \varepsilon_r \frac{A}{d_0} \frac{P}{E} \tag{2.13}$$

2.3.2 Vertically Stacked Capacitive Sensor Model

A vertically stacked capacitive tactile sensor consists of multiple single capacitive elements arranged along the thickness direction, as illustrated in Fig 2.5 Each layer is composed of two electrodes separated by a dielectric layer of thickness d_0, identical to the single-layer configuration described in the previous subsection.

Assuming a stack composed of N identical layers and uniform pressure distribution over the sensor surface, the applied pressure P generates a total force:

$$F = P \cdot A \tag{2.14}$$

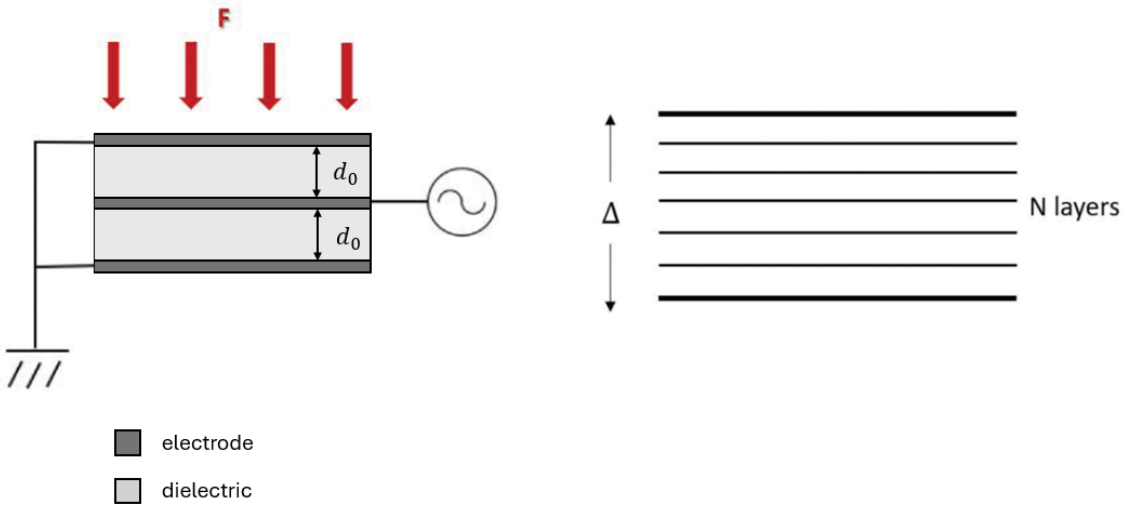

Figure 2.5 Cross-sectional view of the two-layer vertically stacked capacitive sensor and the generalization for N-layers

From a mechanical standpoint, the stacked structure can be modeled as a set of N linear springs connected in series, each representing the elastic behavior of a single dielectric layer. The stiffness of each equivalent spring is:

$$k = \frac{E \cdot A}{d_0} \tag{2.15}$$

For springs connected in series, the equivalent stiffness of the stack is given by:

$$k_{\text{eq}} = \frac{k}{N} \tag{2.16}$$

The total deformation of the stacked sensor under the applied force can therefore be expressed as:

$$\Delta d_{\text{tot}} = \frac{F}{k_{\text{eq}}} = \frac{P \cdot A}{k_{\text{eq}}} \tag{2.17}$$

Substituting the expression of k_{eq} the total deformation becomes:

$$\Delta d_{\text{tot}} = N \cdot \frac{P \cdot d_0}{E} \tag{2.18}$$

Since the deformation is uniformly distributed across the N layers, the compression of each individual dielectric layer is:

$$\Delta d_i = \frac{\Delta d_{\text{tot}}}{N} = \frac{P \cdot d_0}{E} \tag{2.19}$$

As a result, each capacitive element in the stack experiences the same deformation as the single-layer sensor, while the overall electrical response is obtained by combining the contribution of all layers.

The capacitance variation of the i-th layer can be written, consistently with the single-layer model, as:

$$|\Delta C_i| \approx \varepsilon_0 \varepsilon_r \frac{A}{d_0} \frac{P}{E} \tag{2.20}$$

Assuming that the capacitances of the stacked layers are read independently and combined at the electrical level, the total capacitance variation of the vertically stacked sensor is given by:

$$|\Delta C_{\text{tot}}| = \sum_{i=1}^{N} |\Delta C_i| \tag{2.21}$$

Which yields:

$$|\Delta C_{\text{tot}}| \approx N \, \varepsilon_0 \varepsilon_r \frac{A}{d_0} \frac{P}{E} \tag{2.22}$$

This result shows that the capacitance variation — and consequently the sensitivity — increases linearly with the number of stacked layers. Importantly, this improvement is achieved without increasing the electrode area or modifying the in-plane geometry of the sensing element, as the enhancement is obtained by exploiting the thickness direction of the sensor.

The analytical formulation presented in this sections follows the model introduced in *Staiano et al. (2023)* and provides a clear theoretical basis for the design of multilayer capacitive tactile sensors. The assumptions adopted in this derivation are further examined and validated through numerical simulations in the following section.

2.4 Finite Element Simulations

The analytical model developed in Section 2.3 was validated through numerical simulations performed using the finite element method (FEM) within the computational physics suite *COMSOL Multiphysics*. The numerical analysis was used to assess the mechanical behavior of vertically stacked capacitive tactile sensors under applied pressure and to verify the assumptions adopted in the analytical derivation.

Two distinct FEM simulation analyses were carried out within this work. The first set of simulations follows the approach presented in *Staiano et al. (2023)* and is based on the material properties and geometric parameters corresponding to the inkjet-printed multilayer sensors. These simulations are used to validate the analytical model under controlled conditions and to investigate the effects of vertical stacking under equal total thickness constraints.

A second set of FEM simulations was performed using material properties representative of screen-printed multilayer sensors. While the underlying sensor architecture remains unchanged, the mechanical parameters of the dielectric layers differ due to the fabrication process and materials employed. This second numerical analysis allows the evaluation of the robustness of the proposed model when applied to different manufacturing technologies and provides a consistent reference for the experimental characterization of screen-printed sensors presented in the following sections.

In both cases, the FEM simulations focus on the comparison between single-layer and vertically stacked configurations, with particular attention to the pressure–deformation relationship and the resulting sensitivity trends. The numerical results discussed in this section provide the basis for the experimental validation reported in Sections 2.5 and 2.6 for inkjet-printed sensors, and later extended to screen-printed multilayer sensors.

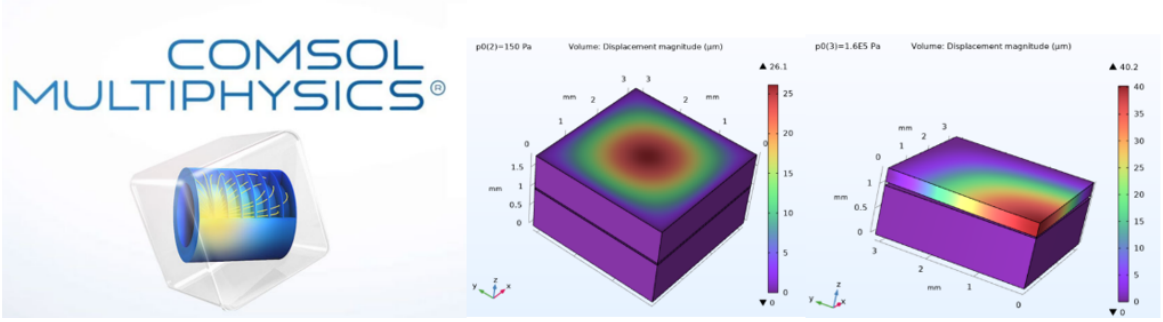

Figure 2.6 Example of COMSOL Multiphysics for mechanical displacement in electromechanics study

2.4.1 FEM Analysis with Inkjet-Printed Sensor Parameters

Finite element simulations were performed in COMSOL Multiphysics to validate the analytical model derived in Section 2.3 using the material properties and geometric parameters corresponding to the inkjet-printed multilayer sensors presented in *Staiano et al. (2023)*. The numerical analysis focuses on the mechanical deformation of the dielectric layers under applied pressure and on the comparison between single-layer and vertically stacked configurations. For this purpose *PDMS* was considered as dielectric and *Silver (Ag)* for the electrodes. PDMS was chosen for its mechanical properties reported in Table 2.1.

Property	**Value**
Young's modulus (E)	200 kPa
Poisson's ratio, (ν)	0.49
Relative permittivity (ε_r)	2.75

Table 2.1 PDMS material properties.

The FEM model reproduces the cross-sectional geometry of the capacitive tactile sensor, including the dielectric layer and the electrode interfaces. The simulated transducer has diameter $\phi = 4$ *mm* and dielectric thickness $d = 100$ μm. The dielectric material is modeled as a linear elastic solid, while the electrodes are assumed rigid. A uniform pressure is applied normal to the top surface of the sensor, and the bottom electrode is mechanically constrained. For the simulations, two classes of contacts have been selected, following *Choi et al. (2020)* and *Kurnaz et al. (2023)*. The first class is referred to as *gentle touch* and is characterized by contact pressures in the *0–10 kPa* range, whereas the second class, *manipulation-like touch*, refers to pressures in the *10–100 kPa* range. The material properties used in the simulations are consistent with those reported in the experimental characterization of the inkjet-printed sensors. Figure 2.7 shows the dielectric geometrical model and Figure 2.8 shows the response of the sensors after the range of pressures applied.

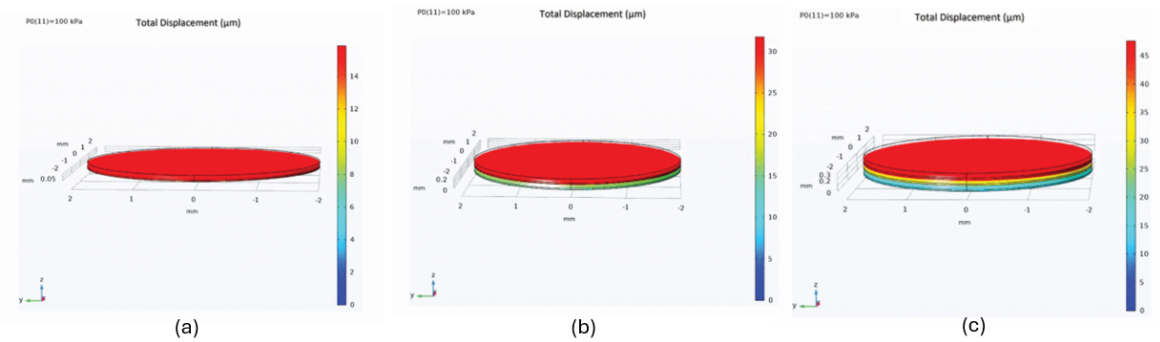

Figure 2.7 Simulated dielectric displacement in COMSOL: **(a)** 1 dielectric layer. **(b)** 2 dielectric layers. **(c)** 3 dielectric layers.

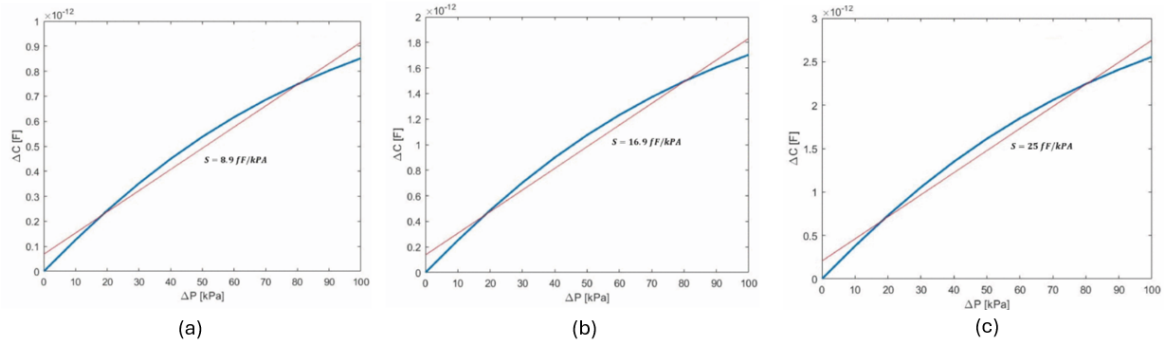

Figure 2.8 Pressure/capacitance characterization obtained from finite element simulation with the corresponding sensitivity: **(a)** 1 dielectric layer. **(b)** 2 dielectric layers. **(c)** 3 dielectric layers.

The FEM results show that, under the same applied pressure, the vertically stacked configuration exhibits a larger overall deformation compared to the single-layer sensor. At the same time, the deformation experienced by each individual dielectric layer in the stacked configuration remains comparable to that of the single-layer sensor. This behavior confirms the spring-in-series representation adopted in the analytical model and demonstrates that the increased deformation originates from the architectural arrangement of the layers rather than from changes in material properties or total thickness.

The pressure–deformation curves obtained from the simulations exhibit a linear trend within the investigated pressure range for both configurations, in agreement with the assumptions of linear elastic behavior used in the analytical derivation. The FEM results therefore confirm that vertical stacking increases the mechanical response of the sensor while maintaining controlled deformation levels within each dielectric layer.

Based on the simulated deformation fields, the capacitance variation was estimated using the analytical relationship derived in Section 2.3 The resulting sensitivity trends show that vertically stacked sensors provide a higher sensitivity compared to single-layer configurations under equal thickness conditions, in agreement with the analytical prediction. These numerical results provide a first validation of the proposed model using parameters representative of inkjet-printed multilayer sensors.
Figure 2.9 compares the sensitivities obtained from the model. Sensitivity increases by 90% passing from a single capacitor ($S = 8.9 fF/kPa$) to two-stack ($S = 16.9 fF/kPa$), and it increases by 48% passing from a two-stack to a three-stack ($S = 25 fF/kPa$). The sensitivity increases by 180% if we pass from a single capacitor to a three-stack capacitor. Also, in this case, the sensitivity will increase every time we add a capacity in parallel to the stack.

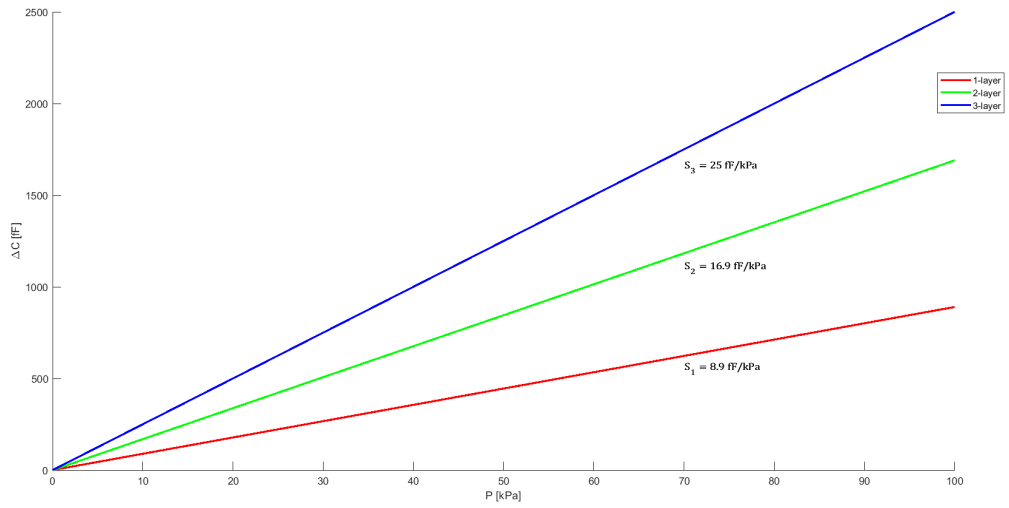

Figure 2.9 Finite element response with the corresponding sensitivity in the case of one-layer sensor, two-layers sensor, and three-layers sensor, assuming a linear model for the dielectric material.

The FEM analysis presented in this subsection provides the numerical reference for the experimental characterization of inkjet-printed multilayers sensors discussed in the following sections

2.4.2 FEM Analysis with Screen-Printed Sensor Parameters

A second set of finite element simulations was performed in COMSOL to study the stacked architecture under material parameters representative of the screen-printed sensors. In this

case, the dielectric was modeled as air and the mechanical deformation was attributed to the electrodes. The air gap thickness was set to $d = 165\ \mu m$, while the remaining sensor geometry was kept consistent with the configurations used in Section 2.4.1.
The electrode material was modeled using the mechanical properties of PET and using the relative permittivity (ε_r) of air as shown in Table 2.2. Fig 2.10 shows the geometry model under simulated pressure from 1 up to 5 dielectric layers.

Property	**Value**
Young's modulus (E)	4 GPa
Poisson's ratio, (ν)	0.33
Relative permittivity (ε_r)	1

Table 2.2 PET material properties.

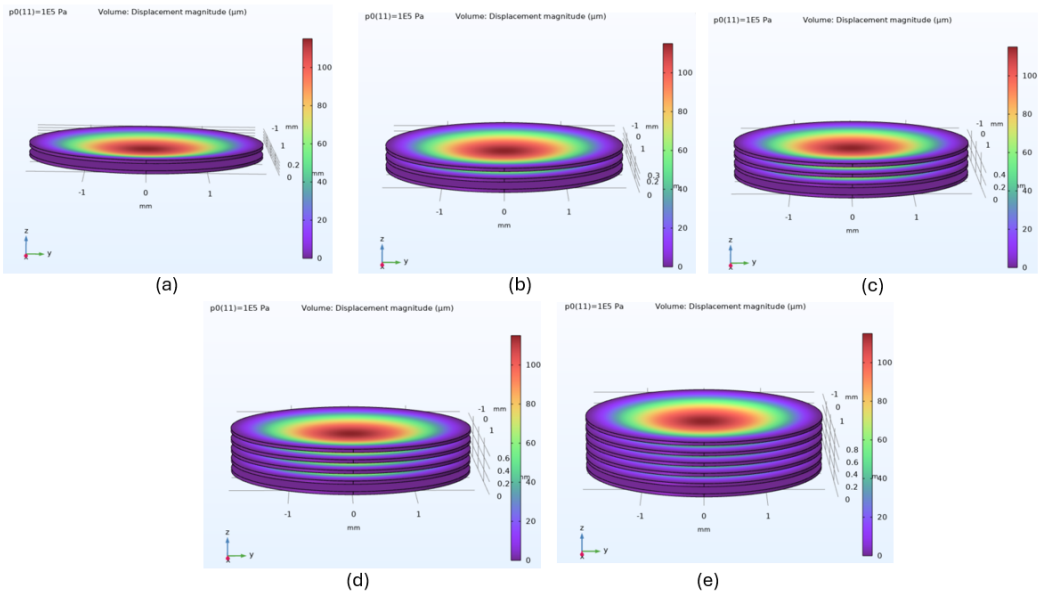

Figure 2.10 Simulated dielectric displacement in COMSOL: **(a)** 1 dielectric layer. **(b)** 2 dielectric layers. **(c)** 3 dielectric layers. **(d)** 4 dielectric layers. **(e)** 5 dielectric layers.

Under these conditions, the structure exhibits a reduced mechanical compliance compared to the inkjet-based simulations. As a consequence, the capacitance response obtained from FEM is lower in absolute terms. Figure 2.11 show the resulted responses.

Despite this difference, the numerical results confirm the same qualitative trend predicted by the analytical model: vertically stacked configurations provide a higher sensitivity than the

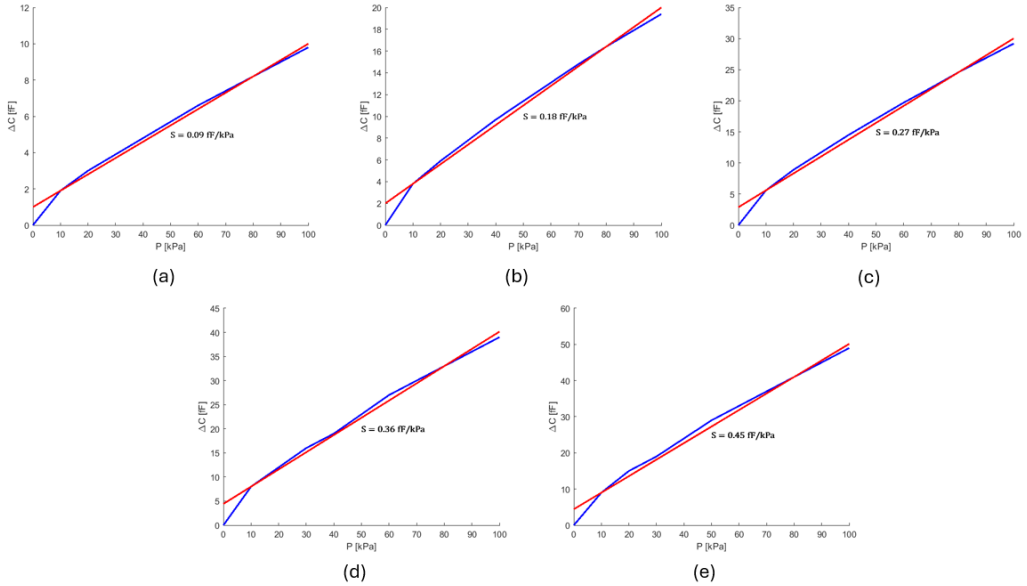

Figure 2.11 Pressure/capacitance characterization obtained from finite element simulation with the corresponding sensitivity: **(a)** 1-layer sensor, **(b)** 2-layers sensor, **(c)** 3-layers sensor, **(d)** 4-layers sensor, and **(e)** 5-layers sensor assuming a linear model for the dielectric material.

single-layer case. Figure 2.12 compares the sensitivities obtained from the model. Sensitivity increases by 100% passing from a single-layer ($S = 0.09 fF/kPa$) to two-layers ($S = 0.18 fF/kPa$), and incrementing by 50% passing from a two-layers to a three-layers ($S = 0.27 fF/kPa$). Then for the four-layer and five-layers the sensitivities are respectively $S = 0.36 fF/kPa$ and $S = 0.45 fF/kPa$ having an enhancement of 33.3% from three-layers to four-layers and 25% going from four-layers to five-layers. Therefore passing from a single-layer configuration to a five-layers one the sensitivity improves by 400%.

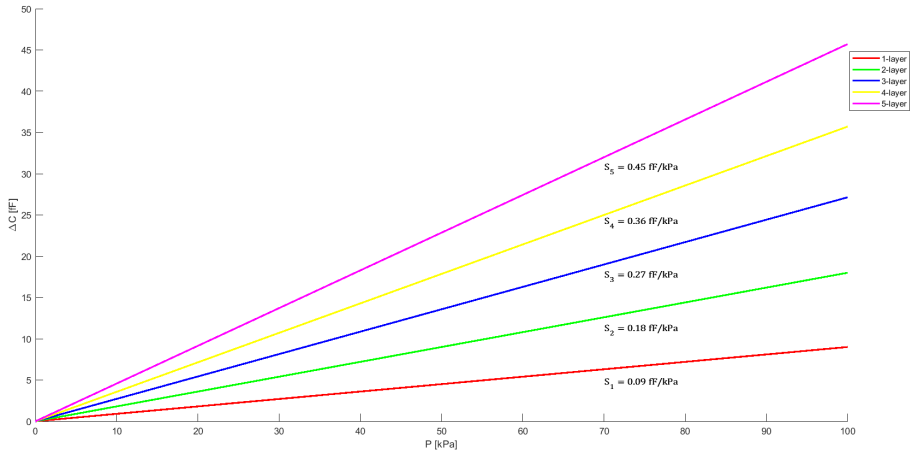

Figure 2.12 Finite element response with the corresponding sensitivity in the case of one-layer, two-layers, three-layers, four-layers and five-layers sensors assuming a linear model for the dielectric material.

The experimental characterization presented in the following sections reports higher sensitivity values for screen-printed sensors. This difference is expected, as the FEM model simplifies the sensor structure by assuming an air dielectric and by attributing deformation mainly to the electrode layers. Nonetheless, the simulations provide useful evidence that the sensitivity trend introduced by vertical stacking remains consistent when material parameters and fabrication constraints change.

2.5 Experimental Characterization of Inkjet-Printed Multilayer Sensors

The numerical results presented in Section 2.4.1 were experimentally validated through the fabrication and characterization of inkjet-printed multilayer capacitive tactile sensors. This section describes the fabrication process, the experimental setup, and the characterization of the sensors, with particular attention to the sensitivity enhancement introduced by vertical stacking.
The experimental analysis aims to confirm the trends predicted by the analytical model and FEM simulations, and to quantify the sensor performance under controlled loading conditions.

2.5.1 Fabrication Process of Inkjet-Printed Multilayer Sensors

The inkjet-printed multilayer capacitive tactile sensors were fabricated following the process described in *Staiano et al. (2023)*. The fabrication approach was selected to realize vertically stacked capacitive structures while preserving a compact lateral footprint and precise layer alignment. Moreover this manufacturing technique, similarly to screen-printing, is low cost and compatible with scalable fabrication workflows, suitable characteristics for rapid prototyping.
Silver nanoparticle ink (Ag NP ink, SunTronic EMD5730) was used for the fabrication of the conductive electrodes inkjet printed on a suitably cleaned Kapton sheet (75 μm), while polydimethylsiloxane (PDMS Sylgard 184) was employed as dielectric material. The PDMS dielectric was prepared separately prior to deposition and subsequently spin-coated to obtain a uniform and well-controlled thickness. The PDMS base and the curing agent are mixed in a 10:1 ratio (base to catalyst) in all experiments and stirred for 2 min. Then, the PDMS is placed in vacuum desiccators for degassing (10–13 min). Then, a thin layer of PDMS has been deposited on the capacitor substrate by spin coating. As discussed in *Mikkonen et al. (2020)*, a thickness of 25 μm guarantees excellent electrical insulation between the conductive layers. The PDMS thickness mainly depends on spin speed and duration *(Lee et al. (2019),Lee et al. (2006))*. In this work, this thickness has been obtained by depositing in sequence two layers of PDMS, each obtained through a spin coating with a speed of 2000 r/min and a duration of 5 min. With these parameters, each layer has a thickness of $\approx 12\ \mu m$ and so the total dielectric thickness is $\approx 24\ \mu m$.
Each sensing layer consists of a bottom electrode printed by inkjet, a spin-coated PDMS

dielectric layer, and a top electrode printed on a separate substrate. After curing, successive layers were mechanically stacked and bonded, as schematically illustrated in Fig. 2.13. This procedure was repeated to fabricate single-layer, two-layer, and three-layer capacitive tactile sensors while preserving the same lateral footprint showed in Figure 2.14.

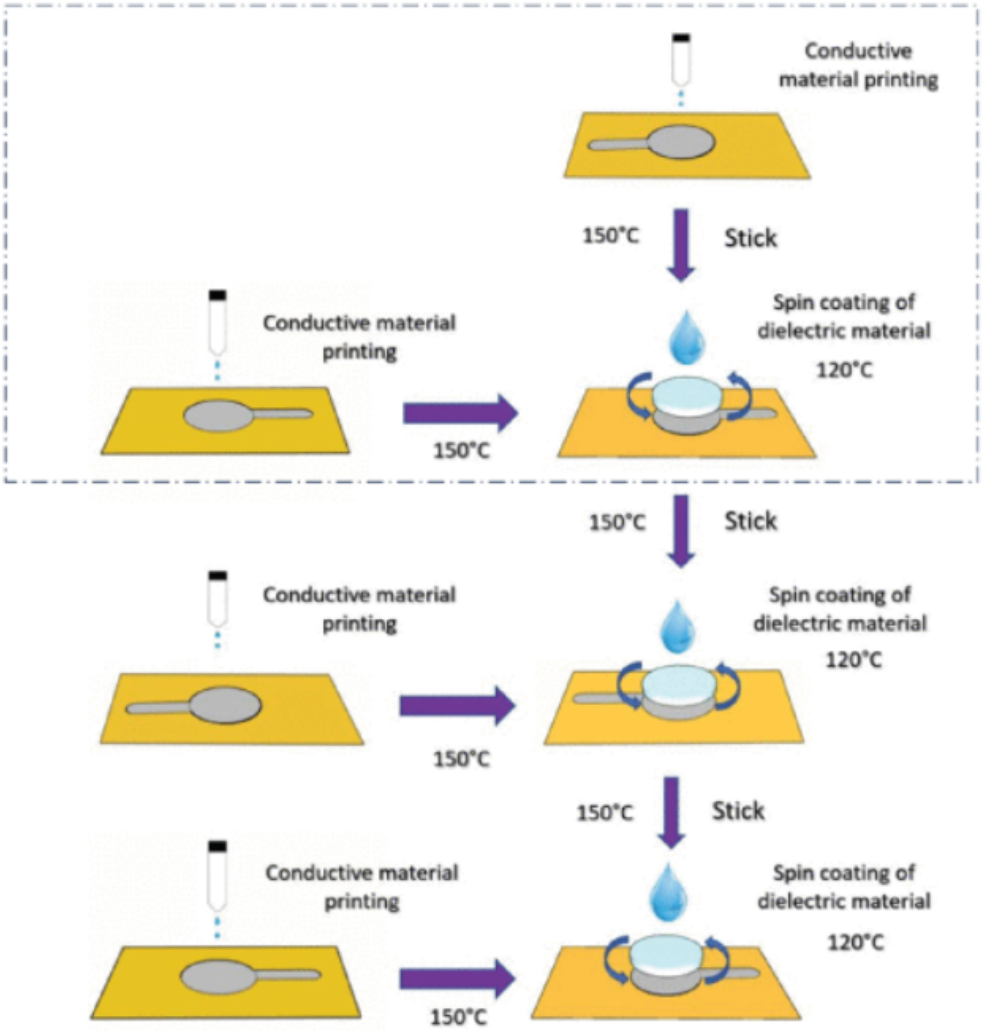

Figure 2.13 Schematic illustration of the sensor fabrication process. The dashed rectangle represents the method for a single capacitor. For the three-stacked capacitor, the process must be iterated.

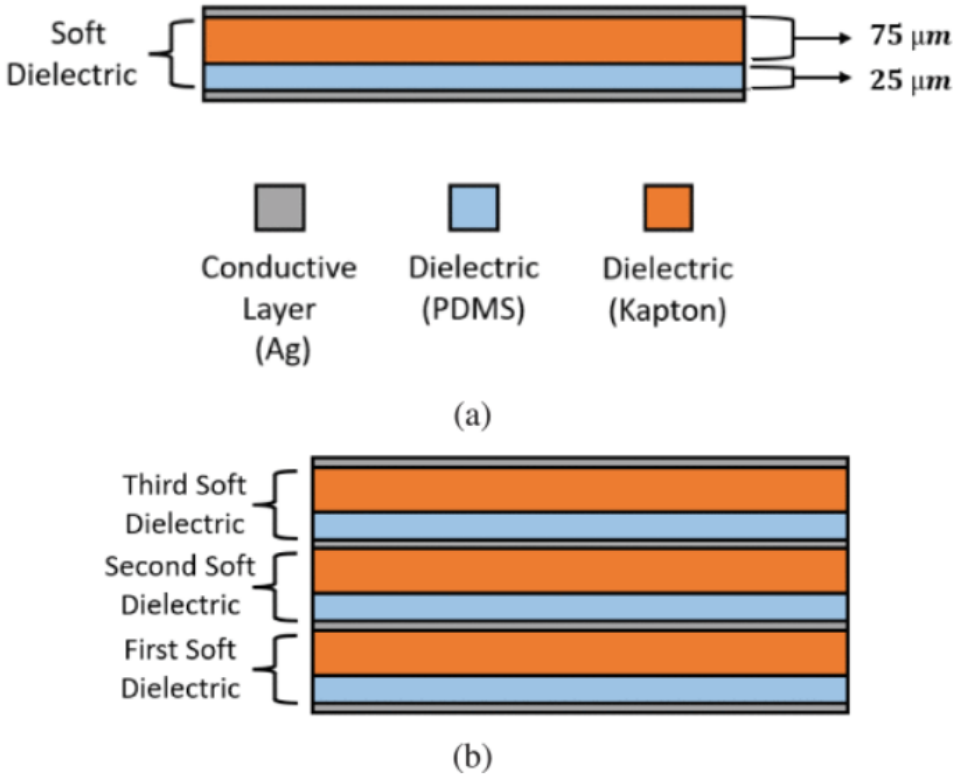

Figure 2.14 (a) Cross section of the structure for single dielectric. **(b)** Cross section of the structure for three dielectric layers.

Electrical interconnection between stacked electrodes was achieved by applying with a brush a silver conductive resin (MG Chemicals 842UR) through vertically aligned vias arranged in a sunburst geometry, as reported in *Staiano et al. (2023)*. Figure 2.15 represents the fabricated three-layers sensor with the spread electrical connection. This solution enables access to the internal electrodes of the multilayer structure but introduces limitations in terms of scalability, alignment accuracy, and fabrication repeatability. In particular, the manual realization of vertical vias becomes increasingly challenging as the number of layers or the sensor area increases.

While inkjet printing provides a cost-effective and flexible fabrication approach, these limitations motivate the transition toward screen-printed multilayer sensors. In the screen-printing process, vertical interconnections are realized through laser-drilled vias subsequently filled with silver paste. This approach improves alignment precision, repeatability, and robustness, and is therefore better suited for the fabrication of large-area and highly scalable multilayer tactile sensors.

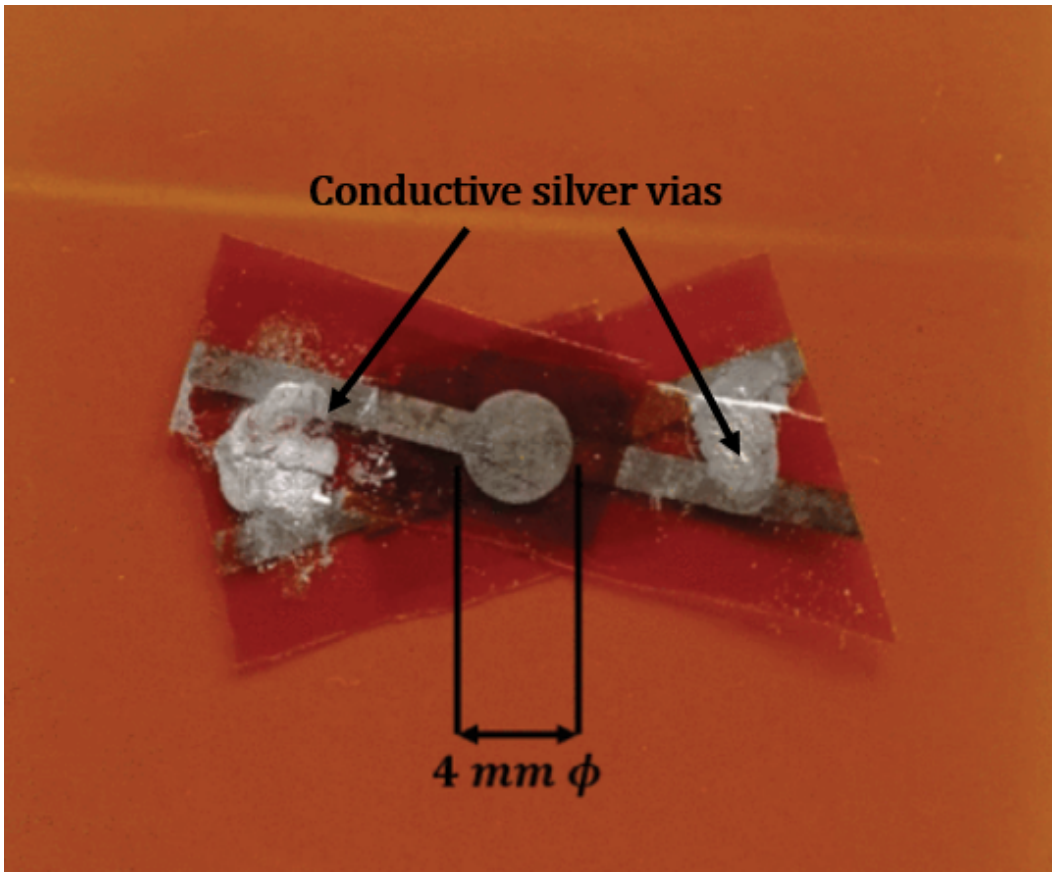

Figure 2.15 Manufactured three-layers sensor with brush-spread conductive vias.

2.5.2 Experimental Setup and Measurement Method

The experimental characterization of the inkjet-printed capacitive tactile sensors was performed under controlled loading conditions in order to evaluate the static response and sensitivity of the devices. The measurements were carried out following the methodology reported in *Staiano et al. (2023)*.

A normal force was applied to the sensor surface using calibrated weights, which were placed centrally on the active sensing area to ensure a uniform pressure distribution. The applied pressure was computed by dividing the applied force by the effective electrode area ($P = F/A$). The pressure range was selected to cover both gentle contact ($0 - 10\ kPa$) and manipulation-like ($10 - 100\ kPa$) interaction conditions, in agreement with the ranges considered in the FEM analysis *(Choi et al. (2020),Kurnaz et al. (2023))*.

Capacitance measurements were performed using a precision LCR meter operating at a fixed excitation frequency ($1\ kHz$) and voltage ($1\ V$), as specified in *Staiano et al. (2023)*. The sensor was connected to the measurement instrument through shielded cables in order to

reduce electromagnetic interference and parasitic capacitances.
For each sensor configuration (single-layer, two-layer, and three-layer), capacitance values were recorded as a function of the applied pressure. Multiple loading and unloading cycles were performed to assess repeatability and to reduce the influence of transient effects. The reported capacitance values correspond to the average of repeated measurements. Figure 2.16 shows the two experimental setups used for the the characterizations.

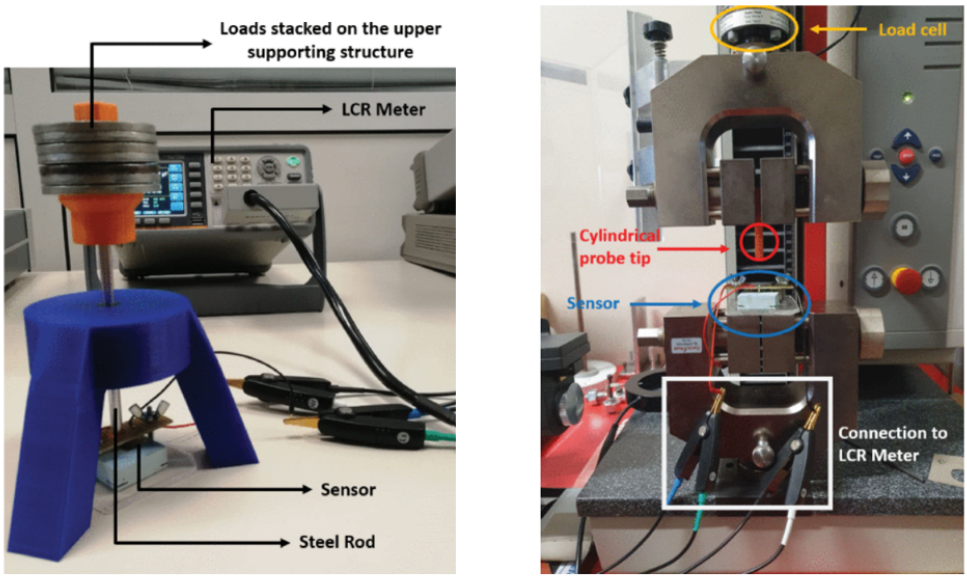

Figure 2.16 Experimental setups used for sensitivity **(a)** and dynamic range **(b)** characterization: **(a)** Mechanical hand-made test rig consisting of a vertical steel rod with a plastic cylindrical tip sustained by a linear bearing embedded in the supporting frame. The pressure applied to the capacitor is changed by adjusting the load by applying different weights on the upper supporting structure. **(b)** Materials testing machine (ZwickRoell zwickiLine Z0.5) equipped with a load cell.For each experiment, the cylindrical probe tip is initially set at 2.5 *mm* above the sensor. During the test, the probe is lowered toward the capacitor at a speed of 0.016 mm/s, until contact is made and the load cell measurements reach a threshold of 1 N

The sensitivity of the sensor was calculated as the slope of the capacitance variation with respect to the applied pressure, assuming a linear response within the investigated pressure range. This definition is consistent with the analytical model introduced in Section 2.3 and with the numerical analysis presented in Section 2.4.1. Also the dynamic range of each sensor was compared by measuring the range of the normalized capacitance ($\Delta C/C_0$) under multiple loading-unloading cycles.

All measurements were conducted at room temperature, and environmental conditions were kept constant throughout the experimental experiments to ensure consistency across different sensor configurations.

2.5.3 Experimental Characterization

The experimental characterization of the inkjet-printed capacitive tactile sensors was carried out to evaluate their response under applied pressure and to assess the performance improvements introduced by vertical stacking. Single-layer, two-layers, and three-layers sensors were characterized under identical experimental conditions using the setups described in Section 2.5.2.

The experimental analysis includes the measurement of the pressure–capacitance response, the evaluation of sensor sensitivity, and the assessment of the dynamic range. The results are presented in terms of both absolute capacitance variation and normalized capacitance change, consistently with the definitions adopted in *Staiano et al. (2023)*. The experimental findings are then compared with the analytical predictions and the FEM results discussed in Sections 2.3 and 2.4.1.

Figure 2.17 shows the change in capacitance with respect to the applied pressure for each sensor type. Here, the sensitivity has been extracted over two adjacent pressure ranges $0-30$ *kPa* and $35-100$ *kPa*. As it is possible to notice, in all the cases the sensitivity is higher in the first linear range, and after it decreases as the dielectric layer gets compressed and becomes less compliant. Table 2.3 compares the computed sensitivities in the first linear region of each sensor and their correspondent increase in percentage. These outcomes are consistent with the results obtained in simulation as described in Section 2.4.1.

Configuration	**Sensitivity [fF/kPa]**	**Sensitivity Increase**
Single-layer	5.75	–
Two-layers	19.3	+235.6% (vs. single-layer)
Three-layers	23.7	+22.79% (vs. two-layers)

Table 2.3 Experimental sensitivity values for inkjet-printed capacitive tactile sensors with different numbers of stacked layers.

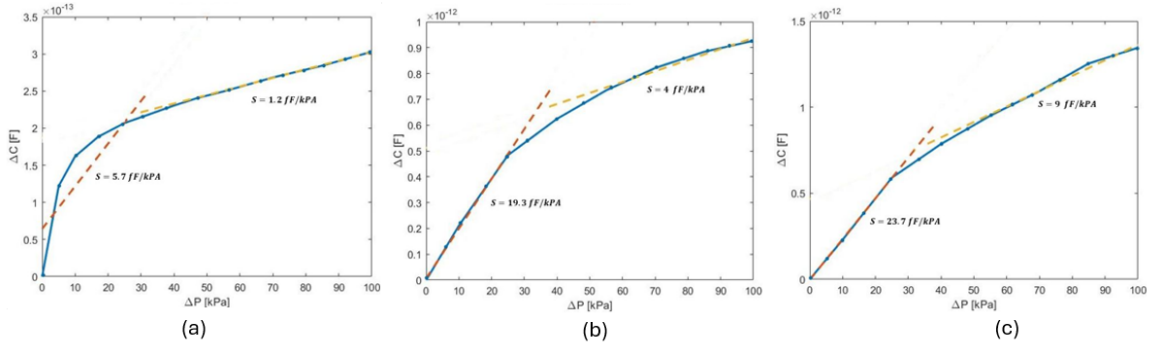

Figure 2.17 (a) Experimental sensor output in the case of the one-layer capacitive sensor. Output in terms of ΔC with the corresponding sensitivity in the two regions $[0-30\ kPa]$ $[35-100\ kPa]$. **(b)** Experimental sensor output in the case of the two-layers capacitive sensor. **(c)** Experimental sensor output in the case of the three-layers capacitive sensor.

Regarding the dynamics Figure 2.18 reports the maximum and minimum value of the normalized capacitance change and Table 2.4 compares the percentage variation of each sensor demonstrating that the dynamic range of the sensor is higher in case of parallel capacitors stacked together.

Configuration	**Dynamic Range** [%]
Single-layer	4.7 %
Two-layers	10.4 %
Three-layers	32.4 %

Table 2.4 Experimental dynamic range values for inkjet-printed capacitive tactile sensors with different numbers of stacked layers.

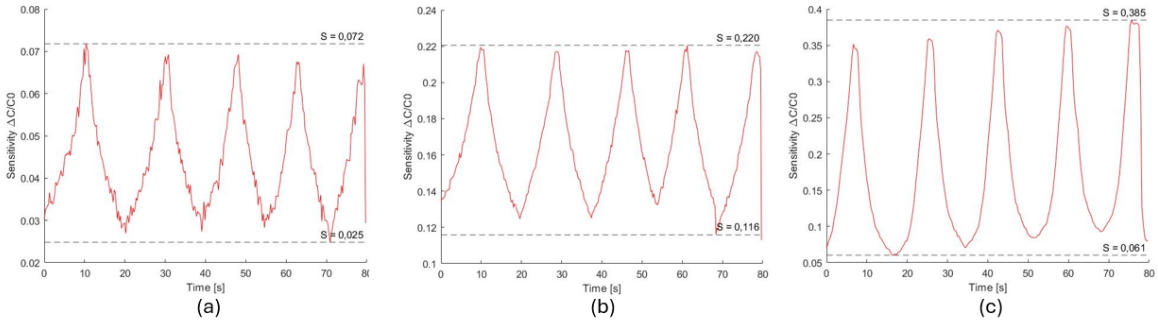

Figure 2.18 (a) Experimental sensor output in the case of the one-layer capacitive sensor. Output in terms of $\Delta C/C_0$ over the time period of the load-unload cycles. **(b)** Experimental sensor output in the case of the two-layers capacitive sensor. **(c)** Experimental sensor output in the case of the three-layers capacitive sensor.

2.5.4 Discussion and Comparison with FEM Results

The experimental results presented in the previous section confirm the main trends predicted by the analytical model and the FEM simulations. In particular, the pressure–capacitance response exhibits an approximately linear behavior within the low-pressure range, followed by a progressive reduction in sensitivity at higher pressures due to the increased compression of the dielectric layer. This behavior is consistent with the assumptions of linear elastic deformation adopted in the analytical formulation and with the numerical results discussed in Section 2.4.1.

The experimentally measured sensitivity values show a clear increase with the number of stacked layers. The transition from a single-layer to a two-layer configuration leads to a substantial sensitivity improvement, while the addition of a third layer provides a further, though smaller, increase. This trend closely matches the behavior predicted by both the analytical spring-in-series model and the FEM simulations, confirming that vertical stacking is an effective strategy to enhance sensitivity without modifying the lateral footprint of the sensor.

Table 2.5 highlights the quantitative comparison between FEM simulations and experimental results in terms of sensitivity scaling. While the absolute sensitivity values differ due to the simplified assumptions adopted in the numerical model, both approaches consistently predict a significant sensitivity increase when moving from single-layer to multilayer configurations.

Configuration	**Sensitivity FEM** [fF/kPa]	**Sensitivity Exp.** [fF/kPa]	**Increase FEM**	**Increase Exp.**
Single-layer	8.9	5.75	–	–
Two-layers	16.9	19.3	+90%	+235%
Three-layers	25.0	23.7	+48%	+23%

Table 2.5 Comparison between simulated (FEM) and experimental sensitivity values for inkjet-printed capacitive tactile sensors with different numbers of stacked layers. Percentage increases are reported with respect to the previous configuration.

The experimental dynamic range also increases with the number of stacked layers, as evidenced by the normalized capacitance variation measured during loading–unloading cycles. This result indicates that vertically stacked configurations not only improve sensitivity but also extend the usable operating range of the sensor. The observed increase in dynamic range is consistent with the parallel contribution of multiple capacitive elements, as described in the analytical model.

Overall, the experimental characterization confirms the validity of the analytical and numerical models and demonstrates that vertically stacked capacitive tactile sensors fabricated via inkjet printing exhibit improved sensitivity and dynamic range. These results provide a solid reference for the extension of the proposed architecture to alternative fabrication technologies, which are discussed in the following sections.

2.6 Screen-Printed Multilayer Capacitive Tactile Sensors

The fabrication approach adopted for inkjet-printed multilayer sensors demonstrated the effectiveness of vertical stacking in improving both sensitivity and dynamic range. However, as discussed in Section 2.5.1, the manual realization of vertical interconnections limits scalability, alignment accuracy, and fabrication repeatability, especially when extending the architecture to larger sensing areas or higher numbers of stacked layers.// To overcome these limitations, screen-printing technology was investigated as an alternative fabrication approach. Screen printing offers a cost-effective and scalable manufacturing process, well suited for large-area tactile sensors and for the integration of vertical interconnections through automated procedures. This transition is motivated by the need to move from laboratory-scale prototypes toward robust and reproducible tactile sensing systems.

2.6.1 Fabrication Process of Screen-Printed Multilayer Sensors

Screen-printed multilayer capacitive tactile sensors were fabricated following the process illustrated in Fig. 2.19, which outlines the steps adopted to realize scalable and repeatable multilayer structures. The fabrication approach relies on commercially available screen-printable inks and plastic substrates, selected to ensure compatibility among materials and suitability for multilayer lamination. The conductive electrode layers were realized by screen printing a silver-based ink *(CXT, Nagase)* onto PET substrates with a thickness of 50 μm. The printed electrodes have a circular geometry with a diameter of 6 mm and are arranged in a 3×3 matrix configuration. After deposition, the conductive layers were thermally cured at 120°C to achieve the required electrical conductivity and adhesion to the substrate.
The dielectric structure of the sensor was formed using a tactile ink formulation, such as a UV-curable Braille varnish *(Marabu)*, which was screen printed to define the air gap cavities and the supporting pillars. These structures are responsible for reducing the effective distance between opposing electrodes when an external force is applied, thereby increasing the sensor capacitance. The tactile ink was cured via UV light exposure to ensure mechanical stability and repeatability of the printed features.
An adhesive ink layer was then screen printed to enable lamination between successive PET substrates. The D142 adhesive ink from Kiwo was chosen, which was thermally dried at temperatures below 70°C. The lamination process allows multiple functional layers—conductive, dielectric, and adhesive—to be assembled into a single capacitive unit while maintaining a controlled and repeatable geometry.

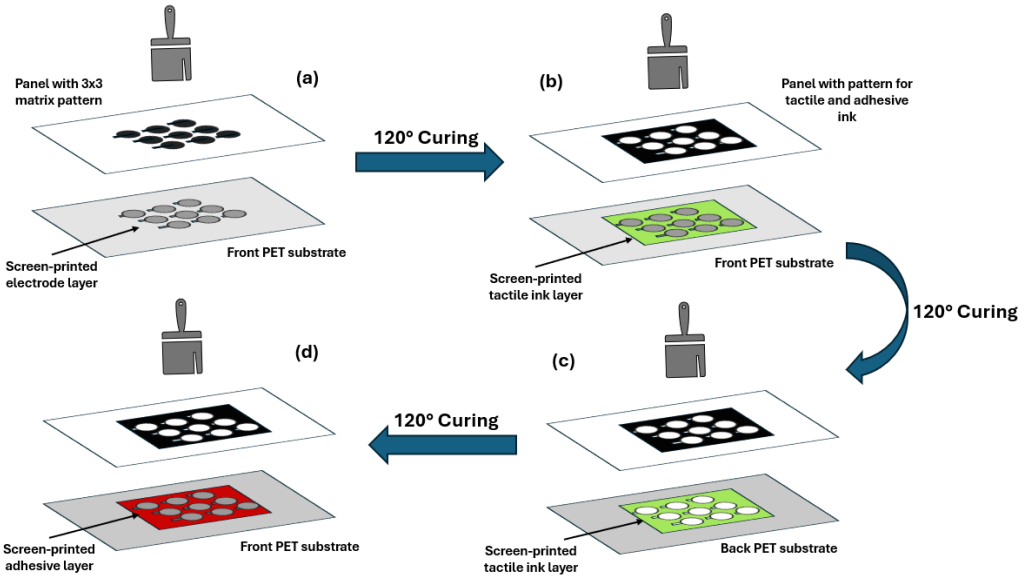

Figure 2.19 Overview of the screen-printing process: **(a)** First a layer of silver ink ($\approx 5-10\ \mu m$) was brushed on the panel with the 3x3 matrix pattern to screen-print the electrodes on the front of the 50 μm PET substrate. **(b)** After curing the sample at 120°C we brushed a layer of tactile ink (70 μm) to create the air gap between electrodes **(c)** After another step of curing at 120°C we flipped the PET substrate and screen printed another layer of tactile ink (70 μm) to keep the thickness of the dielectric after the stacking. **(d)** Finally a layer of adhesive ($\approx 20-30\ \mu m$) was applied to be able to attach the electrode layers.

To realize vertically stacked multilayer configurations, individual sensor layers were aligned and laminated after the fabrication of the vertical vias. Vertical electrical interconnections between layers were implemented by laser drilling through-holes with a diameter of 1 mm in a designed pattern. The laser-drilled vias provide precise alignment across layers and enable reproducible fabrication of multilayer stacks as depicted in Fig.2.20. After lamination, the vias were filled with silver conductive paste to establish reliable electrical connections between internal electrodes, as shown in the cross-sectional view in Fig. 2.21.

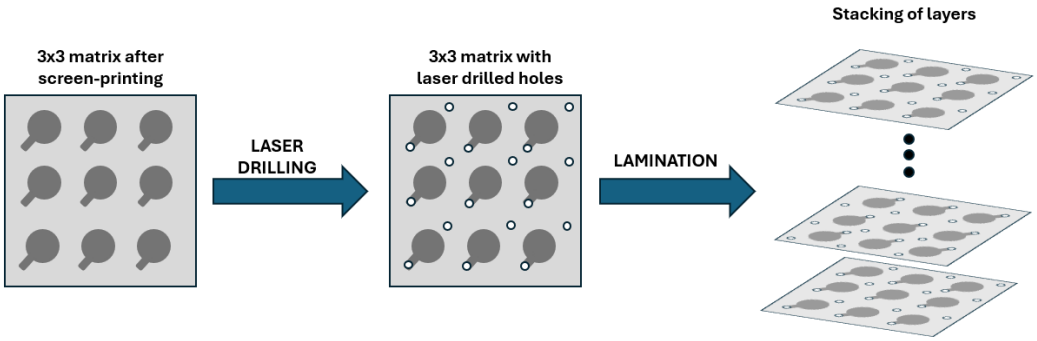

Figure 2.20 Top view of the screen-printed 3x3 matrix sample and its laser-drilling result then ready for the stacking process through lamination.

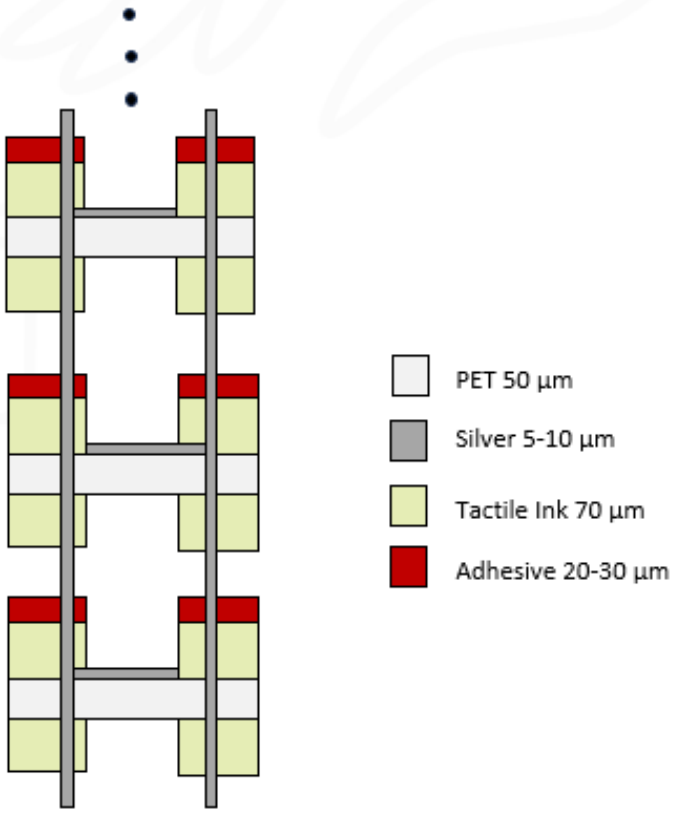

Figure 2.21 Cross section of the stacking of the multilayer capacitive tactile sensors.

The complete fabrication process—screen printing, curing, laser drilling, lamination, and via filling—enables the realization of scalable multilayer capacitive tactile sensors with improved alignment accuracy and fabrication repeatability. This approach overcomes the limitations associated with manual via formation in inkjet-printed sensors and represents a key step toward the development of large-area tactile sensor arrays. Fig. 2.22 illustrates the fabricated screen-printed multilayer capacitive tactile sensors from 1 to 5 capacitive layers.

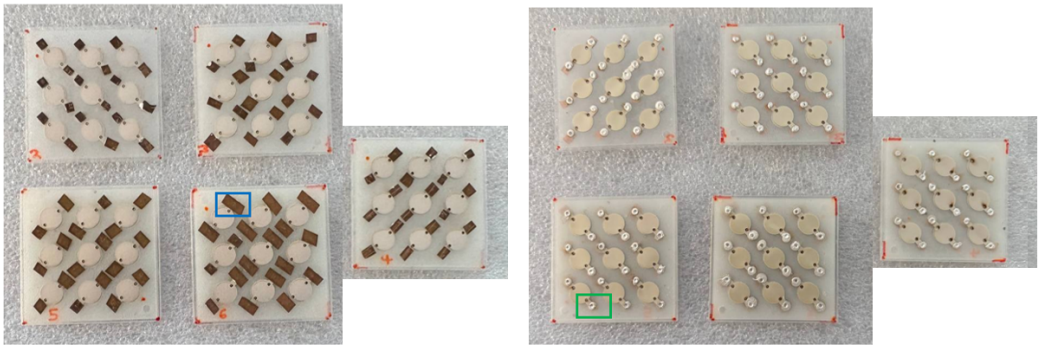

Figure 2.22 (a) Top View of the multilayer capacitive tactile sensors from 1 to 5 layers. In blue it is highlighted the copper pad attached on the vias for electrical connections. **(b)** Bottom View of the multilayer capacitive tactile sensors from 1 to 5 layers. In green it is highlighted the laser drilled via filled with silver.

2.6.2 Experimental Setup and Measurement Method

The experimental characterization of the screen-printed multilayer capacitive tactile sensors was performed using a materials testing machine (ZwickRoell zwickiLine Z0.5), similarly to the setup adopted for inkjet-printed sensors in Section 2.5.2 and shown in Fig. 2.23. This choice ensures consistent loading conditions and allows a direct comparison between the two fabrication technologies.

During the experiments, a normal force was applied to the sensor surface using a cylindrical probe mounted on the Zwick machine. The probe was aligned with the center of the active sensing area to ensure uniform pressure distribution. The applied pressure was computed by dividing the measured force by the effective electrode area, considering the same pressure ranges ($0-10$ *kPa* and $10-100$ *kPa*) adopted in Section 2.5.2. The probe was initially positioned above the sensor surface and then lowered at a constant speed until the desired force level was reached.

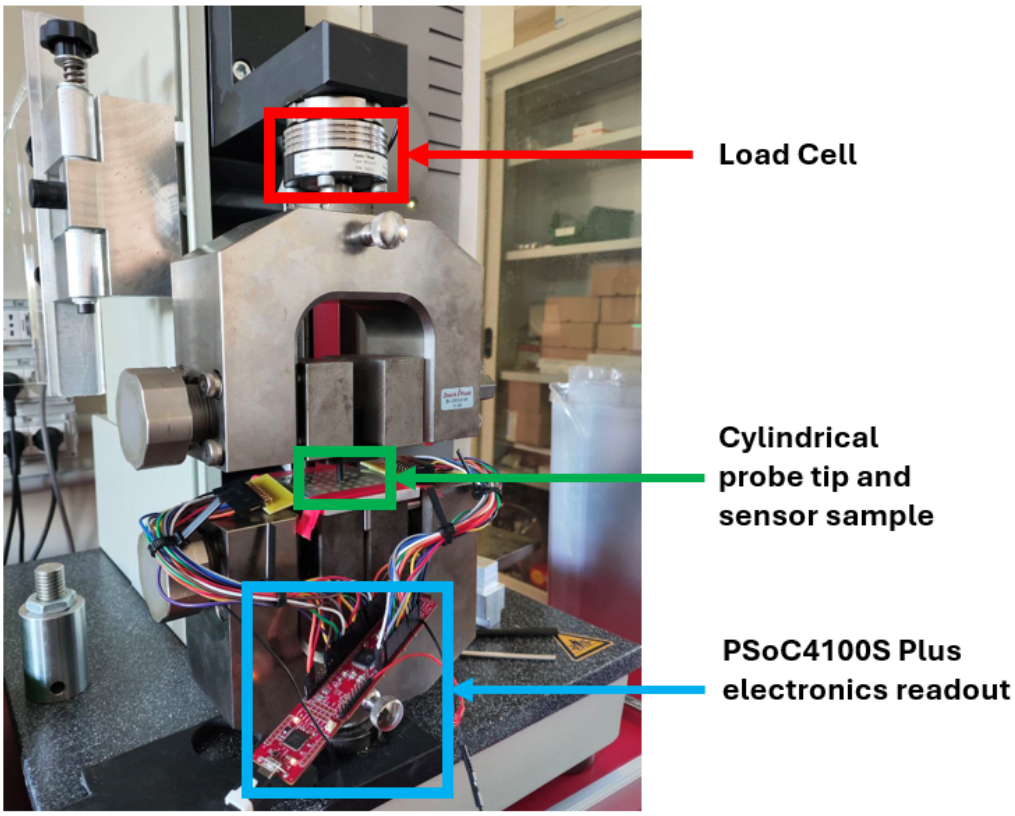

Figure 2.23 Experimental setup for the sensitivity characterization. For the readout a PSoC4100s Plus board has been used

In contrast to the inkjet-printed sensor characterization, the capacitance acquisition for the screen-printed sensors was performed using a custom electronic readout based on a PSoC4100S Plus microcontroller. This board was selected because it represents the target embedded platform for the final integration of the tactile sensing system. The PSoC4100S Plus is capable of measuring capacitance values at a sampling rate of 1 kHz per channel, with a resolution of approximately 0.3 fF, making it suitable for high-resolution tactile sensing applications.

Each sensor configuration, ranging from one to five stacked capacitive layers, was connected to the PSoC-based acquisition board through dedicated wiring and shielded connections to minimize parasitic capacitances and electromagnetic interference. Capacitance data were recorded continuously during loading and unloading cycles, allowing the evaluation of the sensor response.

The sensitivity of the screen-printed sensors was extracted from the slope of the capacitance–pressure curve within the linear operating region. The use of an embedded

acquisition system enables a more realistic assessment of sensor performance under conditions representative of final robotic integration.

2.6.3 Experimental Characterization and FEM Comparison

The experimental characterization of the screen-printed multilayer capacitive tactile sensors focused on the evaluation of sensitivity as a function of the applied pressure. Sensors with an increasing number of stacked capacitive layers, ranging from one to five layers, were tested under identical loading conditions using the setup described in Section 2.6.2.

Figure 2.24 reports the pressure–capacitance response for each configuration. As observed for the inkjet-printed sensors, the capacitance response exhibits a higher slope at low pressure levels, followed by a reduced sensitivity at higher pressures as the mechanical structure becomes less compliant. Sensitivity values were therefore extracted in the initial linear region of the response curve.

The experimental results show a clear and systematic increase in sensitivity as the number of stacked layers increases. This behavior confirms that vertical stacking effectively enhances the capacitive response also in the case of screen-printed sensors, despite the higher stiffness associated with PET substrates and air-gap-based dielectric structures.

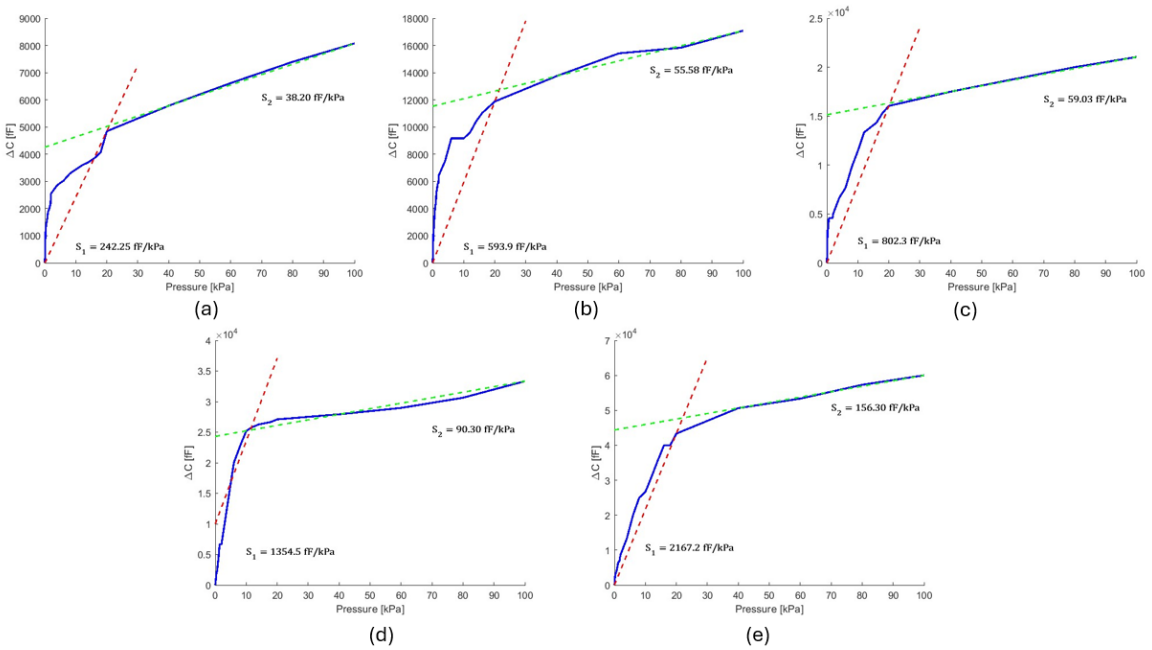

Figure 2.24 Experimental pressure–capacitance response of screen-printed multilayer capacitive tactile sensors: **(a)** one-layer, **(b)** two-layers, **(c)** three-layers, **(d)** four-layers, and **(e)** five-layers configurations. Sensitivity values are extracted in the initial linear region.

Table 2.6 summarizes the extracted sensitivity values for each configuration, together with the corresponding percentage increase with respect to the previous stacking level. The results highlight a monotonic growth of sensitivity with the number of stacked layers, demonstrating the scalability of the proposed architecture.

Configuration	**Sensitivity [fF/kPa]**	**Sensitivity Increase**
Single-layer	242.25	–
Two-layers	593.9	+145.2% (vs. single-layer)
Three-layers	802.3	+35.09% (vs. two-layers)
Four-layers	1354.5	+68.83% (vs. two-layers)
Five-layers	2167.2	+60.66% (vs. two-layers)

Table 2.6 Experimental sensitivity values for screen-printed multilayer capacitive tactile sensors with increasing number of stacked layers.

Configuration	**Sensitivity FEM** [fF/kPa]	**Sensitivity Exp.** [fF/kPa]	**Increase FEM**	**Increase Exp.**
One-layer	0.09	242.25	–	–
Two-layers	0.18	593.9	+100%	+145.2%
Three-layers	0.27	802.3	+50%	+35.09%
Four-layers	0.36	1354.5	+33.3%	+68.83%
Five-layers	0.45	2167.2	+25%	+60.66%

Table 2.7 Comparison between simulated (FEM) and experimental sensitivity values for screen-printed multilayer capacitive tactile sensors with increasing number of stacked layers. Percentage increases are reported with respect to the previous configuration.

These results confirm that vertical stacking provides a robust and scalable strategy to enhance sensitivity in screen-printed capacitive tactile sensors. The observed trend of increasing sensitivity with the number of stacked layers is consistent with both the analytical model and the FEM analysis reported for reference in Table 2.7. The ability to extend the stacking approach up to five layers with repeatable performance highlights the suitability of screen printing for the realization of large-area tactile sensing systems.
However, a significant quantitative discrepancy is observed between the FEM-predicted and experimentally measured absolute sensitivity values, with the experimental results exceeding the simulated ones by several orders of magnitude. This divergence can be attributed to a combination of simplifying assumptions adopted in the numerical model that do not fully capture the mechanical behavior of the fabricated devices:

- The FEM model represents the dielectric region as a homogeneous linear elastic solid with the mechanical properties of PET, whereas in the actual sensor the dielectric is an air gap bounded by thin and flexible PET substrates. Under applied pressure, the air cavity collapses significantly more than a solid elastic layer would, producing a substantially larger capacitance variation at low forces.
- The electrodes are treated as rigid boundaries in the simulation, neglecting bending and local deformation effects that in practice contribute to additional air-gap reduction.
- The FEM analysis assumes linear elastic behavior throughout the operating range, while the real structure exhibits nonlinear effects arising from the mechanical response of the tactile ink pillars, the thin PET substrates, and their interaction during compression.
- The simplified geometry adopted in the simulations does not reproduce the full laminated architecture of the fabricated sensor, including the presence of adhesive layers, printed pillars, and the boundary conditions introduced by the lamination process.

Despite these limitations, the FEM model successfully captures the qualitative scaling behavior of the stacked architecture. A more refined numerical model incorporating air-gap mechanics, substrate flexibility, and nonlinear material response would be needed to achieve quantitative agreement with the experimental data, and is identified as a direction for future development.

2.7 Chapter Summary and Key Contributions

This chapter presented the development, modeling, fabrication, and characterization of multilayer capacitive tactile sensors based on a vertical stacking architecture. An analytical model was first introduced to describe the mechanical–electrical transduction mechanism of stacked capacitive structures, highlighting the role of material properties and geometric parameters in determining sensor sensitivity.

Finite element simulations were then employed to validate the analytical formulation and to investigate the influence of vertical stacking under different material assumptions, representative of both inkjet-printed and screen-printed fabrication technologies. The numerical results confirmed that stacking multiple capacitive layers leads to a systematic increase in sensitivity, independently of the specific dielectric configuration.

Two fabrication approaches were subsequently investigated. Inkjet printing was adopted to realize compact multilayer sensors and to experimentally validate the stacking concept, demonstrating significant improvements in sensitivity and dynamic range. Screen printing was then introduced as a scalable alternative, enabling improved alignment accuracy, fabrication repeatability, and the realization of multilayer sensors with up to five stacked capacitive layers.

Experimental results obtained from both fabrication technologies confirmed the trends predicted by the analytical model and FEM simulations. Although absolute sensitivity values depend on materials and structural compliance, vertical stacking consistently proved to be an effective strategy for enhancing sensor performance. Moreover, the integration of screen-printed sensors with embedded readout electronics based on a PSoC4100S Plus microcontroller represents a key step toward the deployment of small and large-area tactile sensing systems.

Chapter 3

CySkin+ and EtherCAT-based Distributed Architectures

3.1 From Cyskin to CySkin+

The development of large-area tactile skins for robotic applications requires a system-level perspective that extends beyond the design and characterization of individual tactile sensors. While the multilayer capacitive tactile sensors presented in Chapter 2 provide an effective sensing building block, their deployment over extended robot surfaces introduces additional challenges related to scalability, mechanical integration, data acquisition, and system robustness. Recent research in tactile robotics highlights that these challenges increasingly dominate system performance as tactile sensing moves from localized interaction points toward whole-body coverage as showed in *Luo et al. (2025)* and *Zhiyu et al. (2025)*.

Early tactile skin concepts, such as CySkin developed by *Maiolino et al. (2013)*, were conceived to demonstrate the feasibility of distributed tactile sensing through modular sensing units arranged over curved and complex robot surfaces. CySkin introduced a patch-based approach, in which multiple tactile elements are grouped into mechanically flexible modules that can be attached to different parts of a robot body, enabling conformability and spatial distribution of tactile sensing. This architectural choice represented an important step toward whole-body tactile perception and provided an experimental platform for investigating distributed tactile sensing principles. Fig. 3.1 shows in detail the CySkin technology.

However, as tactile skins evolve toward larger sensing areas and higher sensor densities, several limitations of early CySkin architectures become evident. In particular, substrate selection, material durability, wiring complexity, and data routing emerge as critical bottlenecks. As the number of tactile elements increases, mechanical fragility, assembly tolerances,

and signal integrity issues increasingly affect system reliability and repeatability. Similar challenges have been widely reported in recent studies on large-area and flexible tactile sensing systems, where the transition from laboratory-scale prototypes to robust robotic skins remains a central open problem as stated in *Yang et al. (2025)*.

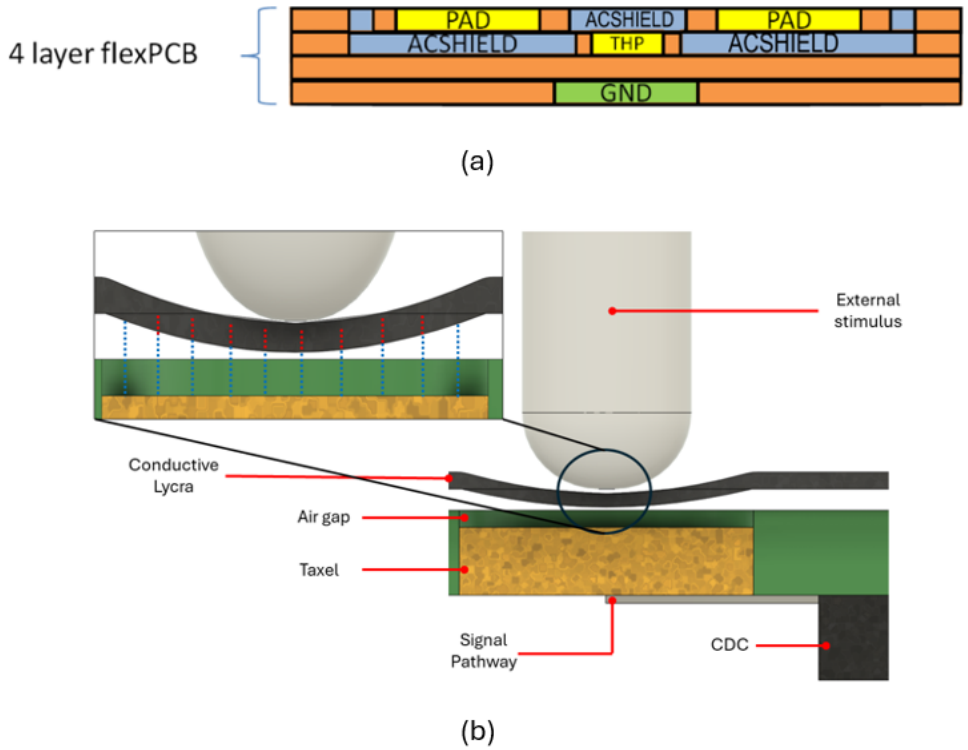

Figure 3.1 (a) A simplified vertical section of the CySkin modules, **(b)** Detail of CySkin's transduction principle. The CDC samples the capacitance variation induced by the deformation of the lycra layer when a contact occurs.

CySkin+ represents an evolution of the original CySkin concept, driven by the need to address these architectural and material limitations while preserving the advantages of modularity and flexibility. Rather than introducing a fundamentally new sensing principle, CySkin+ focuses on improving the structural and material aspects of tactile skin patches, including substrate replacement, material trade-offs, and patch-level design choices. These improvements aim to enhance mechanical robustness, fabrication repeatability, and compatibility with scalable manufacturing processes, which are essential requirements for next-generation collaborative and service robots.
From a system perspective, the transition from CySkin to CySkin+ reflects a shift from proof-of-concept tactile patches toward architectures that can support large-area tactile

coverage. This evolution naturally introduces new requirements at the level of data acquisition and communication, as the number of sensing nodes grows and real-time interaction becomes a fundamental constraint. Recent work on body-scale robotic skins and distributed multimodal sensing architectures further emphasizes the importance of scalable acquisition strategies and efficient data aggregation mechanisms for practical deployment as in Giovinazzo et al. (2024a). Following sections analyze design choices, fabrication, characterizations and analysis between CySkin and CySkin+.

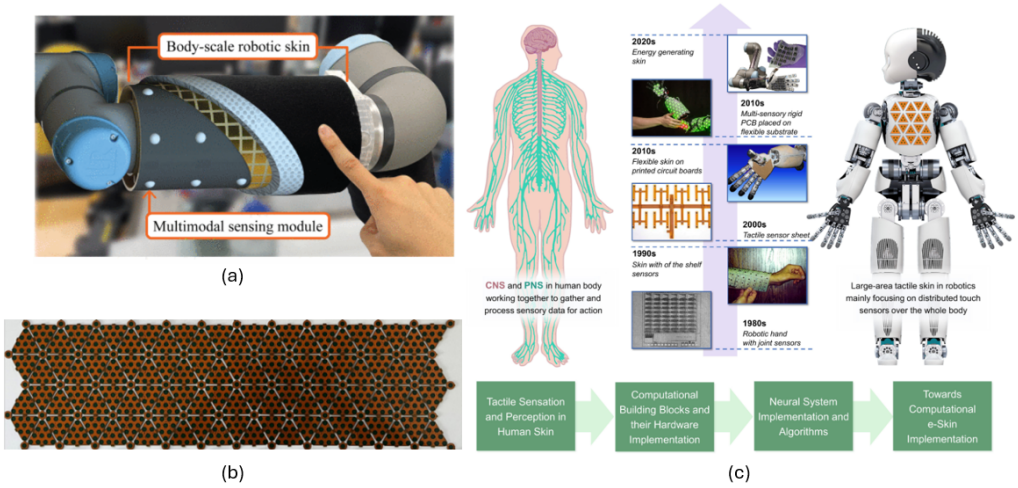

Figure 3.2 (a) Body-scale robotic skin presented in *Yang et al. (2025)*, **(b)** CySkin panel used in ProxySKIN for robotic integration *Giovinazzo et al. (2024a)*, **(c)** Process from tactile perception in human toward large-area tactile skin *Liu et al. (2022)*

3.2 Substrate Replacement and Material Trade-offs

The transition from CySkin to CySkin+ was motivated not only by performance considerations, but also by practical constraints related to cost, manufacturing, and system integration. While the original CySkin architecture successfully demonstrated the feasibility of modular tactile patches, its reliance on textile-based substrates such as Lycra introduced significant limitations when considering large-area deployment and long-term robotic use.

When it comes to costs, the choice of substrate material plays a crucial role in determining the feasibility of large-area tactile skins. Textile-based substrates, such as Lycra, introduce significantly higher material costs when compared to polymer-based alternatives commonly used in printed electronics. This difference becomes increasingly relevant when tactile

sensing is extended from small patches to robot-scale surfaces, where material consumption grows proportionally with the covered area.
A quantitative comparison of representative substrate materials considered during the design of CySkin+ is reported in Table 3.1. The data highlight the strong cost advantage offered by polymer films such as Kapton, PET and TPU, which are not only more affordable but also better suited for scalable fabrication processes.

Substrate Material	**Cost [€/m^2]**
Lycra	117.80
Kapton 50 μm	27.98
TPU 100 μm	6.80
PET 125 μm	6.56
PET 50 μm	0.94

Table 3.1 Approximate cost comparison of substrate materials considered for CySkin and CySkin+ designs. Values highlight the economic impact of substrate selection when scaling tactile skins to large areas.

Besides the economic advantage, polymer-based substrates provide improved dimensional stability and compatibility with printing and lamination processes, making them more suitable for repeatable manufacturing and mechanical integration on robotic platforms.

3.2.1 FEM Analysis of Substrate Replacement

Finite Element Method (FEM) simulations were performed using COMSOL Multiphysics to quantitatively investigate the impact of substrate material on the mechanical response and sensitivity of CySkin+ tactile patches. The numerical analysis supports the substrate replacement strategy introduced in Section 3.2 and provides a direct link between material properties, sensor deformation, and sensitivity.
The FEM model simplify the layered structure of a designed CySkin+ tactile taxel, as schematically illustrated in Fig. 3.3. The model includes the studied flexible substrate, a conductive electrode, a dielectric structure designed to enhance local deformation, and the underlying CySkin flexible PCB. A circular active sensing area with a diameter of 3.5 *mm* was considered, consistent with the designed fabrication of CySkin+ patches. A uniform normal pressure was applied to the top surface of the dielectric structure ranging from 0 up to 100 *kPa*, while appropriate boundary conditions were imposed to constrain the patch edges. Figure 3.4 shows a representative FEM result illustrating the displacement magnitude distribution under applied pressure.

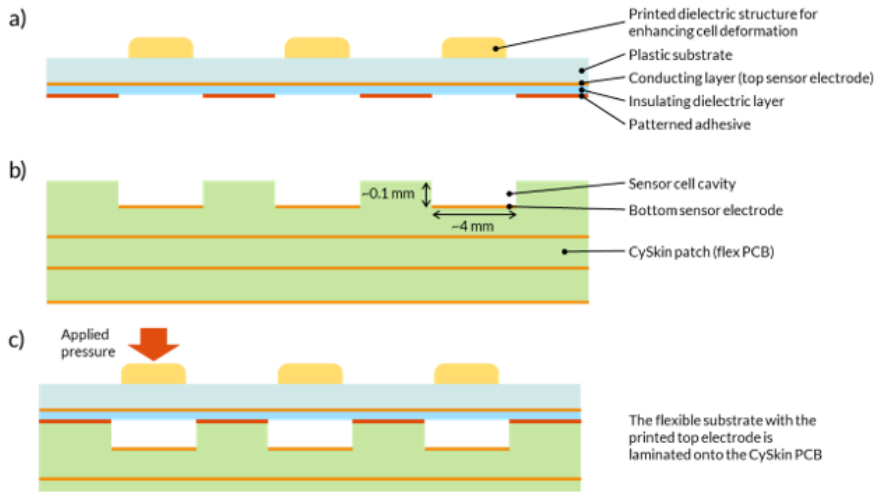

Figure 3.3 Schematic illustrating the CySkin+ concept. The upper layer **(a)**, which is manufactured by printing and laminated onto the flexible CySkin PCBs **(b)**, serves as the electronic ground plane in the completed CySkin+ modules **(c)**.

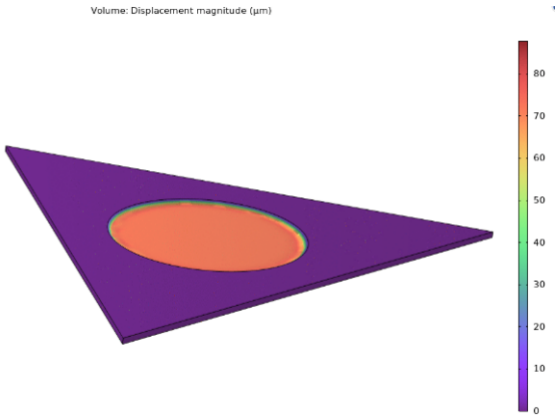

Figure 3.4 Simulate displacement of the FEM model used for each substrate study.

To evaluate the influence of substrate material, a parametric study was conducted by varying the substrate elastic properties while keeping the sensor geometry unchanged. The materials considered in the analysis were **PET**, **TPU** and **Kapton**, selected to span a wide range of stiffness values representative of polymer films. The mechanical properties used in the simulations are summarized in Table 3.2.

For each substrate configuration, the pressure–capacitance response was computed and the sensitivity was extracted in the linear operating region. Figure 3.5 and Table 3.3 compares the simulated capacitance variation as a function of pressure for different substrate materials and thicknesses.

Substrate	**Young's Modulus** E	**Poisson's Ratio** ν
PET	4 GPa	0.33
TPU	50 MPa	0.49
Kapton	3.2 GPa	0.34

Table 3.2 Mechanical properties of substrate materials used in the FEM analysis.

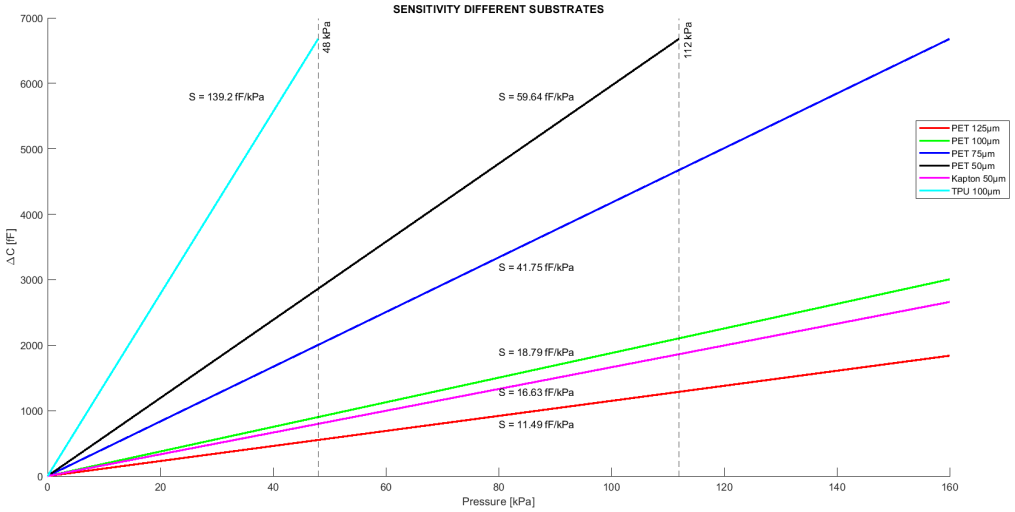

Figure 3.5 Computed sensitivity of each substrate investigated for CySkin+.

The results clearly demonstrate that substrate compliance has a strong influence on sensitivity. Softer substrates, such as TPU, allow larger deformations under the same applied pressure, leading to significantly higher capacitance variations. Conversely, stiffer substrates such as PET and Kapton restrict deformation and result in lower sensitivity values. This trend is consistent across the investigated pressure range and confirms that substrate selection represents a critical design parameter in CySkin+.

At the same time, the simulations highlight an important design trade-off. While highly compliant substrates maximize sensitivity, they may compromise mechanical robustness, alignment accuracy, and ease of integration on robotic structures. Stiffer polymer substrates, particularly thin PET films, provide a more balanced compromise between sensitivity, dimensional stability, and fabrication. These findings directly motivate the material choices adopted for CySkin+ and guide the manufacturing strategies and respective characterization discussed in the following section.

Substrate Material	Thickness [μm]	Sensitivity [fF/kPa]
PET	125	11.49
PET	100	18.79
PET	75	41.75
PET	50	59.64
Kapton	50	16.63
TPU	100	139.2

Table 3.3 Sensitivity values obtained from FEM simulations for different substrate materials and thicknesses. The active sensing area has a diameter of 3.5 mm.

3.3 CySkin+: Manufacturing

The substrate replacement strategy discussed in Section 3.2 requires experimental validation in order to assess its practical impact on tactile patch fabrication, integration, and performance. For this reason, CySkin+ tactile patches were manufactured and characterized using polymer-based substrates and fabrication techniques compatible with scalable production.

Compared to the original CySkin design, which relied on textile substrates and manual assembly steps, CySkin+ adopts polymer films and printing-based processes that provide improved dimensional stability and more controlled fabrication tolerances. These choices simplify mechanical integration on robotic structures and allow a more systematic evaluation of the influence of substrate material on sensor behavior.

This section describes the manufacturing process adopted for CySkin+ tactile patches, with particular focus on the design choices, materials, and fabrication steps introduced to replace the original textile-based solution. The CySkin+ manufacturing approach is discussed in relation to the substrate replacement strategy and the FEM analysis presented in Section 3.2, which guided the selection of materials and layer configurations suitable for scalable robotic skin applications.

3.3.1 Design and Manufacturing of CySkin+ Printed Layers

The CySkin+ architecture was conceived to replace the original textile-based outer electrode of CySkin with a fully printed and laminated electronic layer, improving manufacturability, robustness, and system integration while preserving the sensing principle of the original platform. The design is based on the reuse of the existing CySkin flexible PCB, which already incorporates air-gap cavities and bottom sensing electrodes, combined with an additional printed layer laminated on top of the PCB to form the capacitive sensing structure.

Figure 3.3 illustrates the operating principle of CySkin+. A flexible polymer substrate

carrying the printed outer electrode is laminated onto the CySkin patch. Between the two electrodes, printed dielectric and tactile structures locally enhance deformation when pressure is applied, effectively modulating the capacitance of each taxel without modifying the underlying CySkin electronics.
The printed layer replaces the conductive Lycra previously used in CySkin, addressing several limitations related to material cost, mechanical aging, and integration complexity. In CySkin+, the outer electrode and dielectric structures are realized using screen-printed functional inks on polymer substrates, enabling controlled layer thickness, precise pattern definition, and compatibility with scalable manufacturing processes.
The CySkin+ printed layer consists of four functional printed layers, whose layout and print order are shown in Fig. 3.6:

- **Silver conductive layer**, defining the outer pressure-sensing electrode pattern;
- **Dielectric insulating layer**, providing electrical isolation between electrodes;
- **Tactile ink layer**, printed on the backside to define air-gap cavities and local deformation features;
- **Adhesive layer**, enabling lamination onto the CySkin flexible PCB.

These layers are printed sequentially on flexible polymer substrates such as PET, Kapton, or TPU, depending on the mechanical requirements identified in the FEM analysis presented in Section 3.2. The print patterns are designed to match the triangular taxel arrangement of the CySkin PCB, ensuring one-to-one alignment between printed electrodes and underlying sensor cells.
Figure 3.6 shows the individual print layouts used for each functional layer, while Fig. 3.7 provides detailed views of the printed structures after fabrication and lamination. The printed patterns reproduce the triangular CySkin geometry, allowing direct electrical and mechanical coupling with the existing PCB without redesigning the sensor electronics.
After printing, the complete printed sheet is aligned and laminated onto the CySkin flexible PCB using a hot lamination process. Laser cutting is then used to define the final sheet outline, ventilation openings, and slits required for mechanical compliance and conformity to curved robot surfaces. Figure 3.7 shows both local alignment details at the taxel level and a full laminated CySkin+ sheet (approximately 23×12 cm^2), demonstrating the scalability of the proposed approach.

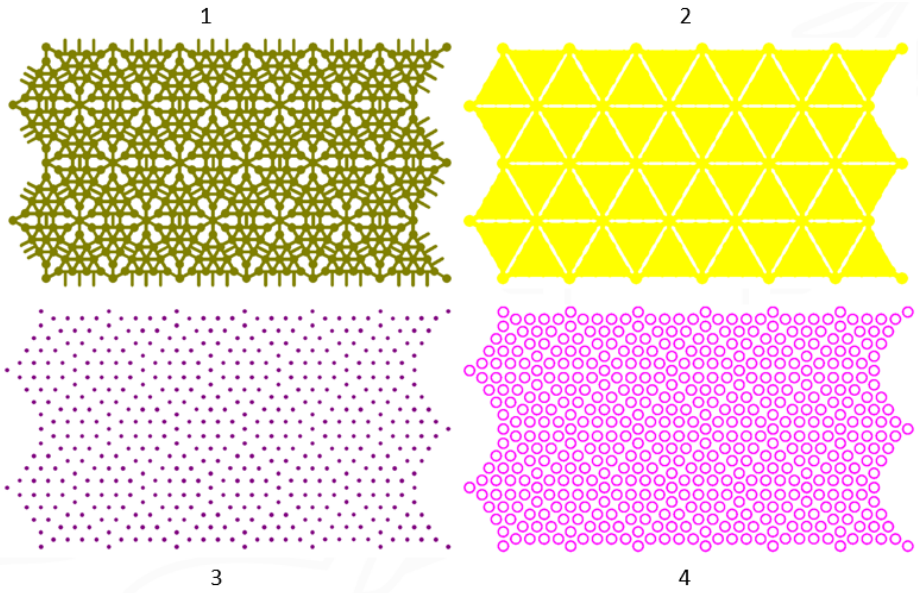

Figure 3.6 The layout of the CySkin+ design. Four different ink formulations are screen printed on top of a flexible substrate. **(1)** The schematic shows the design of the silver pattern. **(2)** The pattern of the insulating layer is shown. **(3)** The pattern of the adhesive layer is shown, where each circle will be located at the periphery of the respective sensor cavity after the lamination process. **(4)** The schematic shows the tactile pillars, note that these are screen printed on the other side of the substrate.

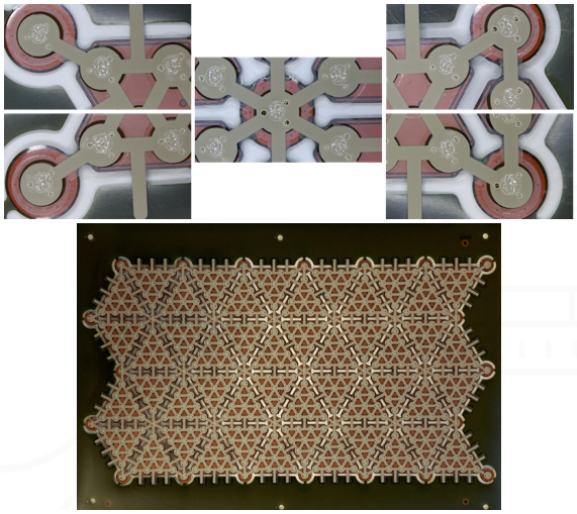

Figure 3.7 The *upper images* show the alignment accuracy after laminating the printed electronic skin onto the CySkin module sheet (corner and middle taxels). The *lower image* shows one full sheet (23×12 cm^2) after lamination

This manufacturing strategy enables the realization of large-area tactile skins with improved repeatability and reduced assembly complexity compared to the original CySkin solution.

By shifting the sensing interface to a printed and laminated layer, CySkin+ decouples the mechanical sensing structure from the electronics, providing greater flexibility in material selection and enabling systematic optimization of sensitivity, robustness, and integration.

3.4 CySkin and CySkin+ Experimental Characterization and Comparison

This section presents the experimental characterization of CySkin and CySkin+ tactile patches, with the objective of evaluating their sensing performance under controlled mechanical loading conditions and enabling a direct comparison between the two architectures. While CySkin represents the reference platform for modular tactile sensing, CySkin+ introduces material and structural modifications aimed at improving scalability, manufacturability, and integration with printed electronics.
The experimental activity focuses on the characterization of individual taxels and patches, including sensitivity, repeatability, hysteresis, and spatial response. Particular attention is given to the characterization of CySkin+ modules, whose experimental results are later compared with those obtained on CySkin and with the FEM-based predictions discussed in Section 3.2. This approach allows assessing the impact of substrate replacement and manufacturing choices on the overall tactile sensing performance.

3.4.1 Experimental Setup for CySkin+ Characterization

The experimental setup adopted for the characterization of CySkin+ patches was designed to apply controlled and repeatable normal forces on individual taxels, while simultaneously measuring the corresponding capacitive response. The setup follows was specifically adapted to the mechanical and electrical characteristics of the laminated CySkin+ modules.
Each sensor patch was placed on a rigid support and mechanically constrained to avoid sliding or bending during the tests. Force application was performed using a motorized positioning system (Thorlabs BSC103 *Thorlabs (2024)*) based on three linear translation stages,shown in Fig. 3.8, providing independent motion along the X, Y, and Z axes. Two stages were used to accurately align the selected taxel under the indenter, while the vertical stage controlled the normal displacement applied to the sensor surface.

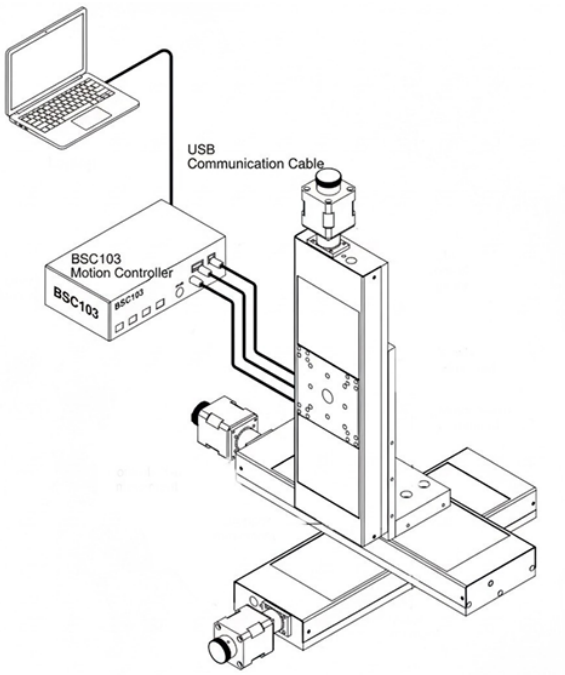

Figure 3.8 Experimental positioning hardware. The BSC103 controller was used to operate three NRT150/M stages, enabling precise X, Y and Z positioning of the indenter

Normal forces were applied using a custom-designed indenter equipped with a circular metal tip of 4 mm diameter. This dimension was selected to match approximately the size of a single CySkin taxel, ensuring that the applied load was localized and minimizing mechanical coupling with neighboring taxels. The indenter was rigidly connected to a load cell, allowing direct measurement of the applied force during each test.
Force measurements were acquired using a 6 kg strain-gauge load cell, interfaced through a 24-bit HX711 analog-to-digital converter. The load cell signal was continuously monitored and logged, providing a precise reference for the applied force throughout the experiments. Prior to each measurement sequence, a calibration procedure was performed to associate the indenter displacement with the corresponding applied force, compensating for small variations due to material compliance and mounting tolerances.Fig. 3.9 shows the configuration of the load cell measurement. Since the output is in $[kg]$ to extract the force in $[N]$ we derived it from the weight force equation:

$$F_p\,[N] \;=\; m\,[kg] \;\cdot\; g\,[m/s^2] \tag{3.1}$$

where g is the gravitational acceleration $g \;=\; 9.81\; m/s^2$.

And knowing the area of the indenter that applies the pressure, it is also possible to compute the pressure applied:

$$P\,[kPa] = \frac{F\,[N]}{A\,[mm^2]} \cdot 10^{-3} \tag{3.2}$$

where A is the area of a circle than $A = r^2 \cdot \pi$

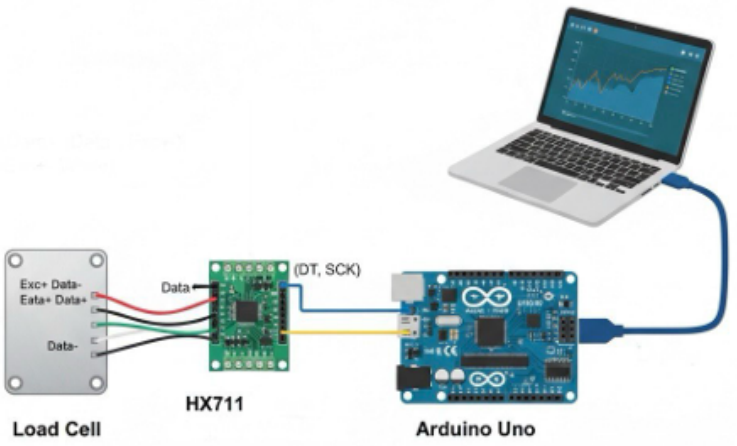

Figure 3.9 Configuration for a load cell measurement system, detailing the signal path from the load cell through an HX711 module to an Arduino Uno, and finally to a laptop for real-time data monitoring.

Capacitive data from the CySkin+ patches were acquired through the standard CySkin electronic architecture, consisting of local capacitance-to-digital converters and microcontrollers embedded on each patch. The sensor data were transmitted to the host computer through the the Intelligent Hub Board (IHB) depicted in Fig. 3.10 and then recorded together with force measurements using synchronized timestamps, enabling accurate correlation between applied load and sensor response during post-processing. Fig. 3.10 illustrates the standard architecture used for data acquisition from CySkin. the improvement of this data acquisition system is part of the chapter and it will be discussed in the next section.

The experimental setup showed in Fig. 3.11 allowed both single-step loading tests and cyclic loading–unloading sequences to be executed in a controlled and repeatable manner. This configuration provided the basis for the sensitivity, repeatability, hysteresis, and spatial resolution analyses presented in the following sections.

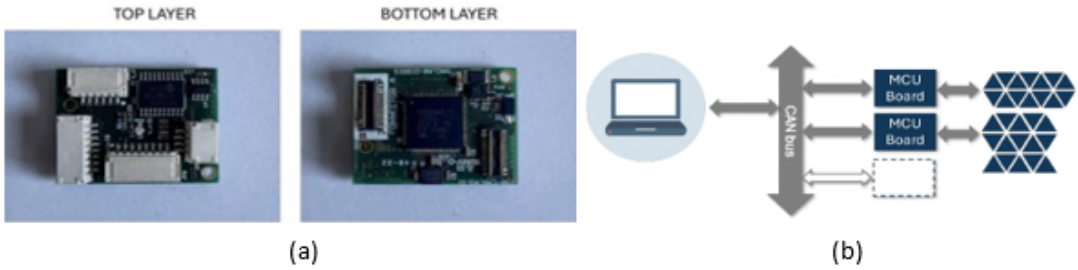

Figure 3.10 (a) IHB module top and bottom layer. **(b)** CAN Communication protocol of CySkin then substituted by the EtherCAT bus developed by *Giovinazzo et al. (2024b)*

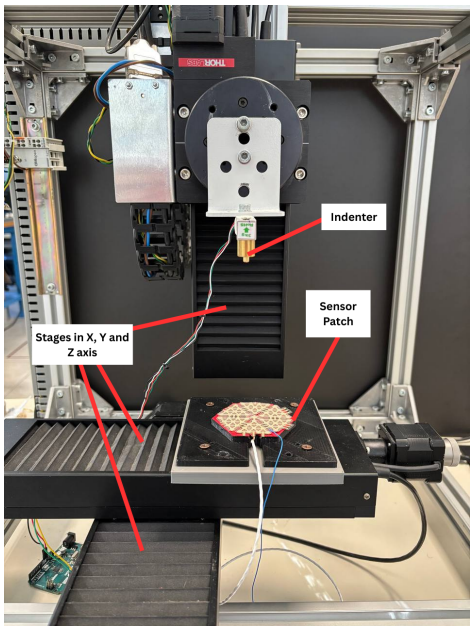

Figure 3.11 Complete overview of the custom-made experimental setup.

3.4.2 Measurement Protocols and Tested Samples

The experimental characterization of CySkin and CySkin+ was conducted following measurement protocols designed to ensure repeatability and direct comparison across different sensor architectures and substrate configurations as stated in the state of the art like in *Maiolino et al. (2013)* and in *Dahiya et al. (2010)*. The protocols include step-wise and cyclical tests to extract the metrics of *Noise*, *Limit of Detection (LoD)*, *Sensitivity*, *Repeatability*, *Hysteresis* and *Spatial resolution*.

The characterization focused on individual taxels, selected from different regions of each sensor patch in order to account for fabrication-related variability. For CySkin, reference

measurements were performed on taxels fabricated on Lycra-based substrates. For CySkin+, taxels fabricated on polymer-based substrates were considered, including PET, TPU, and Kapton configurations, as introduced in Section 3.2. In particular Fig. 3.12 shows the fabricated CySkin and CySkin+ hexagon samples used in the tests: Lycra (Cyskin), PET 50 μm, PET 125 μm, Kapton 50 μm and TPU 100 μm.
Each sensor sample was mechanically constrained on a rigid support and tested under controlled normal loading conditions using the experimental setup described in Section 3.4.1. Force and capacitance data were synchronized and recorded for offline processing, enabling a consistent comparison between different samples and substrate solutions.

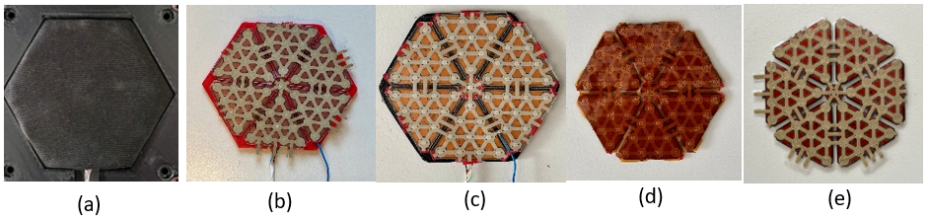

Figure 3.12 (a) CySkin sample **(b)** CySkin+ with PET 50 μm **(c)** CySkin+ with PET 125 μm **(d)** CySkin+ with Kapton 50 μm **(e)** CySkin+ with TPU 100 μm.

3.4.3 Noise and Limit of Detection

Noise and limit of detection (LoD) are key parameters that define the reliability of a tactile sensor. Noise originates from material properties, electronic circuitry, and environmental factors, and directly affects the stability of the sensor output. A lower noise level results in more stable readings and reduces the likelihood of false detections. The limit of detection, on the other hand, defines the smallest measurable input force that the sensor can reliably distinguish from noise. Together, these parameters determine the sensor's capability to detect weak stimuli, which is particularly relevant for applications requiring sensitivity to subtle contact forces.
To measure the noise level, each sensor patch was placed in the experimental setup without applying any external force, and the sensor output was recorded for a duration of two minutes. During this time interval, the capacitance signal was continuously acquired for each taxel. The noise level was then calculated as the difference between the maximum and minimum values measured during the acquisition period.

$$Noise_{\text{digits}} = Y_{\text{MAX}} - Y_{\text{min}} \tag{3.3}$$

To determine the limit of detection, small incremental forces were gradually applied to the sensor surface until a measurable output variation exceeding the noise level was observed. The smallest applied force that consistently generated a response larger than the noise was identified as the limit of detection. The results reported in this section focus on the experimental measurements, while a broader discussion of their implications is provided in Chapter 6.

Table 3.4 summarizes the measured noise levels, the corresponding limits of detection expressed in digital units, and the equivalent applied force for the different CySkin and CySkin+ sensor configurations.

Sensor Type	**Noise [Digits]**	**LoD [Digits]**	**Force [N]**	**Pressure [kPa]**
CySkin	4	147	0.01	0.80
CySkin+ (TPU100 μm)	11	104	0.011	0.88
CySkin+ (Kapton50 μm)	61	303	0.035	2.79
CySkin+ (PET50 μm)	38	173	0.041	3.26
CySkin+ (PET125 μm)	12	144	0.05	3.98

Table 3.4 Noise level, limit of detection (LoD) and its corresponding force and pressure for different CySkin and CySkin+ sensor configurations.

3.4.4 Sensitivity

Sensitivity is a key performance metric for tactile sensors, as it quantifies the change in sensor output with respect to the applied mechanical stimulus. In this work, sensitivity is defined as the slope of the capacitance–pressure curve within the linear operating region, consistently with the definitions adopted in Chapters 2 and 3 and in the related literature *Dahiya et al. (2010); Maiolino et al. (2013).*

$$S = \frac{\Delta C}{\Delta P} \; or \; S = \frac{\Delta C}{\Delta F} \tag{3.4}$$

For both CySkin and CySkin+ configurations, sensitivity was extracted from loading tests performed using the experimental setup described in Section 3.4.1. A force ranging from 0 to 15 *N* was applied for 3 times on the middle taxel of a triangular configuration, waiting a 10 *min* rest period between each experiment to avoid hysteresis effects. The applied force measured by the load cell was converted into pressure by dividing by the effective taxel area according to Eq. 3.1 and Eq. 3.2, and the corresponding capacitance variation was recorded for each tested taxel expressed in Digits and $[fF]$ following the conversion adopted by the

quantization step defined by the acquisition electronics:

$$1\ digit\ =\ \frac{20\ pF}{2^{16}\ -\ 1}\ \approx 0.3\ fF \tag{3.5}$$

The sensitivity was computed by fitting a linear model to the initial portion of the pressure–capacitance response, where the sensor exhibits a stable and repeatable behavior. This region corresponds to low and moderate pressure levels, where the mechanical structure has not yet reached significant stiffening effects.

Figure 3.13 reports representative pressure–capacitance curves for CySkin and CySkin+ samples fabricated on different substrates, then summarized in Tab. 3.5 A clear increase in sensitivity is observed when transitioning from the original Lycra-based CySkin to CySkin+ configurations based on polymer substrates. In particular, substrates with lower elastic modulus, such as TPU, exhibit higher sensitivity due to the larger deformation induced under the same applied pressure. Conversely, stiffer substrates such as PET and Kapton provide lower sensitivity but improved mechanical stability.

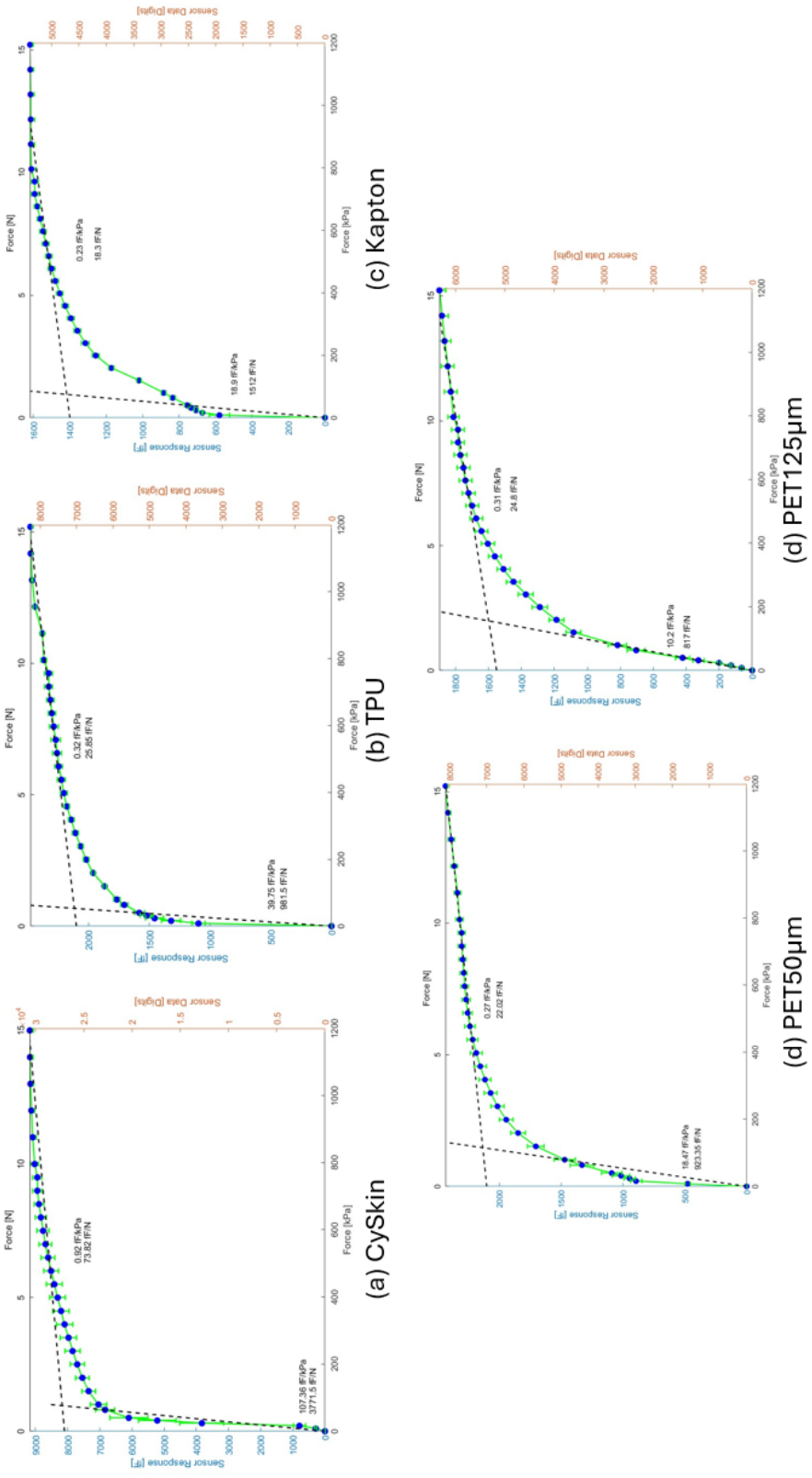

Figure 3.13 **(a)** CySkin sensitivity response **(b)** CySkin+ with TPU 100 μm sensitivity response **(c)** CySkin+ with Kapton 50 μm sensitivity response **(d)** CySkin+ with PET 50 μm sensitivity response **(e)** CySkin+ with PET 125 μm sensitivity response.

Sensor Type	**Sensitivity [fF/kPa]**	**Sensitivity [fF/N]**
CySkin	107.36	3771.5
CySkin+ (TPU 100 μm)	39.75	981.5
CySkin+ (Kapton 50 μm)	18.9	151.2
CySkin+ (PET 50 μm)	18.47	923.3
CySkin+ (PET 125 μm)	10.2	817.0

Table 3.5 Sensitivity values extracted from the initial linear region of the pressure–capacitance response for CySkin and CySkin+ samples, expressed both in terms of pressure and applied force.

The experimental sensitivity values follow the same qualitative trends predicted by the FEM analysis presented in Section 3.2. In particular, thinner PET substrates and more compliant materials yield higher sensitivity, confirming the strong influence of substrate mechanical properties on the transduction mechanism. However, these results show that the original CySkin architecture exhibits the highest sensitivity among all tested configurations. This result is expected, given the significantly lower stiffness of the Lycra-based structure compared to any of the polymer substrates adopted in CySkin+.
The advantage of CySkin+ should therefore not be interpreted in terms of raw sensitivity, but rather as a controlled design trade-off. By replacing the Lycra layer with printable polymer substrates, CySkin+ gains improved fabrication repeatability, mechanical robustness, and compatibility with scalable manufacturing processes, at the cost of a reduction in initial sensitivity. These complementary performance aspects, including repeatability, hysteresis, and spatial resolution, are analyzed in the following sections and summarized in Section 3.4.7. The results confirm that sensitivity can be effectively tuned through substrate selection without modifying the sensing geometry, enabling application-specific optimization within the CySkin+ design choices.

3.4.5 Repeatability and Hysteresis

Repeatability and hysteresis are fundamental metrics for evaluating the stability and reliability of tactile sensors under repeated mechanical loading. Repeatability describes the ability of the sensor to provide consistent outputs when the same stimulus is applied multiple times, while hysteresis quantifies the difference in sensor response between loading and unloading phases for the same applied force.
To assess repeatability and hysteresis, cyclic loading tests were performed following the same mechanical configuration adopted for the sensitivity measurements described in Section 3.4.4.

Each hexagonal CySkin or CySkin+ patch was positioned on the experimental setup such that the indenter applied force to the central taxel of a triangular configuration. A cyclic force ranging from 0 to 5 N (400 kPa) was applied and subsequently released back to the no-contact condition. This loading–unloading sequence was repeated for 30 consecutive cycles, with a maximum rest time of 60 s in between cycles.

During the experiments, force and capacitance signals were recorded continuously. The sensor response was then plotted as a function of time to visualize the cyclic behavior. For each cycle, the maximum output value reached by the sensor was extracted.

Repeatability was quantified by computing the standard deviation of these maximum values across all cycles, normalized with respect to their mean value. In percentage form, repeatability was calculated as:

$$R = \sigma_Y \times 100\% \tag{3.6}$$

where σ_Y is the standard deviation of the maximum sensor output values across cycles. Lower repeatability values indicate a more stable and consistent sensor response under repeated loading. Fig. 3.14 shows the repeatability graphs of each sample.

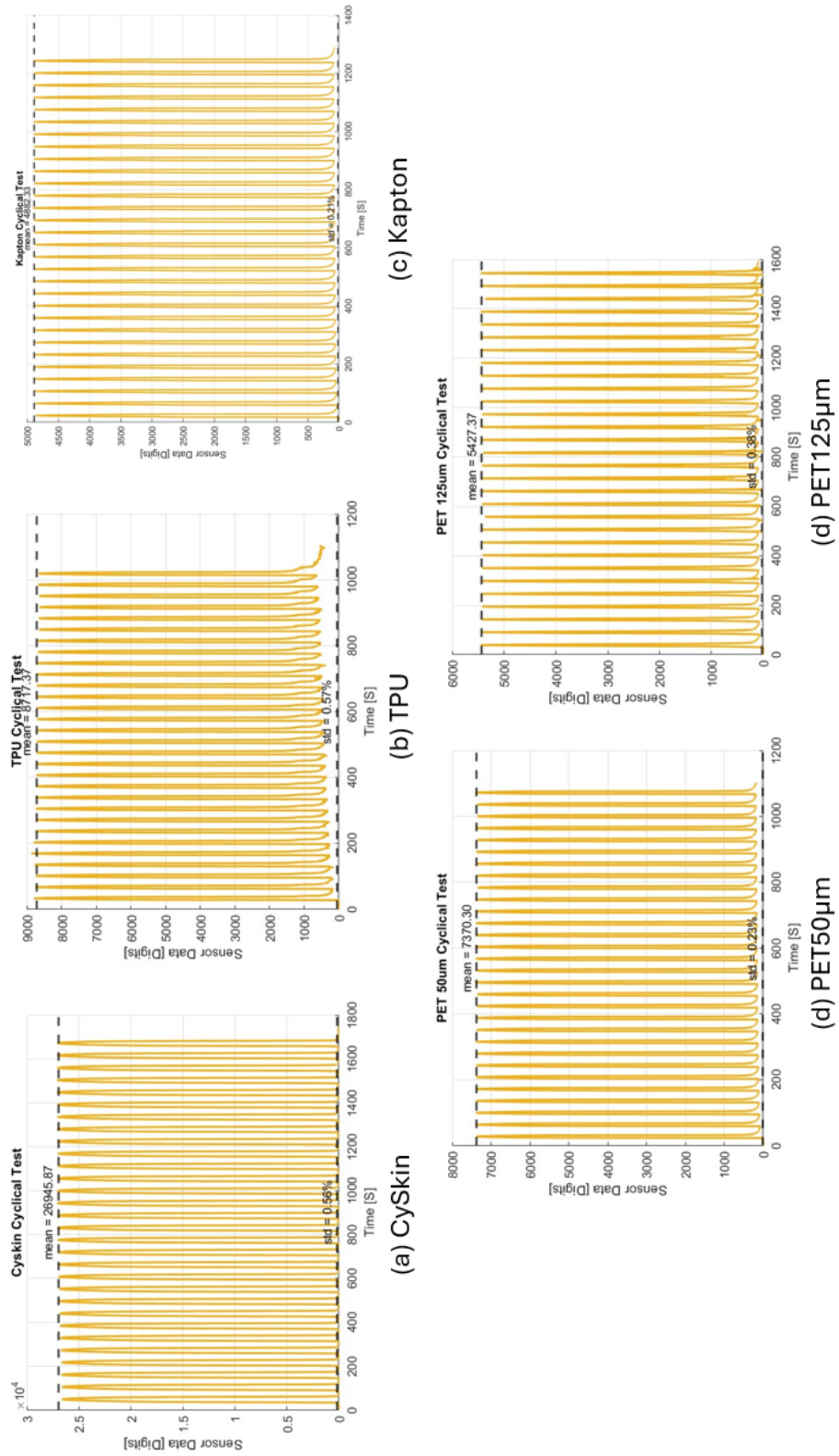

Figure 3.14 **(a)** CySkin repeatability response **(b)** CySkin+ with TPU 100 μm repeatability response **(c)** CySkin+ with Kapton 50 μm repeatability response **(d)** CySkin+ with PET 50 μm repeatability response **(e)** CySkin+ with PET 125 μm repeatability response.

To evaluate hysteresis, force and sensor output signals were synchronized through interpolation in order to ensure an accurate correspondence between applied force and measured capacitance. The sensor output was then compared at identical force levels during the loading (increasing force) and unloading (decreasing force) phases of each cycle. This approach allows a direct assessment of the dependence of the sensor output on the loading direction. Fig. 3.15 illustrates the hysteresis graphs of each sample.

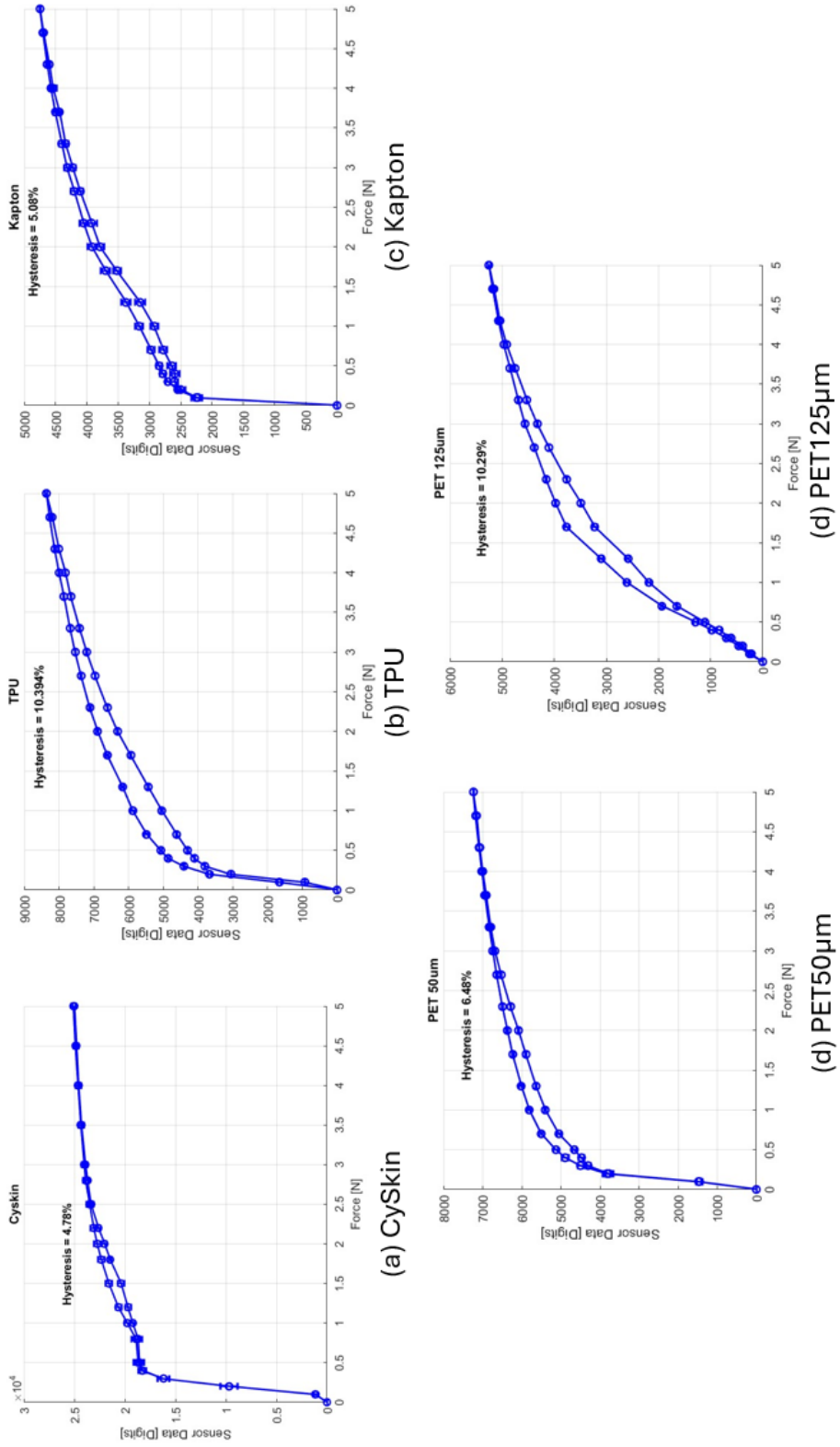

Figure 3.15 **(a)** CySkin hysteresis response **(b)** CySkin+ with TPU 100 μm hysteresis response **(c)** CySkin+ with Kapton 50 μm hysteresis response **(d)** CySkin+ with PET 50 μm hysteresis response **(e)** CySkin+ with PET 125 μm hysteresis response.

Hysteresis error was computed using a widely adopted definition, expressed as the maximum absolute difference between the loading and unloading curves, normalized by the full-scale output (FSO):

$$H = \frac{\max \left| Y_{\text{loading}}(F) - Y_{\text{unloading}}(F) \right|}{Y_{\text{FSO}}} \times 100\% \tag{3.7}$$

where $Y_{\text{loading}}(F)$ and $Y_{\text{unloading}}(F)$ are the sensor outputs at the same applied force during loading and unloading, respectively, and Y_{FSO} is the maximum sensor output within the considered force range.

These metrics provide complementary information on the dynamic behavior of CySkin and CySkin+ sensors. Repeatability reflects the stability of the sensing system over time, while hysteresis highlights the influence of viscoelastic effects and mechanical energy dissipation within the sensor structure. These experimental results obtained for different substrate materials are summarized in Tab. 3.6 and Tab. 3.7.

Sensor Type	**Repeatability [%]**
CySkin	0.56
CySkin+ (TPU 100 μm)	0.57
CySkin+ (Kapton 50 μm)	0.21
CySkin+ (PET 50 μm)	0.23
CySkin+ (PET 125 μm)	0.38

Table 3.6 Repeatability of CySkin and CySkin+ sensors evaluated as the normalized standard deviation of the maximum sensor response over repeated loading cycles.

Sensor Type	**Hysteresis [%]**
CySkin	4.78
CySkin+ (TPU 100 μm)	10.39
CySkin+ (Kapton 50 μm)	5.08
CySkin+ (PET 50 μm)	6.48
CySkin+ (PET 125 μm)	10.29

Table 3.7 Hysteresis error of CySkin and CySkin+ sensors calculated as the maximum difference between loading and unloading curves, normalized by the full-scale output (FSO).

3.4.6 Spatial Resolution

Spatial resolution defines the ability of a tactile sensing system to localize a contact and to discriminate between stimuli applied at neighboring positions on the sensing surface. For

modular tactile skins such as CySkin and CySkin+, spatial resolution is primarily determined by the taxel geometry, spacing, and mechanical coupling between adjacent sensing elements. A high spatial resolution is essential for accurately detecting contact location, pressure distribution, and interaction patterns on robotic surfaces.

The spatial resolution of CySkin and CySkin+ patches was evaluated by applying localized normal forces at different positions across the sensing surface while monitoring the response of multiple neighboring taxels. The experimental setup described in Section 3.4.1 was used, with the indenter positioned at controlled locations relative to the taxel layout.

During the test, a constant normal force was applied sequentially at predefined positions, starting from the center of a reference taxel and progressively shifting toward adjacent taxels. Fig. 3.16 highlights the activated taxels during the experiment. For each indenter position, the capacitance variation of the central taxel and its neighboring elements was recorded. This procedure allows the assessment of mechanical cross-talk and the effective spatial spreading of the applied stimulus.

The spatial response was quantified by analyzing the relative amplitude of the sensor output as a function of the distance between the indenter position and the center of a reference taxel.

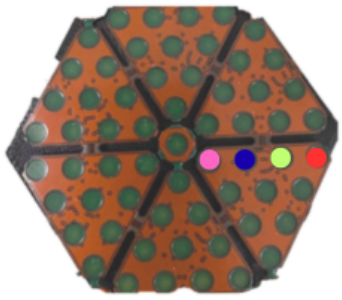

Figure 3.16 Hexagonal sensor patch showing the taxels activated during the experiment, indicated by color coding.

Spatial resolution was defined as the minimum distance at which the response of the directly stimulated taxel could be clearly distinguished from the responses of adjacent taxels, indicating a localized and spatially confined activation.

As shown in Fig. 3.17, the spatial resolution measurements highlight a clear difference between CySkin and CySkin+ architectures. All CySkin+ patches exhibit well-localized responses, characterized by a significant response of the taxel directly under the indenter and inactive or low-response regions between neighboring taxels. This behavior indicates limited mechanical coupling and reduced cross-talk between adjacent sensing elements.

In contrast, the original CySkin patch shows partially overlapping responses between neighboring taxels, with multiple taxels having measurable outputs even when the applied force is not directly centered on them. This effect can be interpreted in two complementary ways. On one hand, it reflects the presence of mechanical cross-talk, where non-targeted taxels are activated due to substrate compliance. On the other hand, such overlapping responses may be advantageous for applications involving contact pattern recognition, as forces applied between two taxels still generate measurable signals that can improve the reconstruction of pressure distributions.

Overall, these results confirm that CySkin+ not only preserves but improves the spatial localization capabilities of the original CySkin architecture. At the same time, substrate selection enables a controlled trade-off between sensitivity and spatial resolution, in agreement with the FEM analysis and the experimental trends discussed in the previous sections. This balance represents a key design consideration for large-area robotic skin applications.

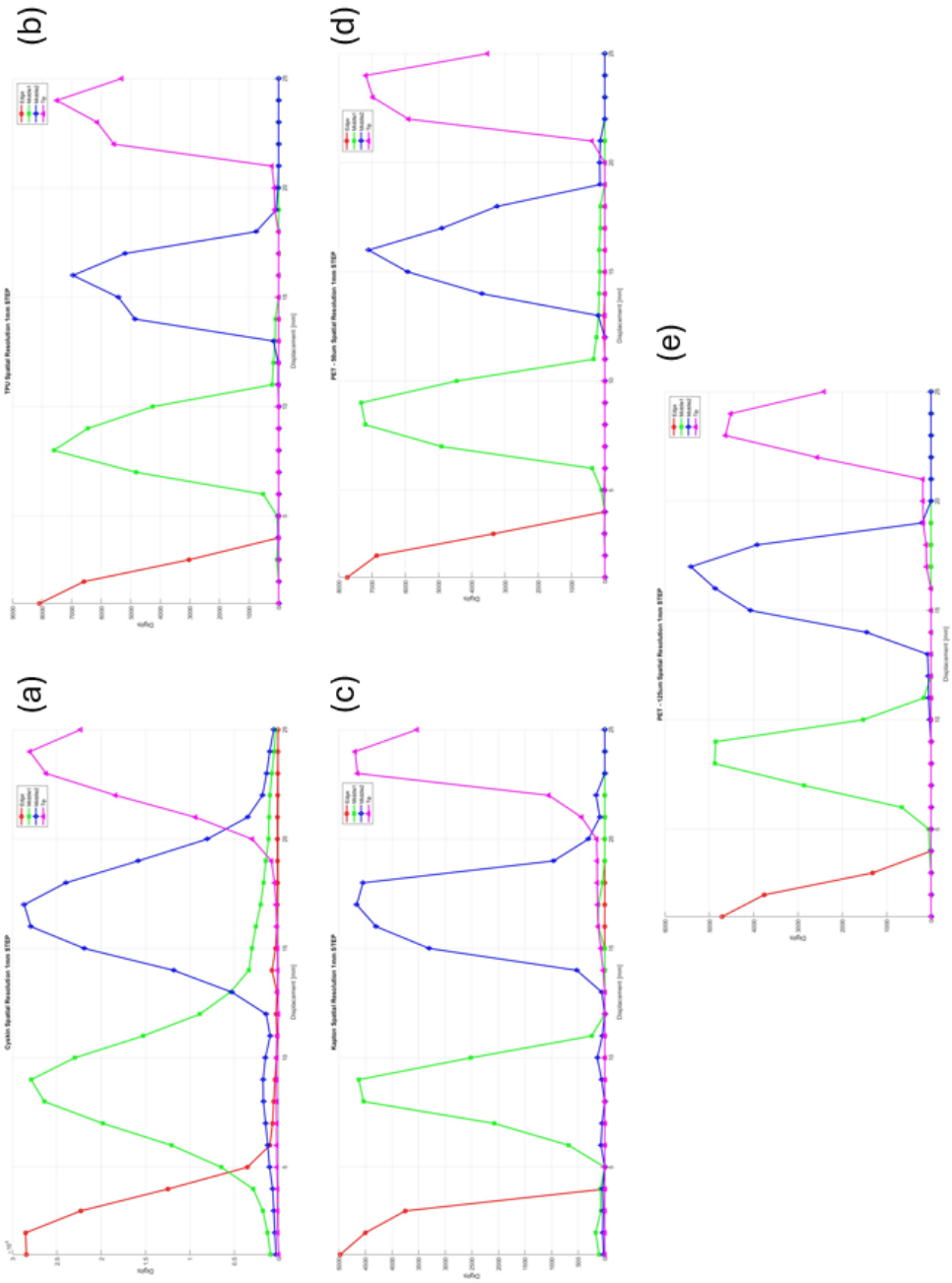

Figure 3.17 **(a)** CySkin spatial resolution graph **(b)** CySkin+ with TPU 100 μm spatial resolution graph **(c)** CySkin+ with Kapton 50 μm spatial resolution graph **(d)** CySkin+ with PET 50 μm spatial resolution graph **(e)** CySkin+ with PET 125 μm spatial resolution graph.

3.4.7 Summary of Performance Trade-offs

The experimental characterization presented in Sections 3.4.3–3.4.6 highlights how the transition from the original CySkin architecture to CySkin+ enables a systematic tuning of sensor performance through substrate selection. While all configurations rely on the same capacitive sensing principle and taxel geometry, the mechanical properties of the substrate play a dominant role in determining sensitivity, noise level, repeatability, hysteresis, and spatial resolution.

The original CySkin patch based on conductive Lycra exhibits the highest sensitivity and excellent tactile responsiveness, but at the cost of limited reproducibility, higher mechanical coupling between taxels, and more complex integration on robotic structures. In contrast, CySkin+ patches fabricated on polymer substrates show improved fabrication repeatability, better spatial localization, and enhanced robustness, at the expense of a reduced sensitivity that depends on substrate stiffness.

Stiffer substrates such as Kapton and thin PET films provide low hysteresis, high repeatability, and well-confined spatial responses, making them suitable for applications where signal stability and localization are critical. Softer substrates such as TPU offer higher sensitivity and easier lamination, but introduce increased hysteresis and reduced spatial resolution due to larger in-plane deformation.

Table 3.8 summarizes the main strengths and limitations of the analyzed CySkin and CySkin+ configurations, providing a concise overview of the trade-offs involved in substrate selection. These results confirm that CySkin+ enables a flexible design space in which sensor performance can be tailored to application-specific requirements, representing a key step toward scalable and robust large-area robotic skin systems.

Material	**Strengths**	**Limitations**
CySkin (Lycra)	Highest sensitivity and excellent tactile response.	Difficult integration and limited reproducibility due to the soft, fabric-based structure.
Kapton (50 μm)	Excellent repeatability, low hysteresis, and good spatial resolution.	Lower sensitivity compared to softer substrates.
PET (50 μm)	Good balance between flexibility and mechanical stability; easy fabrication, low hysteresis, and low cost.	Lower sensitivity than highly compliant materials.
PET (125 μm)	Mechanically stable, durable, and low cost.	Lowest sensitivity and increased hysteresis due to higher stiffness.
TPU (100 μm)	Highly flexible, easy to laminate, and overall balanced performance.	Moderate hysteresis and reduced spatial resolution due to higher compliance.

Table 3.8 Summary of strengths and limitations for the analyzed CySkin and CySkin+ tactile sensor configurations, highlighting the main trade-offs associated with substrate selection.

3.5 EtherCAT-based Communication Architecture

The progressive evolution from single tactile patches to large-area tactile skins, as discussed for CySkin and CySkin+, introduces communication and data acquisition challenges that cannot be efficiently addressed using centralized or low-bandwidth architectures. As the number of taxels and sensing modalities increases, the tactile system transitions from a local sensing device to a distributed real-time sensing network, where scalability, determinism, and synchronization become primary design constraints, as widely reported in the literature on robotic skins *(Dahiya et al. (2010); Kappassov et al. (2015))*.

Early CySkin implementations relied on a Controller Area Network (CAN) bus to collect sensor data from distributed tactile patches. While this solution provided robustness and simplicity for small-scale systems, its limitations in terms of bandwidth and polling-based acquisition became evident when extending tactile coverage to larger robot surfaces. In particular, the achievable sampling rate decreases rapidly as the number of connected nodes increases, directly impacting real-time interaction performance.

These limitations motivated the investigation of alternative communication architectures capable of supporting distributed, high-throughput, and time-deterministic data exchange. EtherCAT (Ethernet for Control Automation Technology) was selected as the communication backbone for next-generation tactile skins due to its widespread adoption in industrial real-time systems and its capability to support large numbers of distributed nodes with precise synchronization through distributed clocks *(EtherCAT Technology Group (2023))*.

The adoption of EtherCAT in the context of CySkin and ProxySKIN is not driven by a generic preference for industrial fieldbuses, but rather by concrete system-level requirements arising from tactile skin scalability. As highlighted in recent works on distributed multimodal sensing systems *Giovinazzo et al. (2024b)*, EtherCAT provides a unified framework for integrating heterogeneous sensor nodes—including capacitive tactile sensors, proximity sensors, and inertial units—within a single deterministic network. This capability is particularly relevant for robotic skins, where tactile data must be synchronized with other sensory streams and control loops.

In the following, the design principles, implementation details, and experimental validation of the EtherCAT-based distributed architecture adopted for CySkin and ProxySKIN are presented.

3.5.1 System Requirements and Design Constraints

The design of a communication architecture for large-area tactile skins must address a set of strict system-level requirements that rise as the number of sensing elements increases. Unlike localized tactile sensors, robotic skins involve hundreds or thousands of taxels distributed over extended surfaces, each generating continuous data streams that must be acquired, synchronized, and transmitted in real time.

One of the first requirements is *Scalability*. The communication system must support a growing number of sensor nodes without a proportional degradation of sampling rate or latency. In polling-based architectures such as CAN, the effective bandwidth per node decreases as new devices are added to the network, limiting the achievable update rate for tactile feedback. This behavior is incompatible with large-area tactile skins, where high spatial resolution must be preserved without sacrificing temporal resolution.

A second fundamental requirement is *Determinism*. Tactile sensing is often used within closed-loop control schemes for safe human–robot interaction, collision detection, and compliant manipulation. In these scenarios, bounded and predictable communication latency is essential to ensure stable and safe control behavior. Best-effort or non-deterministic communication protocols introduce timing uncertainties that can compromise system reliability when tactile feedback is integrated into fast control loops.

Closely related to determinism is the requirement for *Time Synchronization*. In distributed tactile skins, sensor data acquired from different patches must be temporally aligned in order to reconstruct coherent pressure maps and to correlate tactile information with other sensing modalities, such as proximity or inertial measurements. The lack of a global time reference leads to spatial and temporal inconsistencies, especially when tactile events occur at multiple locations simultaneously. *Delgado et al. (2016)* verify the timing accuracy of an EtherCAT-based real-time motion control system to actuate a differential drive mobile robot. Fig. 3.18 shows the system and the timing analysis.

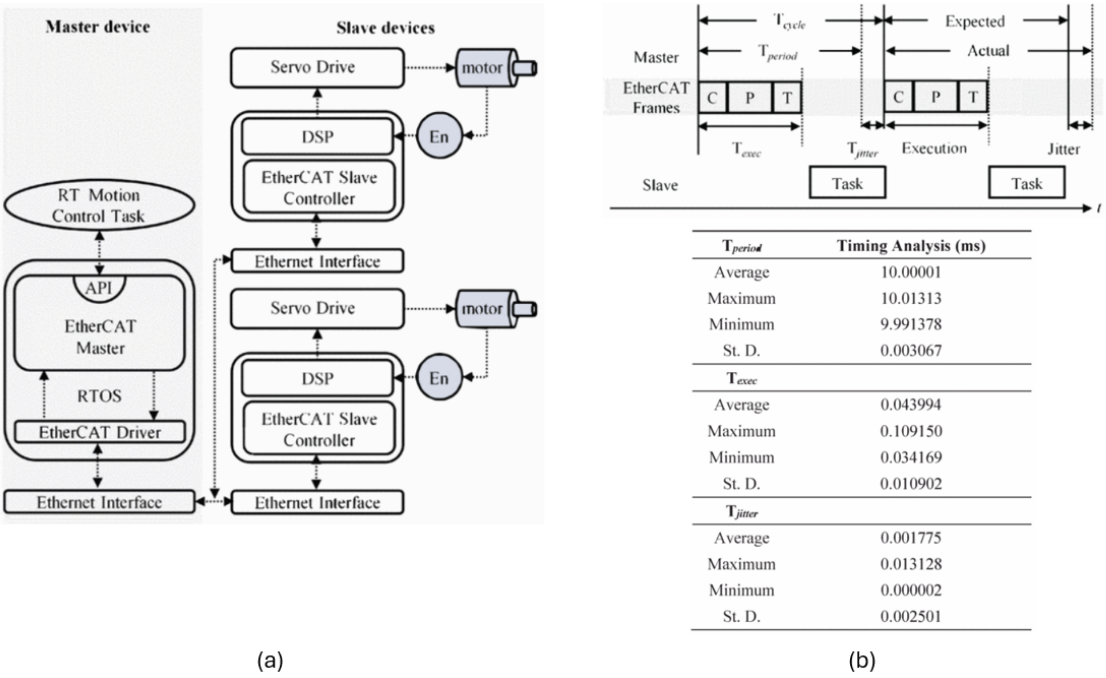

T_{period}	Timing Analysis (ms)
Average	10.00001
Maximum	10.01313
Minimum	9.991378
St. D.	0.003067
T_{exec}	
Average	0.043994
Maximum	0.109150
Minimum	0.034169
St. D.	0.010902
T_{jitter}	
Average	0.001775
Maximum	0.013128
Minimum	0.000002
St. D.	0.002501

(a) (b)

Figure 3.18 *Delgado et al. (2016)* **(a)** System structure of a motion control system for a mobile robot **(b)** Timing diagram and timing analysis of the EtherCAT-based control system.

In addition to performance constraints, *Modularity* and *Heterogeneity* represent key design requirements. The communication architecture must support the integration of different types of sensing nodes, potentially featuring heterogeneous sampling rates, data formats, and processing capabilities. *Wang et al. (2011)* present and evaluate the performance of an EtherCAT-based communication network for interconnecting servo motors and a large number of sensors in real-time motion control system. Fig. 3.19 illustrates the architecture system.

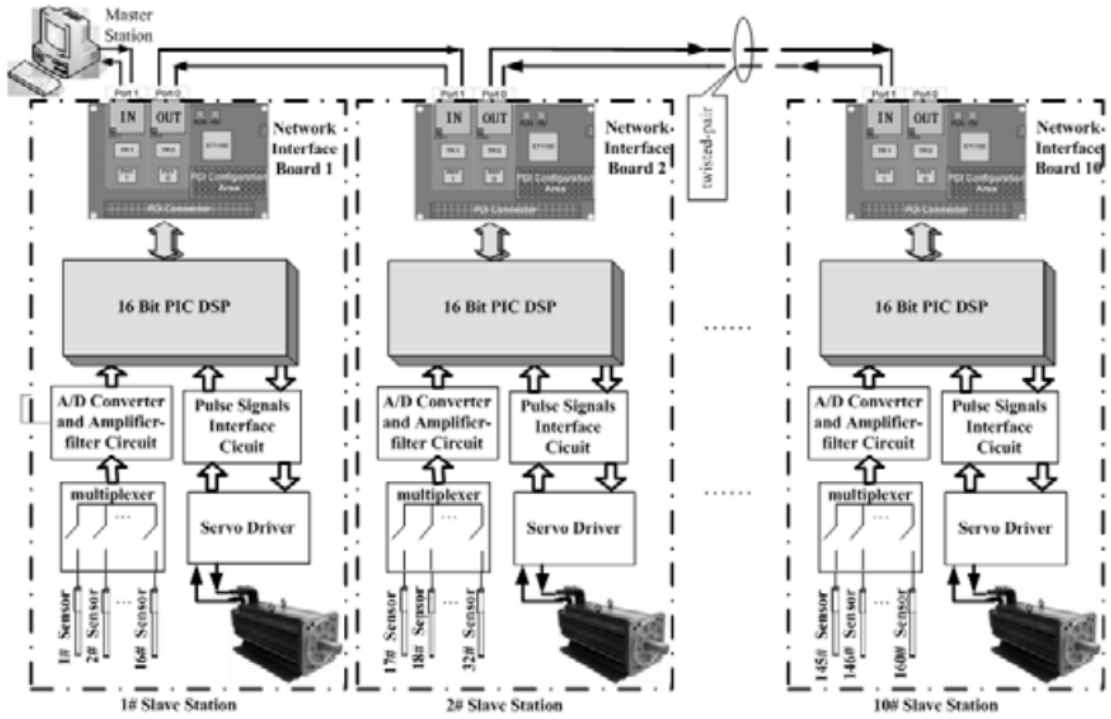

Figure 3.19 *Wang et al. (2011)* Structure of networked wave maker control modules.

Finally, the communication system must be compatible with embedded hardware constraints. Local processing nodes embedded within tactile patches are typically limited in terms of computational resources, memory, and power consumption. The selected protocol must therefore provide an efficient data transfer mechanism with minimal overhead, while remaining compatible with low-power microcontrollers used at the sensor level.
These requirements lead to a real-time EtherCAT-based solution. In the following sections, EtherCAT is presented as the communication technology selected to satisfy these constraints, and its integration within the CySkin and ProxySKIN architectures is discussed in detail.

3.5.2 EtherCAT Principles and Suitability for Distributed Tactile Skins

EtherCAT (Ethernet for Control Automation Technology) is a real-time Ethernet-based fieldbus specifically designed to support deterministic and high-throughput communication in distributed control systems, standardized in IEC 61158 with 100 Mbps data rate. Its operating principles directly address the requirements identified in Section 3.5.1, making it well suited for large-area tactile skins composed of many distributed sensing nodes.
A key feature of EtherCAT is the *On-The-Fly* frame processing mechanism. Unlike con-

ventional Ethernet-based protocols, EtherCAT frames are not fully received and buffered at each slave node. Instead, each slave reads and writes its process data while the frame passes through the device hardware, introducing only a minimal and predictable delay. This approach allows a single Ethernet frame to collect data from multiple distributed nodes within one communication cycle, significantly improving bandwidth utilization and reducing latency. The mechanism is represented in Fig. 3.20.

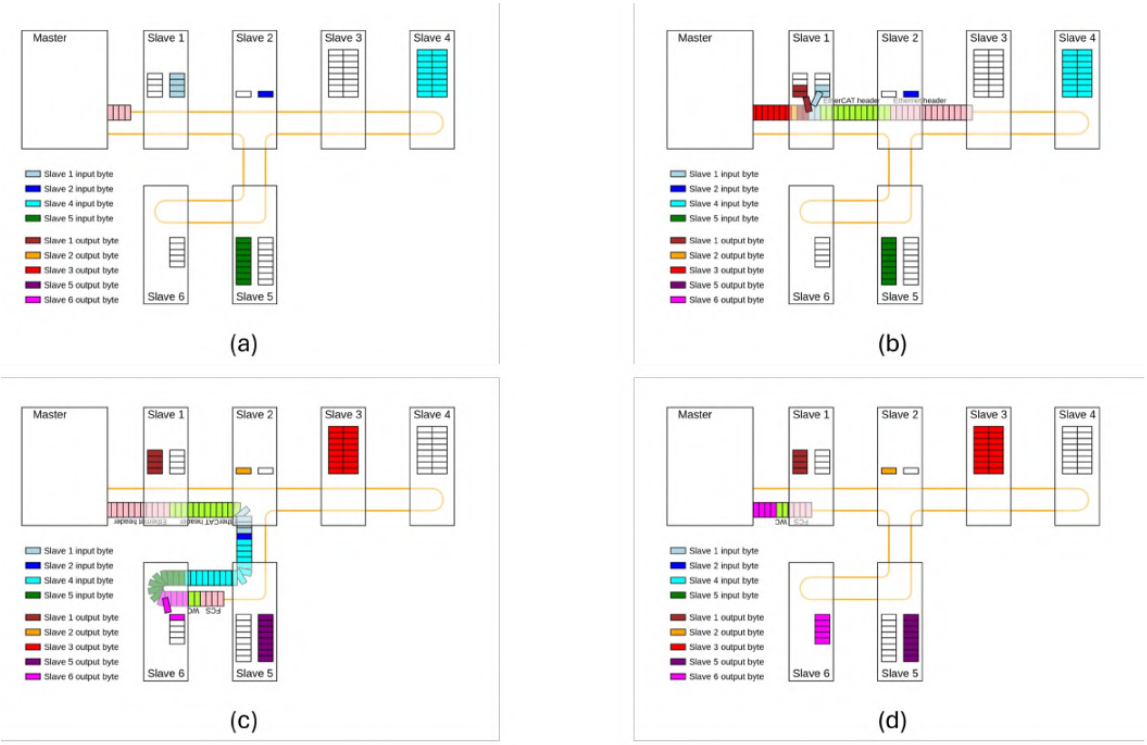

Figure 3.20 Schematic representation of the EtherCAT "processing on the fly" working principle. **(a)** The datagram leaves the master; **(b)** As the message passes through the first slave, input and output bytes are exchanged. **(c)** the same mechanism is repeated for each slave in the network. **(d)** The datagram, returns to the master node with the updated slaves input data.

Another fundamental aspect of EtherCAT is the use of *Distributed Clocks*. Each slave node maintains a local clock that is synchronized with sub-microsecond accuracy to a global reference clock managed by the master. This hardware-level synchronization enables precise temporal alignment of data acquired from different nodes, which is essential for reconstructing coherent tactile maps across large robotic surfaces and for correlating tactile data with other sensor modalities.

From a network topology perspective, EtherCAT supports flexible configurations, including line, tree, and ring topologies, without requiring additional switches. This flexibility is particularly advantageous for robotic skins, where sensor patches must conform to complex geometries and where routing constraints often dictate non-regular network layouts. The ability to connect nodes in a line topology also simplifies wiring and reduces the overall system complexity.
In addition to its real-time performance, EtherCAT provides efficient support for heterogeneous devices within the same network. Sensor nodes with different data rates and processing capabilities can coexist and exchange data in a unified communication cycle. This characteristic aligns with the requirements of CySkin and ProxySKIN architectures, where capacitive tactile sensors and proximity sensors are integrated within a single distributed sensing framework *Giovinazzo et al. (2024b)*.
Finally, EtherCAT is compatible with embedded implementations based on low-power microcontrollers. Hardware EtherCAT Slave Controllers (ESCs) handle time-critical communication tasks, allowing the application microcontroller to focus on sensor acquisition and local processing. This separation is crucial for tactile patches, where computational resources are limited and energy efficiency is a design constraint.
For these reasons and based on previous research in *Baglini et al. (2010)* and *Baglini et al. (2014)*, EtherCAT was selected as the communication backbone for the distributed tactile sensing architectures developed in this work. The following section describes the concrete system architecture adopted for CySkin and ProxySKIN and details the integration of EtherCAT within the tactile skin modules.

3.5.3 Distributed Data Management and Network Architecture

The adoption of EtherCAT as communication backbone enables an efficient and scalable data management strategy for large-area tactile skins composed of heterogeneous sensing patches. In such distributed systems, slave nodes are typically associated with local sensing units and are required to transmit relatively small payloads (tens of bytes per sensor) at high update rates. EtherCAT supports this operating condition by allowing multiple slave devices to exchange process data within a limited number of concatenated Ethernet frames, each with a maximum payload of 1500 bytes.
In the CySkin and ProxySKIN architectures, the design goal is to minimize the number of EtherCAT slave devices while maximizing the amount of sensory data collected per communication cycle. This approach reduces system complexity, wiring overhead, and power

consumption, while maintaining deterministic timing behavior. As a consequence, each EtherCAT slave is responsible for aggregating data from multiple sensor patches operating at relatively low sampling frequencies.

A representative example is provided by the ProxySKIN architecture, where a single EtherCAT slave collects data from arrays of Time-of-Flight (ToF) proximity sensors and CySkin tactile patches. An array of 10 ToF sensors generates approximately 3220 bytes every 66.7 ms, while 100 CySkin modules (corresponding to approximately 1100 tactile taxels) generate around 2200 bytes at 20 Hz. Since a single Ethernet frame cannot accommodate the entire payload produced by a slave device in one cycle, the data are divided into multiple segments that are transmitted sequentially over consecutive EtherCAT cycles.

Specifically, the payload generated by a slave device can be split into segments of approximately 1280 bytes, which are then inserted into the EtherCAT datagram and forwarded to the master node across multiple communication cycles. This segmentation strategy allows the system to preserve deterministic timing while efficiently utilizing the available bandwidth. Fig. 3.21 schematically illustrates the sequence of operations across two consecutive EtherCAT cycles, showing how payload segments are progressively transmitted and collected by the master node.

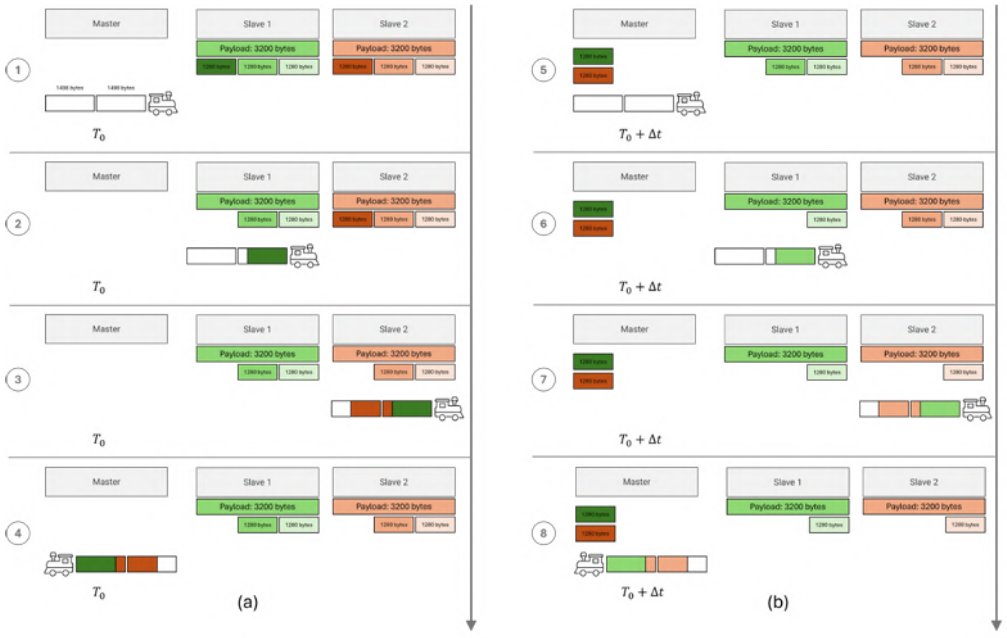

Figure 3.21 Schematic representation of the EtherCAT data management process. Sensor data generated by each slave are divided into multiple payload segments and sequentially transmitted to the master node over consecutive EtherCAT cycles.

An alternative approach would be to limit the number of sensors connected to each slave node in order to fit the entire payload within a single Ethernet frame. However, this solution would significantly increase the number of required slave devices, microcontrollers, power supplies, and communication cables, leading to higher system cost and reduced modularity. The adopted segmentation strategy therefore represents a more scalable and cost-effective solution for large-area tactile skins.
This distributed architecture demonstrates the capability of EtherCAT to support synchronized, high-throughput data acquisition from heterogeneous sensing modalities while preserving deterministic timing behavior. The modular structure of the system allows independent operation of sensing devices and facilitates integration on complex robotic surfaces, representing a key enabler for scalable tactile and multimodal robotic skins.
Fig. 3.22 illustrates the EtherCAT-based communication architecture for distributed sensing networks.

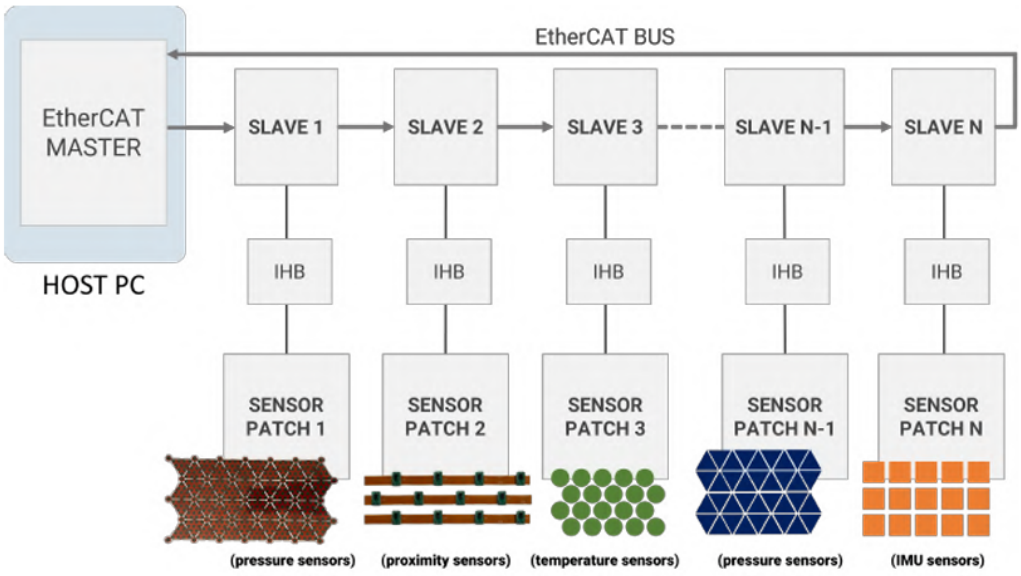

Figure 3.22 Schematic representation of the EtherCAT-based communication architecture for distributed sensing networks. Five main components are highlighted: the EtherCAT master, the physical bus connecting the Host PC to the EtherCAT slaves, the network of slave devices, the Intelligent Hub Board (IHB) microcontroller and patches of different types of sensors.

3.5.4 Experimental Setup for Validation

The experimental validation of the EtherCAT-based communication framework described in 3.5.3 was performed using a ProxySKIN sample composed of 12 CySkin tactile patches and two arrays of 10 proximity sensors as showed in Fig. 3.23. The network was implemented in a non-redundant daisy-chain topology and consisted of five EtherCAT slave devices based on the Infineon XMC4300 microcontroller, miniaturized and customized for the purpose and illustrated in Fig. 3.24. Two slaves were dedicated to proximity sensing, while three slaves acquired tactile data from CySkin patches. The EtherCAT master was implemented on a standard PC running a real-time patched Linux kernel and using the Simple Open EtherCAT Master (SOEM) library.

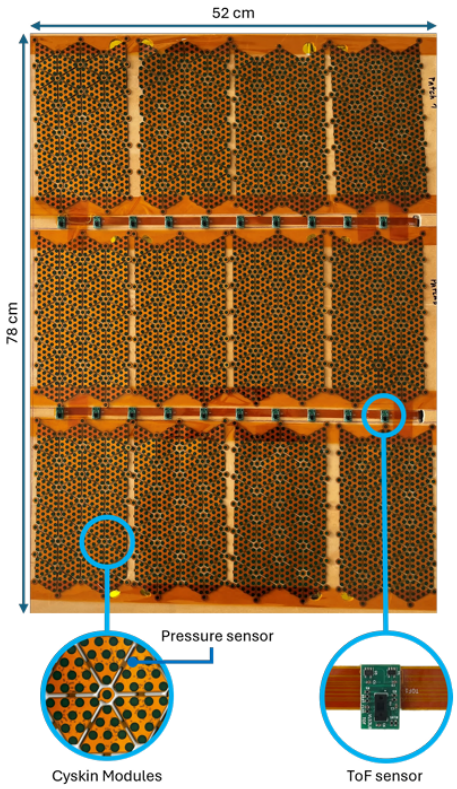

Figure 3.23 Sample of ProxySKIN (52 *cm* x 78 *cm*), the distributed multi-modal sensing architecture used to test the implemented EtherCAT communication infrastructure. This sample integrates two arrays with 10 proximity sensors and twelve patches of CySkin with 515 pressure sensors.

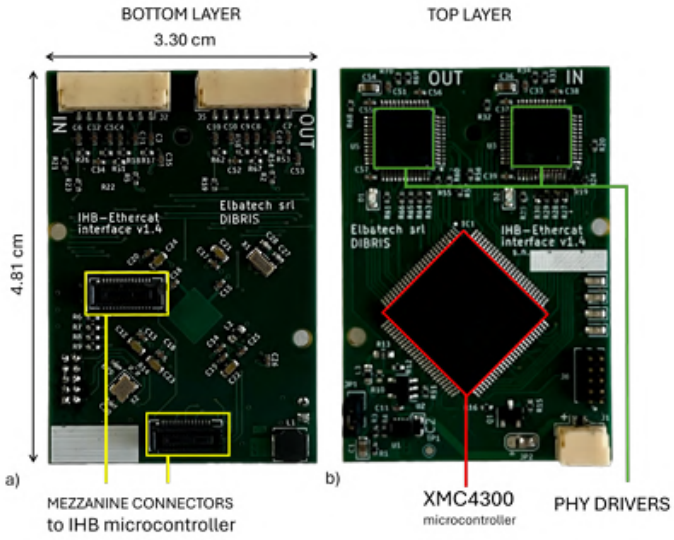

Figure 3.24 EtherCAT slave PCB measuring 4.81 x 3.30 cm. **a)** Bottom layer: in yellow are highlighted the mezzanine connectors to the IHB microcontroller, that is "piggy-backed" to the EtherCAT PCB. Typical RJ-45 connectors are replaced with 2 small SMD connectors, positioned at the top of the board. Bypass capacitors and other decoupling parts are positioned very close to the microcontroller power pins. **b)** Top layer: The PHY-drivers labeled "IN" and "OUT", highlighted in green, are not coupled to isolation transformers. The XMC4300 controller is below them, 45 degrees-oriented, to optimize the trace routing.

To evaluate EtherCAT network performance, five interrelated metrics are considered and discussed in the next sections: the *Round-Trip Time*, the *Slave Minimum Cycle Time*, the *Master Minimum Cycle Time*, the *EtherCAT Cycle Time* and the *Overall Data Transmission Period*. These parameters directly impact the robot's response time and behavior and are influenced by the number of sensors handled by the network and their data payload.

3.5.5 Round-Trip Time

The *Round-Trip Time* represents the time required by an EtherCAT frame to leave the master node, traverse all slave devices in the network, and return to the master. This parameter, also referred to as *Frame Latency*, depends exclusively on hardware-related propagation delays and directly affects the minimum achievable cycle time of the EtherCAT master.
Following the analytical model proposed in *Baglini et al. (2010, 2014)*, the round-trip time can be expressed as:

$$T_{\text{ecat}} = N_{\text{sl}} \left(T_{\text{ecat\_fwd}} + T_{\text{data}}\right) + N_{\text{cables}} T_{\text{medium}} + n_{\text{fr}} T_{\text{eth}} + T_{\text{ecat\_ov}} + T_{\text{pad}} \tag{3.8}$$

where N_{sl} is the number of EtherCAT slaves, $T_{\text{ecat\_fwd}}$ is the forwarding delay introduced by each slave, T_{data} is the transmission time of the process data payload, N_{cables} is the number of Ethernet links, T_{medium} accounts for signal propagation delays, n_{fr} is the number of Ethernet frames per cycle, T_{eth} is the Ethernet overhead time, $T_{\text{ecat\_ov}}$ represents the EtherCAT protocol overhead, and T_{pad} is the padding time required to complete the Ethernet frame.
The round-trip time was theoretically evaluated considering slave payloads limited to a maximum of 1480 bytes, corresponding to the maximum data capacity of a single Ethernet frame. Larger payloads were not considered in this analysis, since they are segmented and transmitted over multiple EtherCAT cycles as described in Section 3.5.3.

n_{ToFs} / n_{slaves}	1		2		3		4	
	T_{delay} [μs]	n_{frames}	T_{delay} [μs]	n_{frames}	T_{delay} [μs]	n_{frames}	T_{delay} [μs]	n_{frames}
1	31.755	1	57.515	1	83.275	1	109.04	1
2	60.470	1	111.99	1	166.55	2	218.07	2
3	89.185	1	169.51	2	246.79	2	327.11	3
4	117.90	1	223.98	2	330.06	3	436.14	4
5	149.66	2	281.50	3	413.34	4	545.18	5
6	178.37	2	335.97	3	493.57	4	654.21	6
7	207.09	2	393.49	4	576.85	5	763.25	7
8	235.64	2	447.80	4	659.96	6	869.08	7
9	264.36	2	502.28	4	740.20	6	978.12	8
10	296.11	3	559.79	5	823.47	7	1087.2	9
11	324.82	3	614.27	5	906.75	8	1196.2	10
12	353.54	3	671.78	6	986.98	8	1305.2	11
p_{sl} [bytes]	324		646		968		1290	

Table 3.9 Round trip time analysis (T_{delay}) expressed in μs, as a function of the number of EtherCAT slaves (n_{slaves}) and ToF sensors (n_{ToFs}) connected to to each slave device. n_{frames} represents the number of Ethernet frames needed to transmit the payload of all the slave devices within an EtherCAT cycle time. p_{sl} represents the sensor data payload of each slave device expressed in bytes.

Table 3.1 presents the results obtained when applying the mathematical model described in Equation 3.8 to a varying number of EtherCAT slaves (ranging from 1 to 12) and ToF sensors (ranging from 1 to 4).
Results show that the frame delay affecting the master minimum cycle time is limited to hundreds of microseconds and in the worst case configuration it never exceeds 1.5 *ms*. These values are suitable for ProxySKIN applications, since the sensors' sampling rate is rather slow (15 Hz). The same considerations apply to CySkin and other sensing devices with comparable performance.

3.5.6 Slave Minimum Cycle Time

The *Slave Minimum Cycle Time* represents the minimum time required by an EtherCAT slave to perform cyclical sequences of calculations and data copying tasks *(System, B. I. (2023))*. Unlike the round-trip time, this parameter does not affect frame propagation through the network, since software processing occurs in parallel with physical data transmission. However, it contributes to the minimum achievable cycle time of the EtherCAT master.
The software operations impacting the slave minimum cycle time include: copying output process data from the SyncManager to local memory, processing the output data, acquiring input data from local memory, and copying input process data back to the SyncManager.
This parameter was statistically evaluated by accessing standard EtherCAT objects 0x1C32 and 0x1C33, which store the SyncManager input/output timing parameters *(System, B. I. (2023))*. In particular, entry 0x1C32:05 provides the minimum cycle time (expressed in *ns*) supported by the slave device. Table 3.10 presents the results obtained for different network configurations, by analyzing 2×10^4 data samples from varying number of EtherCAT slaves (n_{slaves}) ranging from 1 to 5.

slave_id / n_{slaves}	1		2		3		4		5	
	μ [μs]	σ [μs]	μ [μs]	σ [μs]	μ [μs]	σ [μs]	μ [μs]	σ [μs]	μ [μs]	σ [μs]
1	465.59	0.04	/	/	/	/	/	/	/	/
2	540.89	1.93	465.59	0.02	/	/	/	/	/	/
3	624.61	2.62	603.66	2.27	465.84	0.04	/	/	/	/
4	707.87	3.56	687.85	3.91	672.79	0.02	466.12	0.01	/	/
5	780.83	5.68	735.02	5.08	670.96	1.98	715.47	3.38	466.19	0.05

Table 3.10 Slaves minimum cycle time statistical analysis ($T_{\text{min\_cycle}}$). The analysis considers 20000 samples collected by a varying number of EtherCAT slaves (n_{slaves}). *slave_id* refers to the unique identifier assigned to the slave devices. Mean values (μ) and standard deviations (σ) are expressed in microseconds [μs].

By increasing the number of EtherCAT slaves, and consequently the number of sensors connected to the network, higher mean values and standard deviations for the slaves' minimum cycle time can be observed. This is consistent with what was expected, because an increased number of datagrams circulating through the network requires slave devices to perform additional software operations on the input/output process data objects.

3.5.7 Master Minimum Cycle Time

The *Master Minimum Cycle Time* is defined as the shortest time interval required by the EtherCAT master to perform two consecutive input/output data exchanges with all slave

devices in the network. This parameter depends on both the hardware-related round-trip time and the software-related slave minimum cycle time.
To experimentally evaluate this parameter, the time delay between transmission and reception of concatenated Ethernet frames was statistically analyzed on the master node for different network configurations. Table 3.11 shows the frame delay observed for the proposed experimental setup in different network configurations, by varying the number of EtherCAT slaves (n_{slaves}) from 1 to 5. The statistical analysis focuses on 3×10^4 samples and shows that the master node can perform an input/output data exchange with the slave devices within hundreds of microseconds. The resulting values are significantly higher than the theoretical results computed for the round-trip time, because preliminary processing operations on the raw data are also considered.

	n_{slaves}									
	1		2		3		4		5	
	μ [μs]	σ [μs]	μ [μs]	σ [μs]	μ [μs]	σ [μs]	μ [μs]	σ [μs]	μ [μs]	σ [μs]
T_{delay}	524.33	60.79	524.33	62.31	744.61	71.87	753.12	66.76	991.94	73.02
T_{ecat}	782.06	70.29	831.06	72.65	944.46	71.87	950.95	77.11	1.14×10^3	82.84
T_{full_data}	2.34×10^3	210.86	2.49×10^3	217.95	2.83×10^3	215.63	2.85×10^3	231.33	3.41×10^3	248.53

Table 3.11 Statistical analysis of the frame delays (T_{delay}), EtherCAT cycle time (T_{ecat}) and overall data transmission period (T_{full_data}). The analysis considers 30000 samples collected by a varying number of EtherCAT slaves (n_{slaves}). Mean values (μ) and standard deviations (σ) are expressed in microseconds [μs].

However, the master minimum cycle time depends also on the slaves minimum cycle time. Indeed, software operations performed by the slave devices on the process data run in parallel to the physical propagation of the EtherCAT datagrams through the network. Therefore, when the cyclical Ethernet frames return to the master node, EtherCAT slaves might still be processing input/output data.
This behavior can be clearly seen in Figure 3.25, presenting qualitative results on a network with two slave devices. On the screen capture of the oscilloscope are highlighted 4 signals:

- *Yellow Signal*: refers to the EtherCAT master thread running on the PC. The two spikes highlighted in red indicate a new transmission of Ethernet frames to the slave devices. The spike highlighted by the green arrow indicates the reception of the Ethernet frames belonging to the previous data transmission, coming back from the network.
- *Cyan Signal*: indicates the data transmission over the MII interface from the input PHY driver of the first EtherCAT slave to the XMC4300 microcontroller. The time interval between the first yellow spike and the data transmission on the MII interface

represents the hardware propagation delay of the Ethernet frame from the master node, consistent with the theoretical values shown in Section 3.5.5.

- *Magenta Signal*: refers to the minimum cycle time of the second slave device.
- *Green Signal*: refers to the software of the first EtherCAT slave. Specifically, it represents the slave minimum cycle time, triggered by the SyncManager event and kept active until the end of the processing operations on the input/output process data objects.

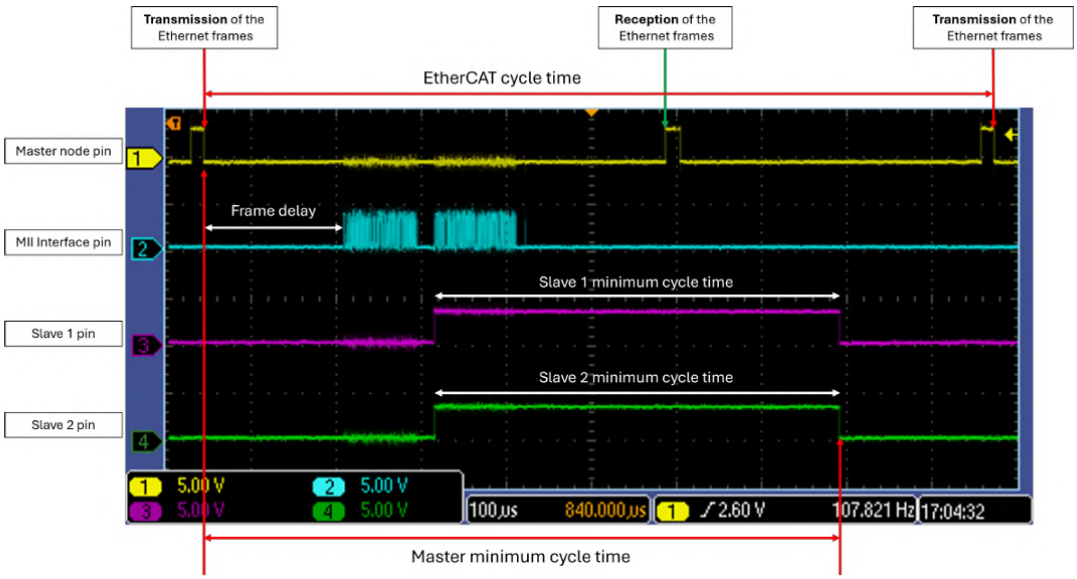

Figure 3.25 Screen capture of the oscilloscope showing important performance parameters of the EtherCAT-based communication network. Reported data refer to an EtherCAT network with 2 slave devices collecting data from patches of pressure sensors. *Yellow Signal* is triggered by the thread of the master EtherCAT right before a transmission of the data frames to the slave devices and immediately after the reception of the data frames from the network. The time interval between two consecutive Ethernet frame transmissions represent the EtherCAT cycle time. *Cyan Signal*: is probed on a pin of the input PHY driver of the first EtherCAT slave and represents the data transmission over the MII interface to the XMC4300 microcontroller. *Magenta Signal* represents the minimum cycle time of the first slave, i.e. the time required to perform cyclical sequences of calculations and data copying tasks. *Green Signal* represents the minimum cycle time of the second slave.

When the master node receives the Ethernet frames (second spike of the yellow signal) both EtherCAT slaves are still engaged in copying and processing input/output data (green and

magenta signals). Therefore, to ensure a reliable and effective data communication throughout the network, it's essential to guarantee that the EtherCAT slaves have updated their process data objects before transmitting a new datagram.
The master minimum cycle time is qualitatively evaluated by analyzing the signals on the oscilloscope for different network configurations. In particular, the time interval between the transmission of the Ethernet frames from the master node and the end of processing operations on the input/output process data are computed. The master minimum cycle times computed for an increasing number of EtherCAT slaves are respectively: 700 μs with a single slave, 780 μs with 2 slaves , 850 μs with 3 slaves, 910 μs with 4 slaves and 103 μs with 5 slaves.

3.5.8 EtherCAT Cycle Time and Data Transmission Period

The *EtherCAT Cycle Time* represents the time interval between the transmission of two consecutive EtherCAT datagrams by the master. In order to guarantee reliable communication, a constant delay is added to the frame delays analyzed in Section 3.5.7, ensuring that all slave devices have completed their processing operations before the transmission of a new frame. Experimental results show that an additional delay of approximately 250 μs is sufficient to ensure stable and deterministic communication. In Table 3.11, T_{ecat} represents the EtherCAT cycle time computed for different network configurations, by varying the number of slave nodes (n_{slaves}) from 1 to 5. The statistical analysis focuses on 3×10^4 samples and shows that the master node can perform two consecutive input/output data exchanges with the slave devices within few milliseconds.
Instead, the *Data Transmission Period* represents the time required to transmit the full sensor payload from all slave devices to the host PC through consecutive EtherCAT cycles. This parameter is a multiple of the EtherCAT cycle time and depends on the number of payload segments required to transmit the complete sensor data.
In Table 3.11, $T_{\text{full\_data}}$ shows the data transmission period computed for different network configurations, by varying the number of slave nodes (n_{slaves}) from 1 to 5. The statistical analysis focuses on 3×10^4 samples and shows that the master node can successfully transfer the overall sensors data payload within few milliseconds. Results show that the data transmission period has little relevance when compared to the sampling interval of the considered sensors (66.7 ms), allowing the master to collect the full data payload before the next sampling cycle.
Figure 3.26 shows the visualization of the ProxySKIN sensing architecture collected by the

EtherCAT network during a physical interaction experiment. The full video of the interaction demo can be found at this link.

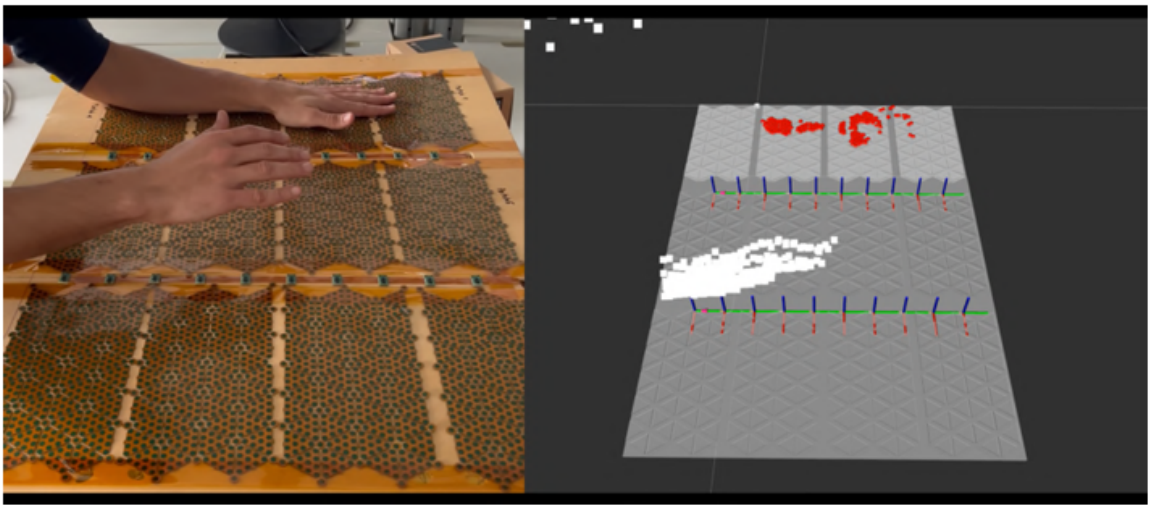

Figure 3.26 Picture of the experimental setup and corresponding visualization of data collected by ProxySKIN. Data acquired through the EtherCAT network are processed and displayed via the ROS framework. The red dots represent the active pressure sensors, while the proximity point cloud is visualized in white.

3.5.9 Conclusions

This section presented the design, implementation, and experimental validation of an EtherCAT-based communication architecture for large-area distributed tactile sensing systems. The proposed framework was specifically developed to address the scalability, determinism, and synchronization requirements arising from the integration of CySkin and ProxySKIN architectures, where heterogeneous sensing modalities and a large number of distributed taxels must be managed in real time.

The analytical and experimental evaluation of key performance parameters—including round-trip time, slave and master minimum cycle times, EtherCAT cycle time, and overall data transmission period—demonstrated that the proposed architecture provides bounded and predictable communication latencies. Even in the worst-case configurations, the measured delays remain well below the sampling intervals of both tactile and proximity sensors, confirming the suitability of EtherCAT for large-area robotic skin applications.

The distributed data management strategy based on payload segmentation over consecutive EtherCAT cycles proved effective in maximizing bandwidth utilization while minimizing the

number of required slave devices. This approach preserves modularity and reduces system complexity, enabling scalable integration of tactile patches and proximity sensors without compromising real-time performance.

The validity of the proposed communication architecture was further demonstrated through its deployment within the ProxySKIN system, integrated on an industrial robotic platform. In particular, EtherCAT was successfully used to manage multimodal tactile and proximity sensing during physical interaction experiments conducted within the SESTOSENSO project *(European Horizon Project (2025))*. As shown in Fig. 3.27, ProxySKIN was mounted on a UR10 manipulator and employed in a real-world interaction scenario, where synchronized tactile and proximity data were acquired, transmitted, and visualized in real time.

Overall, the results presented in this chapter confirm that EtherCAT represents a robust and scalable solution for distributed tactile and multimodal sensing architectures. Its deterministic behavior, precise time synchronization, and efficient data handling capabilities make it a key enabling technology for next-generation robotic skins, supporting safe physical human–robot interaction and large-area tactile perception.

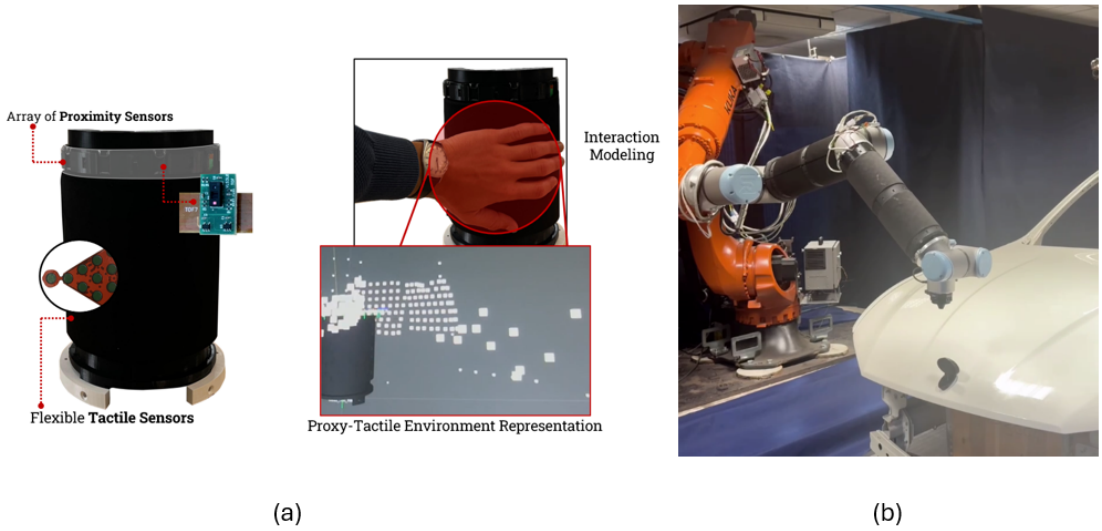

Figure 3.27 (a) integrated cover for a UR10 robot with ProxySKIN and equipped within an EtherCAT network and its response. **(b)** UR10 robot mounted on a KUKA manipulator covered with ProxySKIN and its EtherCAT-base communication infrastructure.

Chapter 4

PeSkin: Screen Printed Capacitive Tactile Sensors

4.1 Motivation and State of the Art

Flexible capacitive tactile sensors have become a cornerstone technology for robotic skins and physical human–robot interaction (HRI), due to their intrinsic advantages in terms of low power consumption, high sensitivity, mechanical compliance, and compatibility with large-area integration. Capacitive sensing enables non-destructive deformation monitoring of soft dielectric layers and allows the realization of distributed tactile arrays with relatively simple readout electronics.

Over the last decade, numerous approaches have been proposed to enhance sensitivity, linearity, and mechanical robustness of flexible capacitive pressure sensors. A common strategy relies on engineering the dielectric layer through micro-structuring, porosity, or hierarchical architectures in order to amplify thickness variations under applied pressure. For instance, micro-porous PDMS-based dielectrics have demonstrated significant sensitivity improvements in the low-pressure regime, as shown in *Choi et al. (2020)*, where porous elastomers enabled enhanced capacitive variation compared to bulk structures. Similarly, bio-inspired micro-structured dielectrics have been employed to achieve high sensitivity at low pressures, often at the expense of fabrication complexity *(Jin et al. (2024))*.

Other approaches focus on nanocomposite dielectric materials, such as CNT/PDMS or graphene-based systems, to tailor the effective permittivity and mechanical response of the sensing layer *(Fu et al. (2021))*. While these solutions provide improved sensitivity and tunable mechanical properties, they typically involve many steps in the fabrication processes including mixing, molding, vacuum degassing, and precision assembly, which may limit

scalability and repeatability in large-area manufacturing.

From a manufacturing perspective, additive printing techniques such as screen printing and inkjet printing have emerged as promising methodologies for low-cost and scalable fabrication of flexible capacitive sensors. Screen-printed capacitive pressure sensors on PET or Kapton substrates have demonstrated the feasibility of thin, flexible, and lightweight devices *(Eshkeiti et al. (2014))*, enabling thicknesses below 100 μm and compatibility with roll-to-roll processes. However, many of these implementations are limited to single sensors or small matrices and do not explicitly address large-area modular integration for robotic skin applications. Fig. 4.1 illustrates the aforementioned technologies.

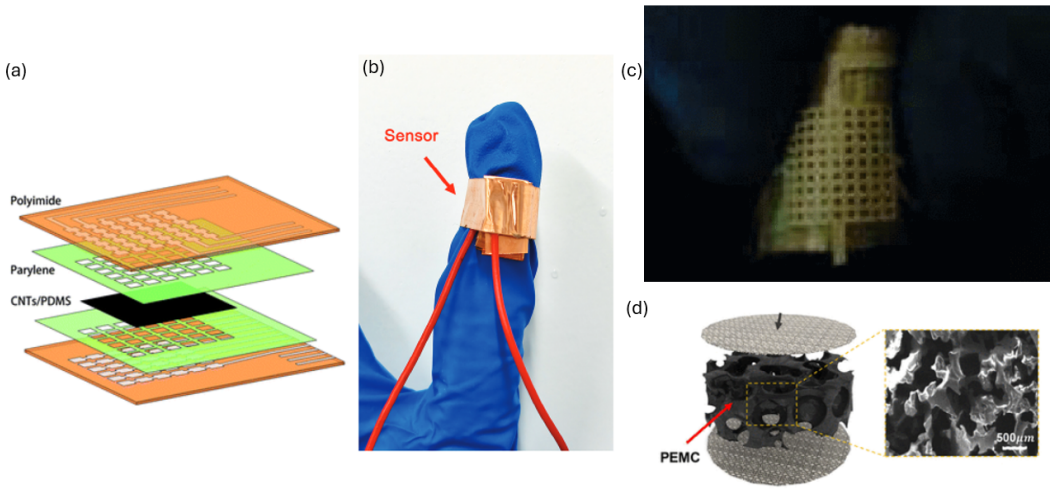

Figure 4.1 Overview on single and matrices of printed capacitive tactile sensors: **(a)** The structure of a 6 $\times$ 6 capacitive tactile sensor. The sensor is composed of two AU-coated polyimide films as top and bottom electrodes and a CNT/PDMS film as the dielectric material *(Fu et al. (2021))*. **(b)** Fabricated flexible pressure sensor based on 3D bio-inspired kapok structure (3DBIKS) *(Jin et al. (2024))*. **(c)** Manufactured screen-printed capacitive tactile sensor *(Eshkeiti et al. (2014))*. **(d)** Schematic diagram of the PEMC-based pressure sensor using conductive fabric electrodes and SEM image of the PEMC structure *(Choi et al. (2020))*.

In the context of robotic tactile systems, scalability, modularity, and integration capability are as critical as intrinsic sensitivity. Large-area tactile systems such as those discussed in *Maiolino et al. (2013)* highlight the importance of balancing mechanical robustness, spatial resolution, and ease of integration on complex robotic surfaces.

Within this framework, PeSkin is conceived as a printed, modular, and scalable capacitive tactile sensing platform specifically designed to bridge the gap between laboratory-scale

high-sensitivity devices and deployable large-area robotic skins. Rather than maximizing sensitivity through complex micro-structuring or nanocomposite formulations, PeSkin focuses on:

- Fully screen-printed electrode architectures compatible with large-sheet manufacturing and lamination-based assembly enabling repeatable stacking of upper and lower electrodes making it **Scalable** and **Low-cost**;
- Air-gap-based capacitive transduction defined by screen-printed dielectric layers keeping a **High Sensitivity** and optimal sensor performances;
- Compatibility with curved and cylindrical robotic surfaces enabling **Flexibility** over different shapes.

This design philosophy prioritizes manufacturability, robustness, and scalability while maintaining high sensitivity for robotic manipulation and safe human–robot interaction. The following sections detail the design rationale, fabrication process, experimental characterization, and comparative analysis of PeSkin with respect to the state of the art.

4.2 Design and Manufacturing of the PeSkin 6×24 Patch

4.2.1 Sensor Architecture and Structural Design

PeSkin architecture is based on a fully screen-printed capacitive air-gap structure specifically optimized for large-area tactile integration on robotic platforms. The sensing patch consists of a 6×24 matrix (144 taxels) fabricated on flexible PET substrates with a thickness of 50 μm.
Each taxel has a circular geometry with a diameter of 3.5 mm and operates according to a parallel-plate capacitive principle:

$$C = \frac{\varepsilon_0 A}{d} \tag{4.1}$$

where A is the electrode overlapping area and d is the air-gap thickness.
The device architecture, schematically illustrated in Fig. 4.2 and Fig. 4.3, is composed of two laminated PET substrates and five printed functional layers forming an air-cavity-based transduction structure.

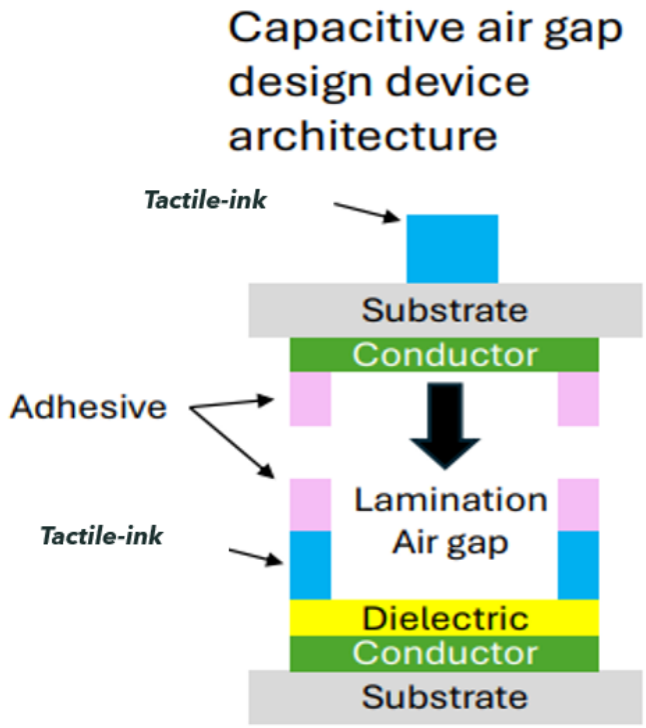

Figure 4.2 Capacitive air-gap PeSkin architecture. The structure consists of two PET substrates, printed conductive electrodes, dielectric layer, tactile ink pillars and adhesive layers forming a laminated air cavity.

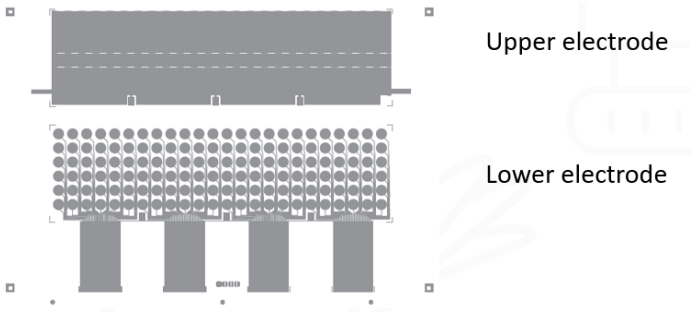

Figure 4.3 Layout of the two electrodes screen-printed on the two different PET 50 μm substrates.

The layer stack from top to bottom is:

- Screen-printed tactile ink (force concentration pillar $\approx$ 125 μm)
- PET substrate (50 μm)
- Printed silver conductor (top electrode $\approx$ 7.5 μm)
- Adhesive layer ($\approx$ 12.5 μm)

- Air gap (laminated cavity $\approx 150\ \mu$m)
- Adhesive layer ($\approx 12.5\ \mu$m)
- Screen-printed tactile ink ($\approx 125\ \mu$m)
- Printed dielectric layer ($\approx 15\ \mu$m)
- Printed silver conductor (bottom electrode $\approx 7.5\ \mu$m)
- PET substrate (50 μm)

The air gap is defined during lamination by the printed adhesive and dielectric layers, creating a controlled cavity thickness. When an external normal force is applied, the upper PET substrate bends locally, reducing the air-gap thickness and increasing the capacitance. The circular taxel geometry with 3.5 mm diameter was selected as a trade-off between spatial resolution, mechanical robustness, and manufacturability through screen printing. The resulting active sensing area of the 6×24 matrix is approximately 44×170 mm^2. The total thickness of the laminated structure is approximately 300 μm, excluding the tactile pillar height.

4.2.2 Materials and Printed Functional Layers

The PeSkin 6×24 patch is entirely fabricated using screen-printable materials compatible with large-area additive manufacturing processes.

Substrate Flexible PET films with thickness 50 μm are used for both top and bottom layers, ensuring mechanical compliance and high sensitivity due to reduced bending stiffness.

Conductive Electrodes Silver conductive ink is screen-printed (CXT from Nagase dried at 120°C) to define the circular electrodes and routing lines. The typical cured thickness ranges between 5–10 μm. The electrode diameter is 3.5 mm.

Dielectric Layer A UV-curable dielectric ink (5018 from DuPont) is printed on the bottom substrate to electrically isolate routing lines and define part of the cavity geometry. The dielectric thickness is typically 10–20 μm.

Adhesive Layer A thermally curable adhesive ink (D142 from Kiwo dried at 70°C) is printed on both substrates to enable lamination and cavity sealing. The adhesive also defines the effective air-gap boundary.

Tactile Ink A high-viscosity UV-curable tactile ink (Braille varnish from Marabu) is printed on the outer surface of the top substrate to form localized force-concentration pillars. These structures improve pressure transfer efficiency and enhance sensitivity in the low-force regime.

4.2.3 Fabrication Process

The fabrication of the 6×24 PeSkin patch follows a fully additive screen-printing process:

1. Screen printing of bottom silver electrodes on PET and cured at 120°C.
2. Printing and UV-curing of the dielectric layer.
3. Printing and UV-curing of the tactile ink layer.
4. Printing of adhesive layer on the bottom substrate and cured at 70°C.
5. Screen printing of top silver electrodes on a second PET sheet and cured at 120°C.
6. Printing of tactile ink pillars on the external side of the top PET and UV curing.
7. Printing of adhesive layer on the top substrate and cured at 70°C.
8. Alignment and lamination of the two substrates under controlled pressure and temperature.

Fig. 4.4 and Fig. 4.5 illustrate the steps of the described procedure.
The final device is thin, flexible, and mechanically compliant, making it suitable for integration on flat and curved robotic surfaces. Fig. 4.6 shows the fabricated sensor.

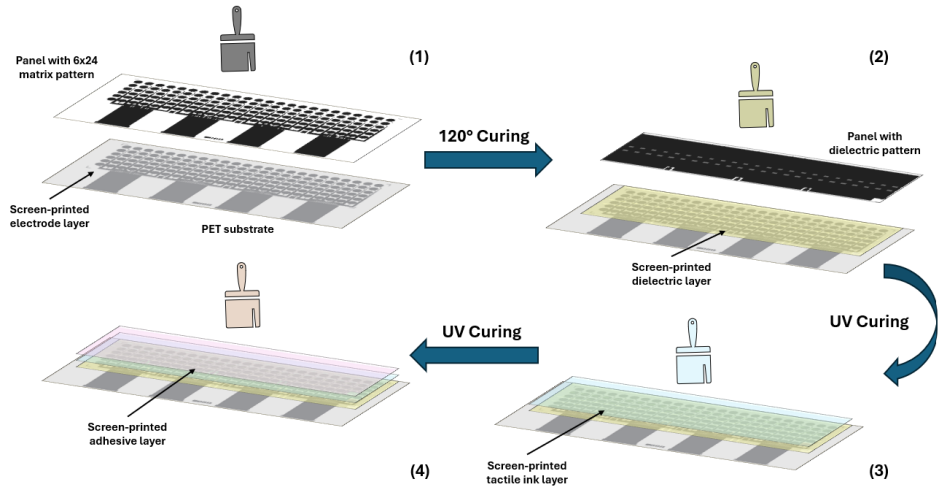

Figure 4.4 Overview of the manufacturing process: **(1)** First a layer of silver ink ($\approx 7.5\ \mu m$) was brushed on a panel with a 6×24 matrix pattern to screen-print the electrodes on the front of the 50 μm PET substrate. **(2)** After curing the sample at 120°C we brushed a layer of dielectric ink ($\approx 15\ \mu$m) on a panel designed to print on top of the taxels area **(3)** After a step of UV curing we screen-print on the PET substrate a layer of tactile ink ($\approx 125\ \mu$m) to control the height of the air gap. **(4)** After another step of UV curing a layer of adhesive ($\approx 12.5\ \mu m$) was applied to be able to attach the other electrode layer and cured at 70°C.

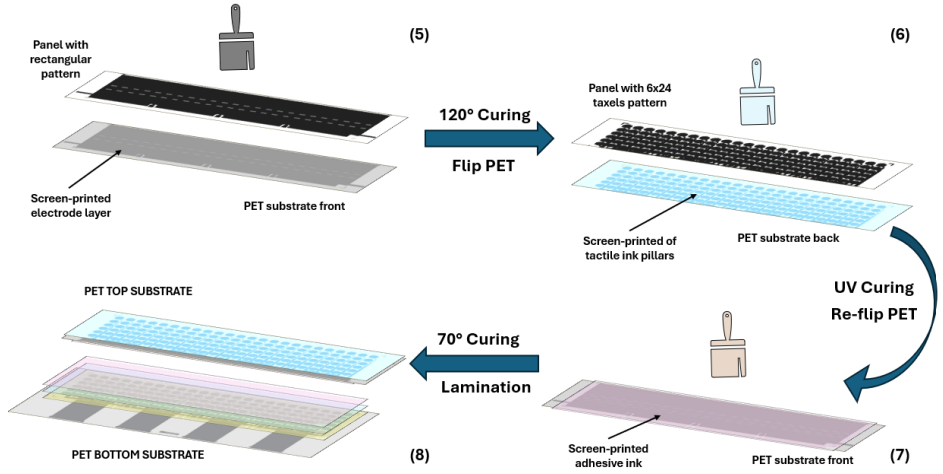

Figure 4.5 Overview of the manufacturing process: **(5)** First a layer of silver ink ($\approx 7.5\ \mu m$) was brushed on a panel with a filled rectangular pattern to screen-print the electrode on the front of the 50 μm PET substrate. **(6)** After curing the sample at 120°C we flip the PET and screen-print a layer of tactile ink ($\approx 125\ \mu$m) **(7)** After UV curing the sheet we re-flip the PET and screen-print on the electrode a layer of adhesive ink ($\approx 12.5\ \mu$m) to attach it to the previous printed layer. **(8)** After curing at 120°C we proceed to laminate the two screen-printed electrodes to create the capacitive tactile sensor.

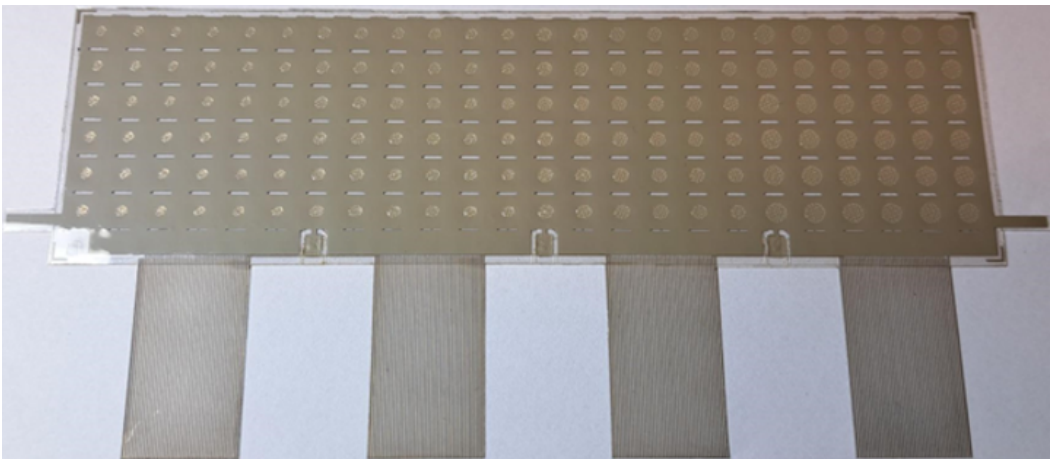

Figure 4.6 Picture showing one 6×24 sensor array that has been manufactured via screen printing and lamination.

4.2.4 Electronic Design and Readout Architecture

The 6×24 PeSkin array is interfaced with a custom miniaturized readout board based on a Programmable System-on-Chip (PSoC) microcontroller. The PSoC platform was selected due to its integrated CapSense technology, which enables direct capacitive acquisition without requiring external analog front-end circuitry. This significantly reduces board complexity, size, and power consumption, making it suitable for modular and scalable tactile architectures.

Each miniaturized PSoC board is designed to acquire a sub-matrix of 36 taxels (6×6), operating at a sampling frequency of approximately 28 Hz. This acquisition rate was selected to ensure compatibility with robotic manipulation and physical human–robot interaction scenarios, where typical contact dynamics occur at relatively low frequencies. The achieved frame rate guarantees stable and reliable pressure mapping while maintaining low computational load. Figure 4.7 shows the schematic layout of the miniaturized PSoC board. The PCB footprint is optimized to minimize area occupation while maintaining reliable routing for the electrode connections and communication interfaces.

The readout architecture follows a matrix-scanning approach, where the upper and lower electrodes are sequentially excited and measured using the internal capacitive sensing blocks of the PSoC. The raw capacitance variations are converted into digital counts and transmitted to the host system for further processing and visualization. Figure 4.8 illustrates the communication protocol adopted to acquire and process the capacitive tactile data.

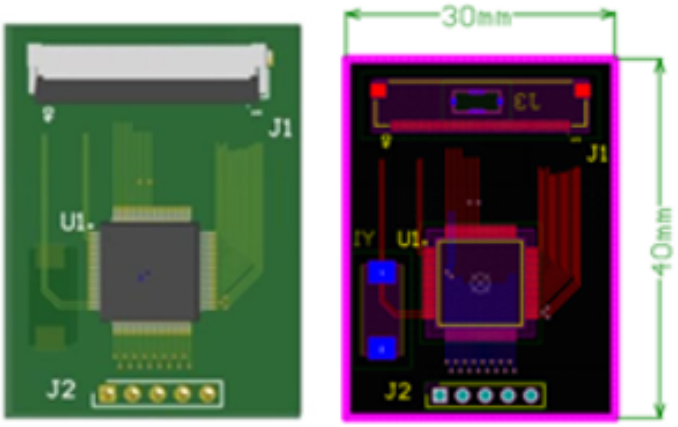

Figure 4.7 Schematic layout of the miniaturized PSoC-based readout board used for the acquisition of 36 taxels (6×6). The compact PCB design enables modular integration underneath the flexible PeSkin array.

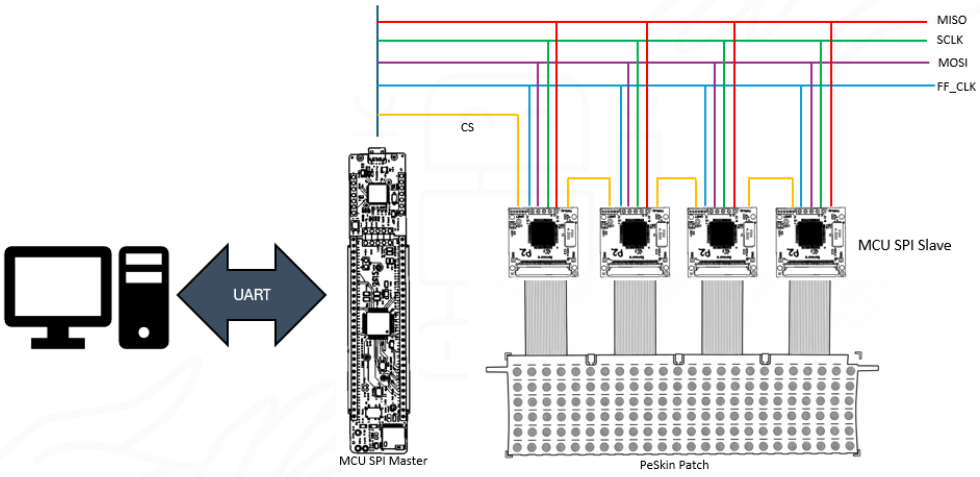

Figure 4.8 PeSkin data acquisition protocol: an SPI Master-Slave flip-flop configuration was used for gathering all the data from the sensor, these configuration allows to connect a significant number of Slave in series. After that data are sent through UART to the PC for the processing and visualization.

The final integrated system is shown in Figure 4.9. The 6×24 PeSkin array is electrically connected to four miniaturized PSoC boards through flat interconnects, each acquiring 36 taxels. The modular architecture allows independent acquisition blocks to be replicated and distributed across larger surfaces, supporting scalability toward extended robotic skins.

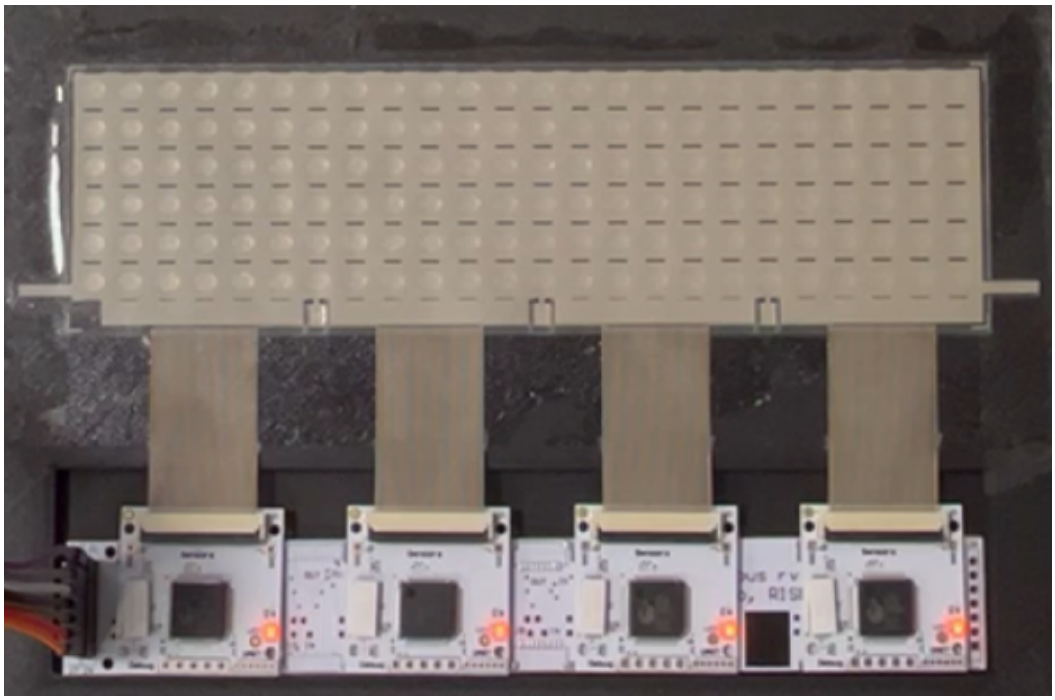

Figure 4.9 Integrated PeSkin 6×24 tactile array connected to four miniaturized PSoC readout boards. Each board acquires 36 taxels at 28 Hz, enabling distributed and scalable tactile sensing.

The modular PSoC-based architecture ensures that PeSkin can be scaled to larger matrices by replicating the acquisition units while preserving manageable sampling rates and deterministic data acquisition. This design aligns with the overall objective of developing a printable, flexible, and scalable tactile sensing platform compatible with robotic integration.

4.3 Experimental Characterization of PeSkin

4.3.1 Experimental Setup

The experimental characterization of the PeSkin 6×24 patch was carried out using the same electromechanical testing platform described in Section 3.4.1 (Fig. 3.11). The setup consists of a motorized linear stage coupled with a calibrated load cell, enabling controlled normal force application with high positional accuracy.

A cylindrical metallic indenter was mounted on the load cell and aligned orthogonally to the sensor surface. The PeSkin patch was fixed on a rigid support plate to ensure repeatable boundary conditions during the tests. Figure 4.10 shows the experimental configuration used for the characterization.

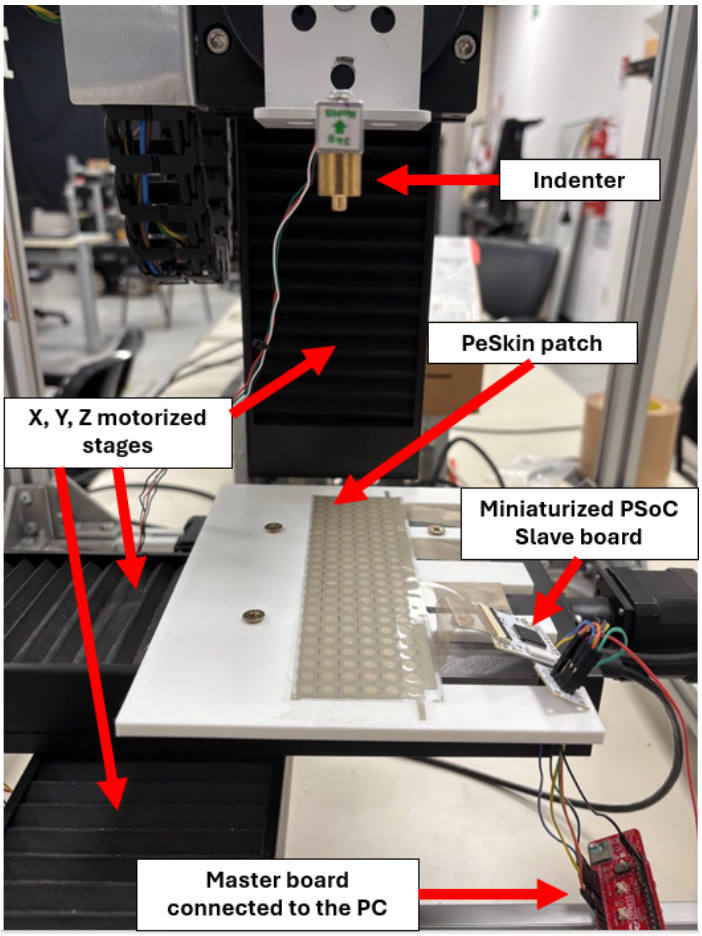

Figure 4.10 Experimental setup used for PeSkin characterization. The same motorized test bench described in Section 3.4.1 (Fig. 3.11) was adopted to apply controlled normal forces while acquiring the capacitive response adopting the communication protocol described in Section 4.2.4.

During all experiments, capacitance variations were acquired through the miniaturized PSoC-based readout board described in Section 4.2.4, operating at a sampling frequency of 28 Hz for a 6×6 sub-matrix. The raw digital counts were converted into capacitance values (C_s) and logged for post-processing. The conversion follows the equation described in the *PSoC CapSense Guide (2021)*:

$$C_s = \frac{\text{RawCount} \cdot I_{\text{mod}}}{(2^N - 1)\, V_{\text{ref}}\, F_{\text{sw}}} \tag{4.2}$$

where:

- N is the resolution of the counter (16 *bit*),

- V_{ref} is the reference voltage (3.3 V),
- F_{sw} is the switching frequency (6 MHz),
- RawCount is the sensor output digit,
- I_{mod} is the modulation current set by the IDAC.

The characterization focuses on the following performance metrics:

- Sensitivity
- Hysteresis
- Repeatability
- Time response
- Dynamic range
- Spatial resolution

These metrics provide a comprehensive evaluation of the mechanical-to-electrical transduction performance of the PeSkin architecture.

4.3.2 Sensitivity

The sensitivity, as presented in Section 3.4.4 Equation 3.4, of the PeSkin taxels was evaluated by applying controlled normal forces in the range [0 60N] for 3 times on a single sensing element and measuring the corresponding capacitance variation (ΔC) and digital output variation (ΔRaw Count).
Figure 4.11 shows the relationship between the applied force and the response of the sensor. The response exhibits a nonlinear behavior that has been approximated in three linear regions [0 1N]/[0 103kPa], [2N 10N]/[206kPa 1030kPa] and [10N 60N]/[103kPa 6180kPa].

Low-force regime In the low-force region (approximately 0–1 N/0–103 kPa), the sensor exhibits a high sensitivity due to the initial compression of the air gap and local bending of the 50 μm PET substrate. In this region, the measured sensitivity reaches approximately:

$$S_{\text{low}} = 5870 \text{ fF/N} \mid 57 \text{ fF/kPa} \tag{4.3}$$

This elevated sensitivity is mainly attributed to the strong variation of the effective air-gap thickness under small applied forces and optimal to cover both gentle contact (0–10 kPa) and manipulation like (10–100 kPa) interaction conditions (*Choi et al. (2020), Kurnaz et al. (2023)*).

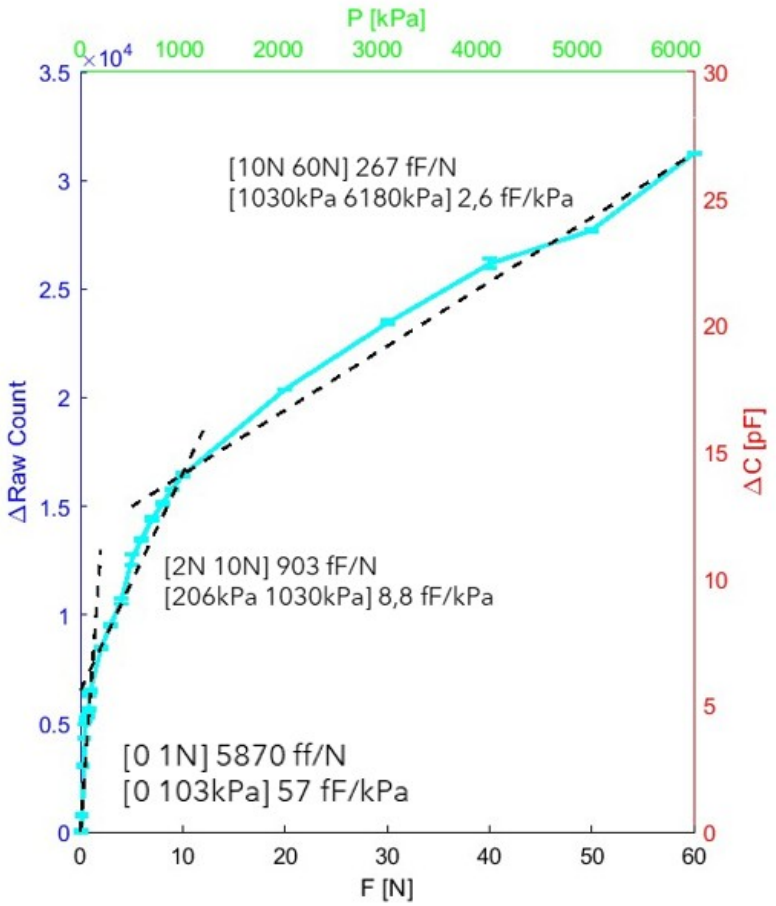

Figure 4.11 Force/Pressure response characteristic of a PeSkin taxel. The left axis represents the variation in raw digital counts, while the right axis reports the corresponding capacitance variation.

Mid-force regime In the intermediate region (approximately 2–10 N), the sensitivity decreases as the air gap compression becomes progressively limited and the mechanical response transitions toward a more linear bending-dominated behavior. The measured sensitivity in this region is approximately:

$$S_{\text{mid}} \approx 903 \text{ fF/N} \mid 8.8 \text{ fF/kPa} \tag{4.4}$$

High-force regime At higher forces (above 10 N), the structure approaches a quasi-linear regime dominated by PET deformation and limited residual air-gap variation. The sensitivity further reduces to:

$$S_{\text{high}} \approx 267 \text{ fF/N} \mid 2.6 \text{ fF/kPa} \tag{4.5}$$

The progressive reduction of sensitivity with increasing force is consistent with the air-gap capacitive model, where the capacitance variation becomes less as the cavity approaches its minimum thickness.

Overall, the PeSkin architecture demonstrates high sensitivity in the low-force regime, which is particularly relevant for safe physical human–robot interaction scenarios, while maintaining measurable and stable response up to higher force values.

Hereafter Table 4.1 reports sensitivity values from literature on capacitive tactile sensors based on printed or flexible fabrication technologies. For the PeSkin sensor, both absolute and normalized values are provided to enable comparison across different metrics. The main variability across references arises from the force or pressure range over which sensitivity is extracted and from differences in sensing area and electrode geometry. The table is therefore intended as an indicative overview rather than a strict one-to-one benchmark.

Sensitivity	Paper Reference
[0–10 N] 0.081 $\%N^{-1}$	Maddipatla et al. (2020)
[0–337 kPa] 0.0212 $\%kPa^{-1}$	Maddipatla et al. (2017)
[0.25–1.1 MPa] 0.0001145 $\%kPa^{-1}$	Ali et al. (2019)
[0–5 N] 2.70 $\%N^{-1}$	Zhu and Tairych (2021)
[0–30 kPa] 23.7 fF/kPa	Staiano et al. (2023)
[2–45 kPa] 2.50 fF/kPa	Maiolino et al. (2013)
[0–10 N] 0.088 $\%N^{-1}$	Aeby et al. (2019)
[1–12 N] 9.5 fF/N	Kosmas et al. (2021)
[0–10 N] 1 fF/N	Jagoda et al. (2012)
[0–10 N] 71 fF/N	Chandra et al. (2017)
[0–2 N] 0.558 pF/N	Wu et al. (2023)
[0–2 N] 1.921 pF/N	Cheng et al. (2023)
[1–10 N] 0.0452 $\%N^{-1}$	Wolternik et al. (2018)
[0.8–18 MPa] 0.0034 $\%kPa^{-1}$	Narakathu et al. (2012)
[0–1 N] 46.8 $\%N^{-1}$	Ramalingame et al. (2019)
[0–50 kPa] 0.003 kPa^{-1}	Ntagios et al. (2020)
[0–1 N] 31.66 fF/N	Jen et al. (2021)
[0–80 kPa] 0.02 $\%kPa^{-1}$	Cai et al. (2021)
[0–2 N] 0.487 N^{-1}	Xu et al. (2024b)
[0–10 N] 0.028 N^{-1}	Zhu et al. (2022)
[0–8 N] 0.175 pF/N	Alshawabkeh et al. (2023)
[0–1 kPa] 0.0043 fF/kPa	Peng and Lu (2015)
[0–300 kPa] 1.03 fF/kPa	Lü et al. (2017)
[0–1 N] 1.835 pF/N	Hailiang et al. (2024)
[0–55 kPa] 0.0285 $\%kPa^{-1}$	Sethumadhavan et al. (2017)
[30–116 kPa] 0.001 kPa^{-1}	Zheng et al. (2024)
[6–120 kPa] 0.0079 kPa^{-1}	Yu et al. (2023a)
[120–300 kPa] 0.0009 kPa^{-1}	Wang et al. (2025)
[0–1.5 N] 0.776 pF/N	Dong et al. (2018)
[0–1 N] 5.870 pF/N|0,88 N^{-1}|88,9 $\%N^{-1}$	**This work**
[0–103 kPa] 57 fF/kPa|0,0086 kPa^{-1}|0,86 $\%kPa^{-1}$	**This work**

Table 4.1 Comparison of sensitivity values reported in the literature and measured for the PeSkin architecture.

4.3.3 Hysteresis and Repeatability

Hysteresis and repeatability of the PeSkin taxel were evaluated through cyclic loading–unloading tests performed on a single sensing element within the force range 0–1 N (equivalent to 0–103 kPa). The test consisted of 10 consecutive loading and unloading cycles. The applied force was controlled using the electromechanical platform described in Section 4.3.1, while the corresponding output Y (expressed either as ΔRaw Count or ΔC) was continuously acquired at 28 Hz through the PSoC-based readout system.
Figure 4.12 shows the cyclic response of the taxel over the 10 loading–unloading cycles, highlighting the consistency of the output signal across repeated mechanical loads.
The repeatability error was computed as:

$$R = \sigma_Y \times 100\% \tag{4.6}$$

where σ_Y represents the standard deviation of the output signal across repeated cycles, normalized with respect to the full-scale output. The low dispersion observed across cycles confirms the stable and reproducible mechanical-to-electrical transduction of the laminated PET–air-gap structure.

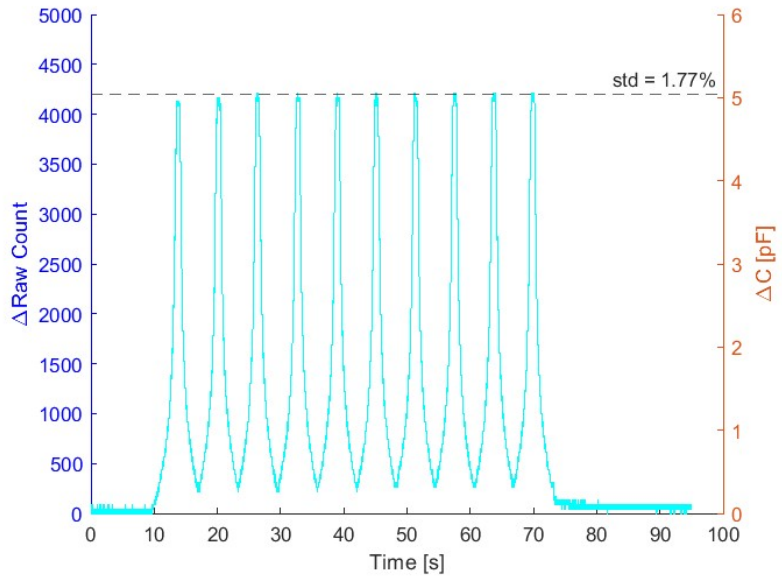

Figure 4.12 Repeatability test of a PeSkin taxel over 10 consecutive loading–unloading cycles in the range 0–1 N.

Hysteresis was extracted from the same dataset by comparing loading and unloading curves within each cycle. A representative loading–unloading characteristic is shown in Fig. 4.13. The hysteresis error was calculated as:

$$H = \frac{\max \left| Y_{\text{loading}}(F) - Y_{\text{unloading}}(F) \right|}{Y_{\text{FSO}}} \times 100\% \tag{4.7}$$

where Y_{FSO} denotes the full-scale output variation within the 0–1 N range. The measured hysteresis remains limited, indicating good elastic recovery of the air-gap structure. Minor deviations between loading and unloading curves can be attributed to viscoelastic relaxation of the printed adhesive and tactile ink layers.

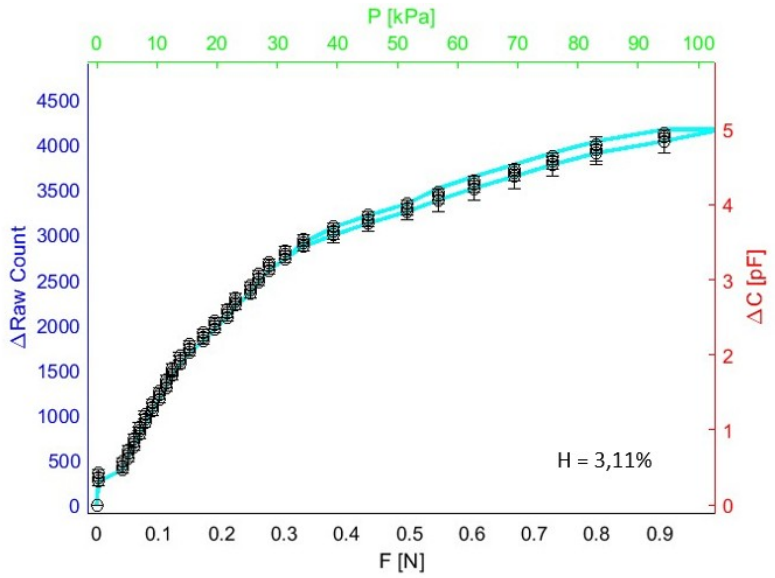

Figure 4.13 Hysteresis characterization of a PeSkin taxel within the 0–1 N range. Loading and unloading curves are reported in terms of output variation Y.

Tab. 4.2 and Tab. 4.3 show the comparison of our results within the current literature.

Hysteresis	**Paper Reference**
3.2 %	Maddipatla et al. (2020)
3.11 %	Yoon et al. (2017)
5.8 %	Hao et al. (2020)
5 %	Maiolino et al. (2013)
11 %	Kosmas et al. (2021)
4.42 %	Cheng et al. (2018)
4.2 %	Xu et al. (2024b)
6.83 %	Hou et al. (2024)
9.2 %	Li et al. (2024)
6 %	Rana et al. (2016)
4.5 %	Cheng et al. (2009)
8.4 %	Jin et al. (2024)
7.54 %	Hailiang et al. (2024)
8.8 %	Aubeeluck et al. (2024)
5.4 %	Xu et al. (2024a)
3.11 %	**This work**

Table 4.2 Comparison of hysteresis values reported in the literature and measured for the PeSkin architecture.

Repeatability	**Paper Reference**
3.2 %	Palaniappan et al. (2020)
3.33 %	Ramalingame et al. (2019)
5.47 %	Li et al. (2024)
3.09 %	Ji et al. (2021b)
2 %	Peng and Lu (2015)
1.78 %	Kurnaz et al. (2023)
1.77 %	**This work**

Table 4.3 Comparison of repeatability values reported in the literature and measured for the PeSkin architecture.

4.3.4 Time Response and Recovery Time

The dynamic performance of the PeSkin taxel was evaluated in terms of response time and recovery time by applying a step-like normal force with a minimum amplitude of 0.2 N. The force was rapidly applied and released using the same electromechanical platform described in Section 4.3.1, while the corresponding output variation Y (expressed as ΔRaw Count and ΔC) was recorded.

The response time (ΔT_{RES}) is defined as the time interval required for the sensor output to rise from its initial steady-state value to the maximum value reached after force application:

$$\Delta T_{\mathrm{RES}} = t_{\mathrm{RESmax}} - t_{\mathrm{RESmin}} \tag{4.8}$$

Similarly, the recovery time (ΔT_{REC}) is defined as the time interval required for the output to return from the maximum value to its baseline level after force release:

$$\Delta T_{\mathrm{REC}} = t_{\mathrm{RECmax}} - t_{\mathrm{RECmin}} \tag{4.9}$$

Figure 4.14 shows the dynamic response of the PeSkin taxel during force application and release. The measured response time is approximately 4.17 ms, while the recovery time is approximately 6.21 ms.

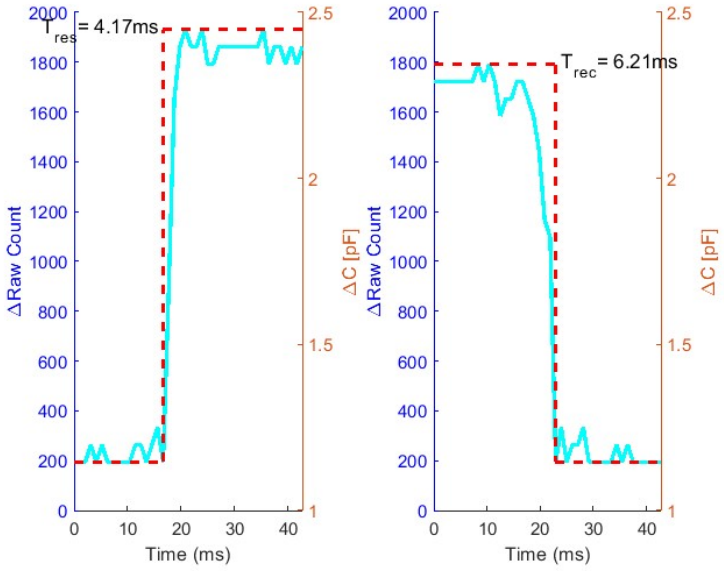

Figure 4.14 Dynamic characterization of a PeSkin taxel under a step-like force of 0.2 N. Left: response time measurement. Right: recovery time measurement.

The fast dynamic response can be attributed to the low mass and reduced bending stiffness of the 50 μm PET substrate combined with the air-gap transduction mechanism, which allows rapid mechanical deformation and recovery. The slightly longer recovery time is mainly associated with minor viscoelastic relaxation effects of the adhesive and tactile ink layers. Overall, the measured time constants demonstrate that the PeSkin architecture is suitable for dynamic interaction scenarios requiring rapid contact detection and release. Hereafter Table 4.4 show the comparison within the literature.

Response / Recovery Time	**Paper Reference**
54 ms	Dong et al. (2018)
200 ms	Yoon et al. (2017)
50 ms	Palaniappan et al. (2020)
6 ms	Zhang et al. (2022)
50 ms	Shuai et al. (2017)
27 ms	Wang et al. (2023a)
21 ms	Cheng et al. (2018)
600 ms / 1200 ms	Maddipatla et al. (2020)
12.5 ms / 37.5 ms	Xu et al. (2023)
100 ms / 200 ms	Cai et al. (2021)
36 ms	Xu et al. (2024b)
60 ms / 36 ms	Hou et al. (2024)
47 ms / 51 ms	Yin et al. (2024)
300 ms	Wang et al. (2023b)
100 ms	Choi et al. (2020)
112 ms / 152 ms	Li et al. (2024)
40 ms / 60 ms	Yu et al. (2023b)
100 ms	Ji et al. (2021a)
23 ms / 40 ms	Jin et al. (2024)
50 ms / 200 ms	Peng and Lu (2015)
86 ms / 93 ms	Nie et al. (2022)
20 ms	Peng et al. (2019)
15 ms	El-Molla et al. (2016)
40 ms	Viry et al. (2014)
62 ms / 77 ms	Xu et al. (2024c)
40 ms	Kumar et al. (2023)
60 ms / 54 ms	Yu et al. (2023a)
29 ms / 75 ms	Hailiang et al. (2024)
110 ms	Aubeeluck et al. (2024)
580 ms / 480 ms	Kurnaz et al. (2023)
75 ms / 93 ms	Zheng et al. (2024)
62 ms / 25 ms	Yan et al. (2024)
33 ms / 44 ms	Yu et al. (2024)
33 ms	Xie et al. (2022)
60 ms / 45 ms	Fu et al. (2021)
50 ms / 60 ms	Su et al. (2024)
15 ms / 14 ms	Wang et al. (2024)
4.17 ms / 6.21 ms	**This work**

Table 4.4 Comparison of response and recovery times reported in the literature and measured for the PeSkin architecture.

4.3.5 Dynamic Range

Dynamic range represents a critical performance metric for tactile sensors, particularly in robotic manipulation scenarios where both low-intensity contacts and higher interaction forces must be reliably detected. In digital acquisition systems, the dynamic range can be expressed in terms of the number of effective usable bits of the sensor output.
In this work, the dynamic range is evaluated according to the formulation introduced in Section 1.2:

$$DR_{\text{bits}} = \frac{20\log_{10}(RawCount_{\max} - RawCount_{\min})}{8} \tag{4.10}$$

where $RawCount_{\max}$ and $RawCount_{\min}$ represent the maximum and minimum measurable digits values within the operating pressure range. This formulation provides an estimate of the effective bit resolution of the sensing system.
To measure this metric the maximum supported pressure (60N) by the experimental machine presented in Section 4.3.1 was applied on a single taxel. Fig. 4.15 shows the measured response.

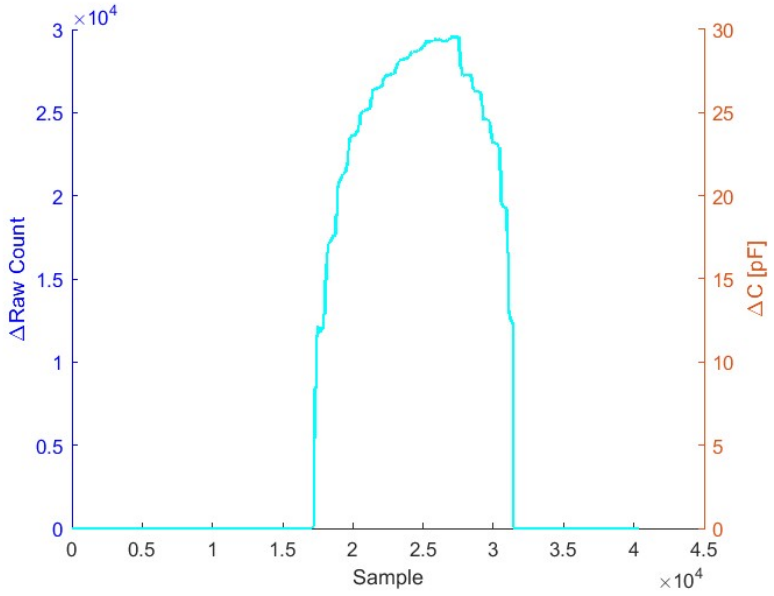

Figure 4.15 Response of the sensor under a pressure load of 60N to extract its dynamic range.

For the PeSkin architecture, the measured capacitance span between the minimum detectable force and the maximum applied load corresponds to an effective dynamic range of:

$$DR_{\text{PeSkin}} \approx 15 \text{ bits} \tag{4.11}$$

This high dynamic range is enabled by the air-gap capacitive transduction mechanism combined with the high-resolution digital acquisition provided by the PSoC-based readout architecture. The large measurable span ensures reliable detection of both gentle contacts and higher applied forces without saturation.
Table 4.5 reports a comparison between the dynamic range of PeSkin and representative values reported in the literature.

Dynamic range (tactile response span)	**Paper Reference**
10 bits	Maiolino et al. (2013)
12 bits	Dong et al. (2018)
12 bits	Wu et al. (2023)
14 bits	Cheng et al. (2023)
15 bits	**This work**

Table 4.5 Comparison of dynamic range values reported in the literature and measured for the PeSkin architecture.

4.3.6 Spatial Resolution

The spatial resolution of the PeSkin 6×24 array was evaluated by applying a localized normal force while progressively shifting the indenter position with a 1 mm step across adjacent taxels.
Figure 4.16 shows the output variation of neighboring taxels as a function of the indenter displacement. The response demonstrates well-localized activation with limited cross-talk between adjacent sensing elements, confirming that the 3.5 mm diameter taxel geometry and laminated PET–air-gap structure allow accurate contact localization.

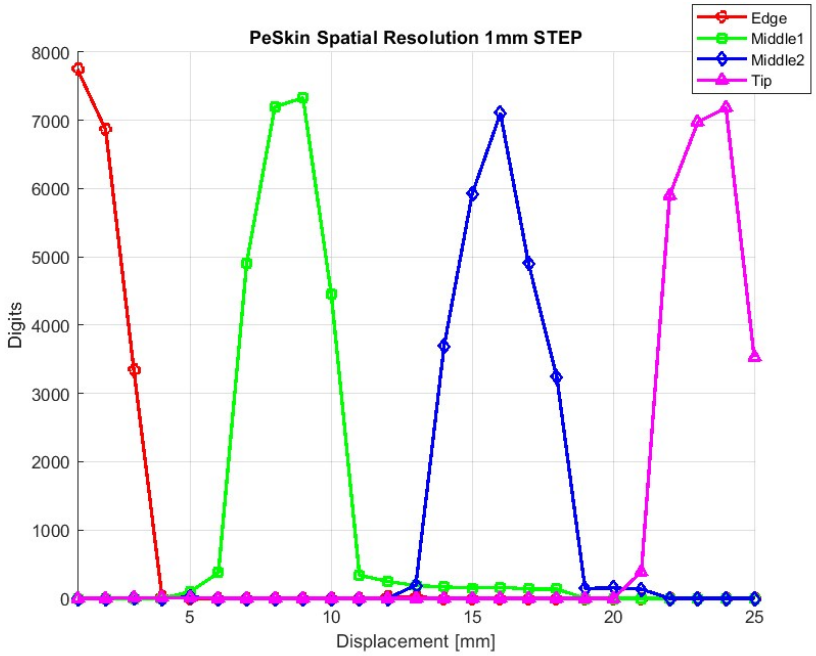

Figure 4.16 Spatial resolution evaluation of the PeSkin array with 1 mm displacement steps. The curves represent the response of adjacent taxels during localized force application.

4.4 PeSkin Integration Demonstrator

The experimental characterization presented in Section 4.3 demonstrated that the PeSkin architecture provides high sensitivity in the low-force regime, limited hysteresis and repeatability errors, fast response and recovery times, and an effective dynamic range of approximately 15 bits. These characteristics make the system suitable for robotic manipulation and safe physical human–robot interaction scenarios.
To validate its applicability in a realistic robotic configuration, a demonstrator was developed based on a cylindrical plastic cover designed for integration on a UR10e robotic arm. The demonstrator consists of a 3D-printed cylindrical structure (diameter $\approx$ 16 cm, height $\approx$ 17 cm) split into two halves to facilitate assembly and maintenance.
A total of 12 PeSkin patches (each 6×24 taxels) were mounted on the external surface of the cylinder, resulting in:

- 144 taxels per patch,
- 1728 taxels overall,
- a spatial geometrical resolution of approximately 2 taxels/cm^2,

Figure 4.17 shows the assembled cylindrical structure with the internal arrangement of the readout electronics.
Each PeSkin patch is connected to compact PSoC-based acquisition boards (30×30 mm), positioned on the inner surface of the cylinder. In total, 48 compact PCBs are used to acquire the 1728 taxels, following the modular architecture described in Section 4.2.4. The communication protocol adopted for data transmission is the same SPI master–slave configuration illustrated in Fig. 4.8, followed by UART communication toward a host computer for real-time visualization.
Unlike the ProxySKIN architecture presented in Chapter 3, this demonstrator does not employ the Intelligent Hub Board (IHB). Instead, the acquisition boards are directly interconnected through the SPI bus and managed by a master unit responsible for aggregating and forwarding data to the visualization interface.
Figure 4.18 shows an example of the demonstrator during operation, where distributed tactile activations are visualized in real time.

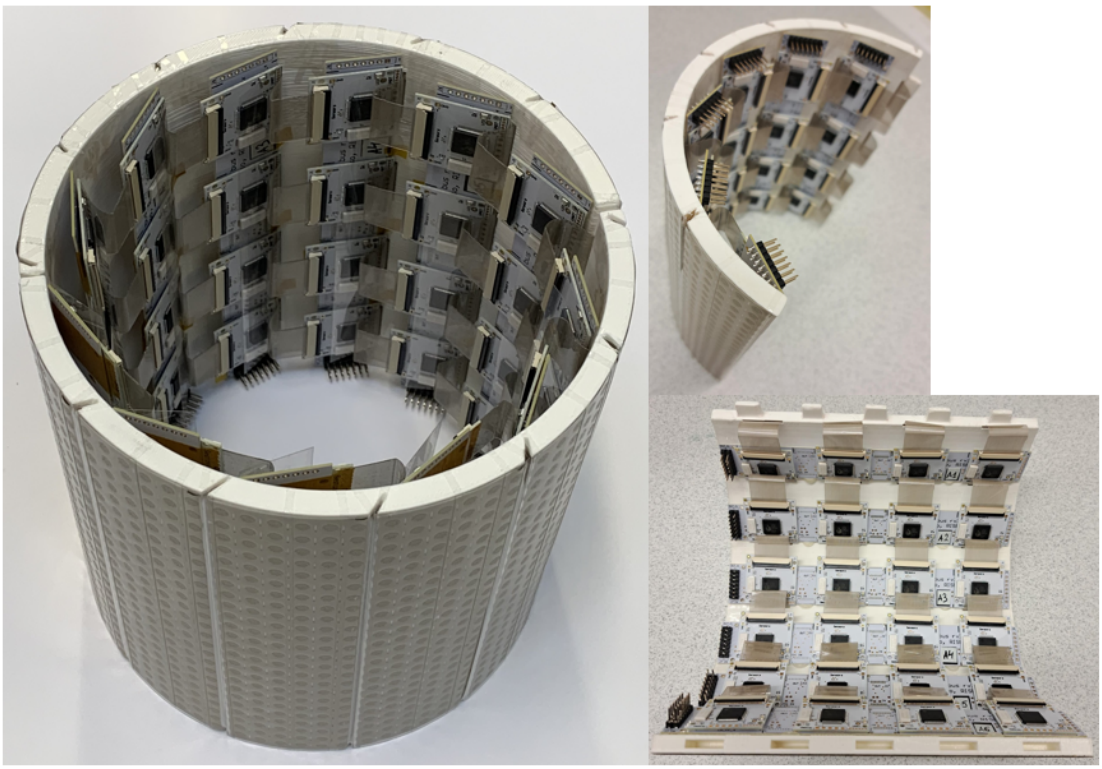

Figure 4.17 PeSkin cylindrical integration demonstrator. (a) External view of the assembled cover. (b) Internal view showing the arrangement of compact PSoC readout boards.

The cylindrical integration validates the mechanical flexibility of the 50 μm PET-based laminated structure and confirms the scalability of the modular electronic architecture. The system is capable of real-time distributed tactile acquisition over a curved surface without significant degradation of sensitivity or spatial resolution.
This demonstrator highlights the potential of PeSkin as a scalable, printable, and integrable tactile sensing solution for robotic covers and large-area physical interaction surfaces.

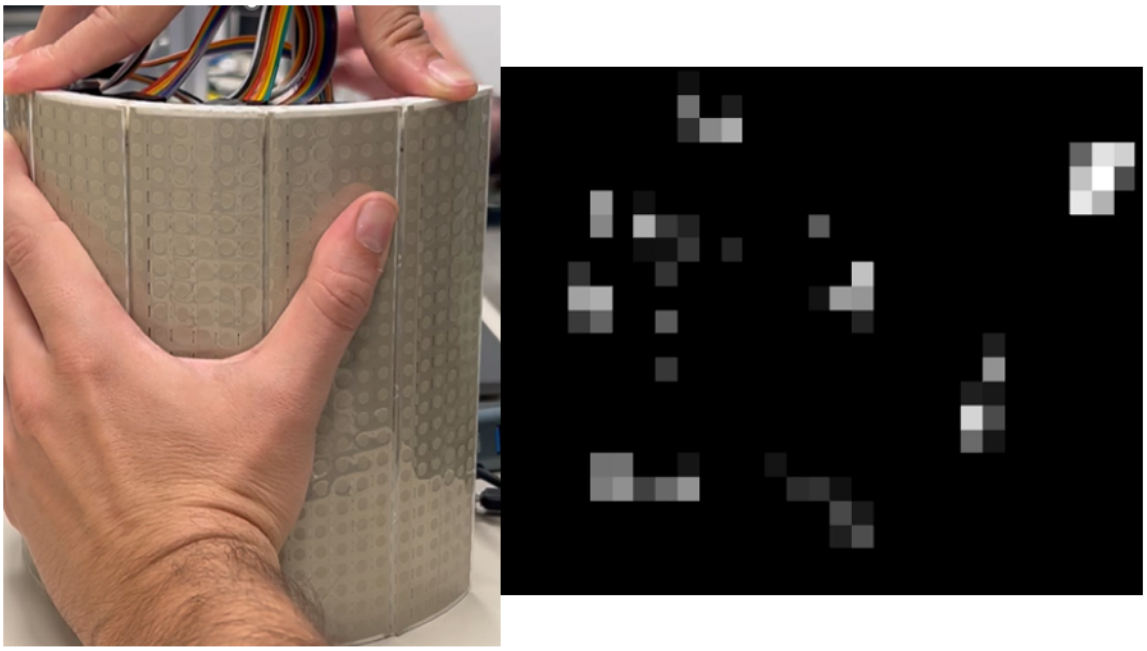

Figure 4.18 Example of the PeSkin cylindrical demonstrator during interaction. Left: physical interaction with the tactile surface. Right: real-time visualization of the activated taxels.

Chapter 5

Conclusions and Perspectives

5.1 PeSkin: Summary and Scientific Contributions

This doctoral research addressed the challenge introduced in Chapter 1: the development of scalable, printable, and mechanically compliant capacitive tactile sensing systems suitable for large-area robotic integration.
The work started from the need to bridge the gap between high-resolution laboratory prototypes and robust, integrable tactile architectures capable of operating on curved robotic surfaces while maintaining reliable mechanical-to-electrical transduction performance.
Three main technological contributions were achieved.
First, a screen-printed air-gap capacitive architecture was developed and experimentally validated. The proposed laminated PET–air-gap structure demonstrated:

- High sensitivity in the low-force regime (up to 5870 fF/N),
- Limited hysteresis (3.11%) and high repeatability (1.77%),
- Fast dynamic response (4.17 ms response time),
- Wide effective dynamic range ($\approx$ 15 bits),
- Reliable spatial resolution with limited cross-talk.

Second, a modular electronic acquisition architecture based on compact PSoC boards was designed and validated. The system demonstrated scalable multi-node acquisition through an SPI master–slave communication protocol, enabling real-time acquisition of distributed tactile data across large sensing surfaces.

Third, the integration feasibility of the proposed technology was validated through the realization of a cylindrical robotic demonstrator composed of 12 PeSkin patches (1728 taxels). This demonstrator confirmed:

- Mechanical adaptability of the 50 μm PET-based structure to curved surfaces,
- Scalability of the modular acquisition architecture,
- Real-time visualization capability for distributed tactile interaction.

Overall, this thesis contributes a complete pipeline—from material and transduction design to electronic architecture and system-level integration—toward printable, scalable, and robot-compatible tactile sensing systems.
The proposed technologies demonstrate that air-gap capacitive sensing, when combined with modular digital acquisition, represents a viable and competitive solution for large-area robotic tactile skins.

5.1.1 Future Developments on PeSkin

Although the PeSkin demonstrator validated the feasibility of large-area tactile integration on a cylindrical robotic cover, several developments are required to transition from laboratory prototype to fully integrated robotic skin.
A first technological improvement concerns the communication architecture. The current demonstrator employs an SPI master–slave configuration followed by UART transmission toward a host computer for visualization. While suitable for prototyping and experimental validation, UART communication introduces bandwidth and determinism limitations when considering full robotic integration.
A future implementation should replace the UART interface with an industrial real-time communication protocol such as EtherCAT. The adoption of EtherCAT would provide:

- Deterministic low-latency communication,
- Direct integration within industrial robotic control architectures,
- Scalability to high taxel counts without compromising update rate,
- Synchronization with robot motion control loops.

Such an upgrade would enable closed-loop tactile feedback directly at the robot controller level, allowing the tactile skin to actively contribute to collision detection, compliant manipulation, and safe human–robot interaction.
A second development concerns full robotic integration. The current demonstrator is a standalone cylindrical module inspired by the UR10e geometry but not mechanically integrated onto the robot. Future work will focus on:

- Mechanical fastening strategies compatible with robotic joints,
- Cable routing and strain-relief optimization,
- Integration on robots with complex geometries beyond cylindrical links.

In particular, adapting PeSkin to robots with non-uniform cross-sections and articulated segments will require flexible tiling strategies and modular patch segmentation. This idea was already taken into consideration by thinking on how to integrate PeSkin on a Franka Emika Panda robot manipulator.
Extending the architecture to complex-shaped robotic surfaces will represent a key step toward fully distributed tactile robotic skins capable of covering entire manipulators.

5.2 CySkin+: Summary and Scientific Contributions

CySkin+ represents the evolution of an already established distributed tactile architecture, enhanced and refined within this doctoral research to improve scalability, integration capability, and industrial compatibility.
While the original CySkin architecture provided a modular framework for large-area tactile sensing, this work introduced significant improvements both at the sensing layer and at the system architecture level.
A first contribution concerns the integration of EtherCAT as communication backbone. The adoption of an industrial real-time protocol enables:

- Deterministic and synchronized distributed acquisition,
- Direct compatibility with industrial robotic controllers,
- Reduced latency and improved reliability for large taxel networks,
- Seamless scalability toward extended robotic surfaces.

Compared to traditional serial communication approaches, EtherCAT significantly enhances the suitability of CySkin+ for industrial robotic deployment and closed-loop control applications.
A second contribution lies in the sensing layer fabrication process. The transition toward screen-printing and lamination techniques for the tactile layer simplifies mechanical integration onto robotic structures. Printing directly onto flexible substrates reduces assembly complexity, improves conformability, and enables more compact mechanical packaging.
Despite the simplified fabrication process, CySkin+ maintains robust sensing performance while reducing manufacturing costs and improving reproducibility. The lamination-based approach facilitates easier replacement, maintenance, and modular scalability.
Overall, CySkin+ combines an already validated distributed architecture with enhanced fabrication strategies and industrial-grade communication, strengthening its position as a scalable tactile sensing solution for robotic systems.

5.2.1 Future Developments on CySkin+

Although CySkin+ demonstrated improved scalability and industrial compatibility through EtherCAT-based communication and simplified laminated fabrication, further validation at the robotic system level remains necessary.
A primary future research direction concerns the implementation and testing of closed-loop control algorithms based on tactile feedback. While the architecture supports deterministic real-time acquisition, its integration within robotic control loops must be experimentally validated to assess:

- Stability and latency during dynamic interaction,
- Effectiveness in collision detection and compliant manipulation,
- Robustness under continuous operation.

Testing CySkin and CySkin+ under real robotic control scenarios will provide quantitative evaluation of their contribution to manipulation accuracy and safety.
In parallel, continued research on printable materials remains essential. The identification of low-cost, mechanically flexible, and durable conductive and dielectric inks would further improve manufacturability and long-term reliability. Optimizing printable materials may also enhance mechanical robustness while preserving sensitivity and conformability.
These developments will contribute to transitioning CySkin+ from a validated distributed sensing architecture to a fully industrial-ready tactile skin solution.

5.3 Multilayer Architectures: Summary and Scientific Contributions

A fundamental constraint discussed in Chapter 2 concerns the in-plane size of tactile sensing elements. Increasing sensitivity by enlarging the electrode area is often not feasible in robotic skin applications, where sensors must be densely distributed over curved and articulated surfaces. Therefore, improvements in sensing performance must be achieved without increasing the in-plane dimensions of the taxel.
Within this framework, multilayer capacitive architectures represent a strategic research direction addressed in this thesis.
The multilayer concept aims at enhancing sensitivity and dynamic range by stacking multiple functional layers vertically rather than expanding the sensor footprint. By introducing additional dielectric interfaces and controlled air-gap structures across multiple stacked layers, it becomes possible to:

- Increase effective capacitance variation under small applied forces,
- Improve signal-to-noise ratio without enlarging electrode area,
- Extend the dynamic range through multi-stage mechanical deformation.

This vertical design approach directly addresses the geometric constraints imposed by robotic integration while maintaining compact taxel dimensions.
Another key contribution of multilayer architectures lies in the introduction of vertical interconnect strategies. The implementation of printed vertical vias enables electrical routing through stacked layers, paving the way for more compact sensor-to-electronics integration. Such solutions could significantly reduce lateral routing complexity and facilitate direct integration with acquisition electronics beneath the sensing layer.
Overall, the multilayer approach provides a pathway toward higher-performance tactile elements that remain compatible with high-density robotic skins. By exploiting the vertical dimension rather than the planar one, it offers a scalable method to enhance performance while respecting the strict geometric constraints of robotic applications.

5.3.1 Future Developments on Multilayer Architectures

The next development step for multilayer architectures concerns the integration of dedicated readout electronics directly within or beneath the stacked sensing structure.
The introduction of vertical interconnects enables compact electrical routing and opens the possibility of embedding acquisition circuitry closer to the sensing layer. This integration would reduce parasitic effects, improve signal integrity, and allow further miniaturization of the tactile module.
Following electronic integration, a complete experimental characterization will be required to evaluate the effective gains in sensitivity, dynamic range, and noise performance introduced by the multilayer configuration. Mechanical robustness under repeated bending and long-term loading conditions will also need to be assessed.
A subsequent validation stage will involve integration on robotic fingertips, where geometric constraints are particularly severe and high spatial resolution is required. Fingertip deployment represents a critical benchmark for high-performance tactile sensing, as it demands compact size, mechanical compliance, and reliable dynamic behavior.
Finally, due to its intrinsic flexibility and vertical scalability, the multilayer approach may be extended to both small-area high-resolution sensing (e.g., robotic fingertips) and larger distributed surfaces. This dual applicability highlights its potential as a versatile next-generation tactile architecture adaptable to multiple robotic platforms.

5.4 Overall Synthesis and Outlook

The three research topics presented in this thesis — *Multilayer Capacitive Architectures, CySkin+, and PeSkin* — address different but complementary aspects of the same problem: develop high-performance tactile sensing at the scale required by robotic skin applications. ***Multilayer Stacking*** provides a strategy to enhance sensitivity within a compact taxel footprint. ***CySkin+*** demonstrates that an established distributed architecture can be upgraded through material substitution and industrial-grade communication without sacrificing sensing reliability. ***PeSkin*** shows that screen printing and lamination can produce large-area tactile patches with competitive performance and straightforward integration on curved surfaces.
Taken together, these contributions support three key conclusions:

- Capacitive air-gap transduction combined with printed fabrication offers a viable route toward scalable robotic skins that balance sensitivity, robustness, and manufacturability.

- Vertical stacking and substrate selection provide effective and independent tuning mechanisms for tailoring sensor performance to application-specific requirements.
- The adoption of deterministic real-time communication protocols is essential to preserve signal integrity and synchronization as the number of distributed sensing elements grows.

Beyond tactile sensing for robotics, several elements of this work have potential applicability in other domains. The analytical model for vertically stacked capacitive structures is not restricted to tactile transduction and could be extended to other sensing modalities where parallel mechanical compliance is exploited. Similarly, the EtherCAT-based distributed acquisition framework is not tied to a specific sensing technology and could support heterogeneous sensor networks in industrial monitoring, wearable systems, or structural health sensing. Exploring these directions would broaden the impact of the methodologies developed in this thesis and is considered as a long-term research perspective. Furthermore, the proposed technologies could be applied in other fields aligned with the DRIM curricula, such as agricultural monitoring systems and healthcare devices.

References

Aeby, X., von Dommelen, R., and Briand, D. (2019). Fully fdm 3d printed flexible capacitive and resistive transducers. In *2019 20th International Conference on Solid-State Sensors, Actuators and Microsystems & Eurosensors XXXIII (TRANSDUCERS & EUROSENSORS XXXIII)*, pages 2440–2443.

Ali, S., Maddipatla, D., Narakathu, B. B., Chlaihawi, A. A., Emamian, S., Janabi, F., Bazuin, B. J., and Atashbar, M. Z. (2019). Flexible capacitive pressure sensor based on pdms substrate and ga–in liquid metal. *IEEE Sensors Journal*, 19(1):97–104.

Alshawabkeh, M., Alagi, H., Navarro, S. E., Duriez, C., Hein, B., Zangl, H., and Faller, L. M. (2023). Highly stretchable additively manufactured capacitive proximity and tactile sensors for soft robotic systems. *IEEE Transactions on Instrumentation and Measurement*, 72:1–10.

Aubeeluck, D. A., Forbrigger, C., Taromsari, S. M., Chen, T., Diller, E., and Naguib, H. E. (2024). Screen-printed capacitive tactile sensor for monitoring tool-tissue interactions and grasping performances of a surgical magnetic microgripper. *ACS Applied Materials & Interfaces*, 6(9):1698–1706.

Bacher, E., Cartiel, S., García-Pueyo, J., Stopar, J., Zore, A., Kamnik, R., Aulika, I., Ogurcovs, A., Grūbe, J., Bundulis, A., Butikova, J., Kemere, M., Muñoz, A., and Laurenzis, M. (2024). OptoSkin: Novel LIDAR touch sensors for detection of touch and pressure within wave guides. *IEEE Sensors Journal*, 24(20):33268–33280.

Baglini, E., Cannata, G., and Mastrogiovanni, F. (2010). Design of an embedded networking infrastracture for whole-nody tactile sensing in humanoid robots. In *2010 10th IEEE-RAS International Conference on Humanoid Robots*, pages 671–676.

Baglini, E., Youssefi, S., Mastrogiovanni, F., and Cannata, G. (2014). A real-time sidtributed architecture for large-scale tactile sensing. In *2014 IEEE/RSJ International Conference on Intelligent Robots and Systems*.

Bai, N., Xue, Y., Chen, S., Shi, L., Shi, J., Zhang, Y., Hou, X., Cheng, Y., Huang, K., Wang, W., Zhang, J., liu, Y., and Fei Guo, C. (2023). A robotic sensory system with high spatiotemporal resoultion for texture recognition. *Nature Communications*, 14(7121).

Bergner, F., Dean-Leon, E., and Cheng, G. (2016). Event-based signaling for large-scale artificial robotic skin - realization and performance evaluation. In *2016 IEEE/RSJ International Conference On Intelligent Robots and Systems (IROS)*, pages 4918–4924.

Cai, M., Zhongdong, J., Shuang, N., Chengjun, W., Jun, Z., and Jizhou, S. (2021). A multifunctional electronic skin based on patterned metal films for tactile sensing with a broad linear response range. *Science Advances*, 7(53).

Cannata, G., Maggiali, M., Metta, G., and Sandini, G. (2008). An embedded artificial skin for humanoid robots. In *2008 IEEE International Conference on Multisensor Fusion and Integration for Intelligent Systems*, pages 434–438.

Chandra, M., Ke, S. Y., Chen, R., and Lo, C. Y. (2017). Vertically stacked capacitive tactile sensor with more than quadrupled spatial resolution enhancement from planar arrangement. *Sensors and Actuators A: Physical*, 263:386–390.

Chen, S., Li, M., Huang, Y., Xu, H., Gu, G., and Guo, X. (2020). Matrix-adressed flexible capacitive pressure sensor with suppressed crosstalk for artificial electronic skin. *IEEE Transactions on Electron Devices*, 67(7):2940–2944.

Cheng, G., Dean-Leon, E., Bergner, F., Rogelio Guadarrama Olvera, J., Leboutet, Q., and Mittendorfer, P. (2019). A comprehensive realization of robot skin: Sensor, sensing, control and applications. *Proceedings of the IEEE*, 107(10):2034–2051.

Cheng, J., Mu, Y., Li, L., Wang, M., Yue, C., Yang, W., Liu, C., and Dong, L. (2023). A four-capacitor tactile sensor based on bump structure and compensating method to reduce inertial interference for robotic tactile sensing. *IEEE Sensors Journal*, 23(18):21670–21678.

Cheng, M. Y., Huang, X. H., Ma, C. W., and Yang, Y. J. (2009). A flexible capacitive tactile sensing array with floating electrodes. *Journal of Micromechanics and Microengineering*, 19(11).

Cheng, W., Wang, J., Ma, Z., Yan, K., Wang, Y., Wang, H., Li, S., Li, Y., Pan, L., and Shi, Y. (2018). Flexible pressure sensor with high sensitivity and low hysteresis based on a hierarchically microstructured electrode. *IEEE Electron Device Letters*, 39(2):288–299.

Choi, J., Kwon, D., Kim, K., Park, J., Del Orbe, D., Gu, J., Ahn, J., Cho, I., Jeong, Y., Oh, Y., and Park, I. (2020). Synergetic effect of porous elastomer and percolation of carbon nanotube filler toward high performance capacitive pressure sensors. *ACS Applied Materials & Interfaces*, 12(1):1698–1706.

Dahiya, R. S., Metta, G., Valle, M., and Sandini, G. (2010). Tactile sensing-from humans to humanoids. *IEEE Transactions on Robotics*, 26(1):1–20.

Delgado, R., Kim, S. Y., You, B. J., and Choi, B. W. (2016). An ethercat-based real-time motion control system in mobile robot application. In *2016 13th International Conference on Ubiquitous Robots and Ambient Intelligence (URAI)*, pages 710–715.

Dong, X., Wei, Y., Chen, S., Lin, Y., Liu, L., and Li, J. (2018). A linear and large-range pressure sensor based on a graphene/silver nanowires nanobiocomposites network and a hierarchical structural sponge. *Composites Science and Technology*, 155:108–116.

El-Molla, S., Albrecht, A., Cagatay, E., Mittendorfer, P., Cheng, G., Lugli, P., Salmerón, J. F., and Rivadeneyra, A. (2016). Integration of a thin film pdms-based capacitive sensor for tactile sensing in an electronic skin. *Journal of Sensors*.

Eshkeiti, A., Emamian, S., Avathu, S. G. R., Narakathu, B. B., Joyce, M. J., Joyce, M. K., Bazuin, B. J., and Atashbar, M. Z. (2014). Screen printed flexible capacitive pressure sensor. In *SENSORS, 2014 IEEE*, pages 1192–1195.

EtherCAT Technology Group (2023). Ethercat technology overview. https://www.ethercat.org. Accessed: 2024-03-01.

European Horizon Project (2025). Sestosenso. https://sestosenso.eu/.

Fu, X., Zhang, J., Xiao, J., Kang, Y., Yu, L., Jiang, C., Pan, Y., Dong, H., Gao, S., and Wang, Y. (2021). A high-resolution, ultrabroad-range and sensitive capacitive tactile sensor based on a cnt/pdms composite for robotic hands. *Nanoscale*, 13(44):18780–18788.

Giovinazzo, F., Grella, F., Sartore, M., Adami, M., and Galletti, R. (2024a). From cyskin to proxyskin: Design, implementation and testing of a multi-modal robotic skin for human-robot interaction. *Sensors*, 24(4).

Giovinazzo, F., Perri, A., Staiano, M., Grella, F., Sartore, M., Adami, M., Galletti, R., and Cannata, G. (2024b). Design, implementation and testing of an ethercat-based network for multi-modal distributed sensing architectures. In *2024 IEEE 20th International Conference on Automation Science and Engineering (CASE)*, pages 830–837.

Hailiang, M., Yixiao, S., Junjie, P., and Guanjun, B. (2024). Flexible tactile sensor arrays with capacitive and resistive dual-mode transduction. *IEEE Sensors Journal*, 24(10):15892–15899.

Hao, W., Guo, J., Wang, C., Wang, S., and Shi, C. (2020). A novel capacitive-based flexible pressure sensor based on stretchable composite electrodes and a dielectric elastomer with microstructures. *Microelectronic Engineering*, 8:142810–142818.

Hou, M., Hong, W., Chen, H., Zhang, T., Zhu, X., Hao, J., Yin, Z., Yan, Z., Li, X., and Zhang, A. (2024). Simple fabrication of high-sensitivity capacitive tactile sensor based on a polydimethylsiloxane dielectric layer using a biomimetic gray kangaroo leg structure. *Journal of Physics D: Applied Physics*, 57(21).

Jagoda, A., Dobrzynska, M., and Gijs, A. M. (2012). Flexible polyimide-based force sensor. *Sensors and Actuators A: Physical*, 173(1):127–135.

Jen, Y. H., Mo, C. T., Chen, Y. W., Martincic, E., Yamane, D., Chang, T. F. M., Sone, M., and Lo, C. Y. (2021). Development and characterization of vertically stacked tactile sensor with hollow structure. *IEEE Sensors Journal*, 21(5):5809–5818.

Ji, B., Zhou, Q., Lei, M., Ding, S., Song, Q., Gao, Y., Li, S., Xu, Y., Zhou, Y., and Zhou, B. (2021a). Gradient architecture-enabled capacitive tactile sensor with high sensitivity and ultrabroad linearity range. *Nano-Micro Small*, 17(43).

Ji, B., Zhou, Q., Lei, M., Ding, S., Song, Q., Gao, Y., Li, S., Xu, Y., Zhou, Y., and Zhou, B. (2021b). Soft capacitive tactile sensing array with high-robustness for three-axis pressure measurement. *Measurement*, 223.

Jin, Q., Wang, C., Wu, H., Luo, X., Li, J., Ma, G., Li, Y., Luo, C., Guo, F., and Long, Y. (2024). 3d printing of capacitive pressure sensors with tuned wide detection range and high sensitivity inspired by bio-inspired kapok structures. *Macro Molecular Rapid Communications*, 45(9).

Kappassov, Z., Corrales, J. A., and Perdereau, V. (2015). Tactile sensing in dexterous robot hands - review. *Robotics Autonomous Systems*, 74:195–220.

Kosmas, D., von Jonberger, H. P., Schouten, M., Abayazid, M., and Krijnen, G. (2021). Development of a 3d printed gap gauge with embedded force sensor for balancing unicompartmental knee arthroplasty. In *2021 IEEE Sensors*, pages 1–4.

Kumar, S., Yadav, S., and Kumar, A. (2023). Flexible mesostructured capacitive pressure sensor for blood pressure monitoring. In *2023 IEEE Sensors*, pages 1–4.

Kurnaz, S., Oztürk, O., Mehmet, A. H., Guduloglu, U., Yilmaz, N., and Cicek, O. (2023). Flexible capacitive and piezoresistive pressure sensor based on screen-printed parylene c/polyurethene composites in low-pressure range. *Flexible and Printed Electronics*, 8(3).

LaCroix, A. S., Duenwald-Kuehl, S. E., Lakes, R. S., and Vanderby, R. (2013). Relationship between tendon stiffness and failure: A metaanalysis. *Journal of Applied Physiology*, 115(1):43–51.

Lee, H. K., Chang, S. I., and Yoon, E. (2006). A flexible polymer tactile sensor: Fabrication and modular expandability for large area deployment. *Journal of Microelectromechanical Systems*, 15(6):1681–1686.

Lee, H. K., Chung, J., Chang, S. I., and Yoon, E. (2008). Normal and shear force measurement using a flexible polymer tactile sensor with embedded multiple capacitors. *Journal of Microelectromechanical Systems*, 17(4):934–942.

Lee, U. G., Kim, W. B., Han, D. H., and Chung, H. S. (2019). A modified equation for thickness of the film fabricated by spin coating. *Symmetry*, 11(9).

Li, R., Zhou, Q., Bi, Y., Cao, S., Xia, X., Yang, A., Li, S., and Xiao, X. (2021). Research progress of flexible capacitive pressure sensor for sensitivity enhancement approaches. *Sensors and Actuators A: Physical*, 321.

Li, Z., Zhao, K., Wang, J., Wang, B., Lu, J., Jia, B., Ji, T., Han, X., Luo, G., Yu, Y., Wang, L., Li, M., Wang, Z., and Zhao, L. (2024). Sensitive, robust, wide-range, and high-consistency capacitive tactile sensors with ordered porous dielectric microstructures. *ACS Applied Materials & Interfaces*, 16(6):7384–7398.

Liu, F., Deswal, S., Christou, A., Sandamirskaya, Y., Kaboli, M., and Dahiya, R. (2022). Neuro-inspired electronic skin for robots. *Science Robotics*, 7(67).

Luo, S., Lepora, N. F., Yuan, W., Althoefer, K., Cheng, G., and Dahiya, R. (2025). Tactile robotics: An outlook. *IEEE Transactions on Robotics*, 41:5564–5583.

Lü, X., Bao, W., Wang, S., Tao, Y., Yang, J., Jiang, L., Li, X., Xie, X., and Chen, R. (2017). Three-dimensional interfacial stress decoupling method for rehabilitation therapy robot. *IEEE Transactions on Industrial Electronics*, 64(5):3970–3977.

Ma, S., Dahiya, A. S., and Dahiya, R. (2023). Out-of-plane electronics on flexible substrates using inorganic nanowires grown on high-aspect-ratio printed gold micropillars. *Advanced Materials*, 35(26).

Maddipatla, D., Narakathu, B. B., Ali, M. M., Chlaihawi, A. A., and Atashbar, M. Z. (2017). Development of a novel carbon nanotube based printed and flexible pressure sensor. In *2017 IEEE Sensors Applications Symposium (SAS)*, pages 1–4.

Maddipatla, D., Zhang, X., Bose, A. K., Masihi, S., Narakathu, B. B., Bazuin, B. J., Williams, J. D., Mitchell, M. F., and Atashbar, M. Z. (2020). A polyimide based force sensor fabricated using additive screen-printing process for flexible electronics. *IEEE Access*, 8:207813–207821.

Maiolino, P., Maggiali, M., Cannata, G., Metta, G., and Natale, L. (2013). A flexible and robust large scale capacitive tactile system for robots. *IEEE Sensors Journal*, 13(10):3910–3917.

Meribout, M., Abule Takele, N., Derege, O., Rifiki, N., El Khalil, M., Tiwari, V., and J-Zhong (2024). Tactile sensors: A review. *Measurement*, 238.

Mikkonen, R., Puistola, P., Jönkkäri, I., and Mäntysalo, M. (2020). Inkjet printable polydimethylsiloxane for all-inkjetprinted multilayered soft electrical applications. *ACS Applied Materials & Interfaces*, 12(10):11990–11997.

Mishra, R. B., El-Atab, N., Hussain, A. M., and Hussain, M. M. (2021). Recent progress on flexible capacitive pressure sensors: From design and materials to applications. *Advanced Material Technology*, 6(4).

Mittendorfer, P. and Cheng, G. (2011). Humanoid multimodal tactile-sensing modules. *IEEE Transaction on Robotics*, 27(3):401–410.

Mittendorfer, P., E., and G, C. (2015). Realizing whole-body tactile interactions with a self-organizing, multi-modal artificial skin on humanoid robot. *Advanced Robotics*, 29(1):51–67.

Mittendorfer, P., Yoshida, E., Moulard, T., and Cheng, G. (2013). A general tactile approach for grasping unknown objects with a humanoid robot. In *2013 IEEE/RSJ International Conference On Intelligent Robots and Systems (IROS)*, pages 4747–4752.

Momota, M. R., Ferdous, T., Fujiwara, T., and Morshed, B. (2023). Fabrication and characterization of flexible solid-state mim supercapacitor with inkjet-printing of stacked ag np and polymer dielectric layers. In *2023 IEEE 16th Dallas Circuits and Systems Conference (DCAS)*, pages 1–5.

Narakathu, B. B., Eshkeiti, A., Reddy, A. S. G., Rebros, M., Rebrosova, E., Joyce, M. K., Bazuin, B. J., and Atashbar, M. Z. (2012). A novel fully printed and flexible capacitive pressure sensor. In *2012 IEEE Sensors*, pages 1–4.

Nie, L., Zhang, L., Di, X., Liu, Q., Zhang, Z., Zhou, Q., Dong, Z., Song, Z., Zhang, S., and Pan, G. (2022). Assembly of highly sensitive capacitive flexible pressure sensor based on bto nws -tpu porous composites film. *Vacuu,*, 205.

Ntagios, M., Nassar, H., Pullanchiyodan, A., Navaraj, W. T., and Dahiya, R. (2020). Robotic hands with intrinsic tactile sensing via 3d printed soft pressure sensors. *Advanced Intelligent Systems*, 2(6).

Palaniappan, V., Masihi, S., Panahi, M., Maddipatla, D., Bose, A. K., Zhang, X., Narakathu, B. B., Bazuin, B. J., and Atashbar, M. Z. (2020). Laser-assisted fabrication of a highly sensitive and flexible micro pyramid-structured pressure sensor for e-skin applications. *IEEE Sensors Journal*, 20(14):7605–7613.

Peng, J. Y. and Lu, M. S. C. (2015). A flexible capacitive tactile sensor array with cmos readout circuits for pulse diagnosis. *IEEE Sensors Journal*, 15(2):1170–1177.

Peng, S., Chen, S., Huang, Y., Pei, S., and Guo, X. (2019). High sensitivity capacitive pressure sensor with bi-layer porous structure elastomeric dielectric formed by a facile solution based process. *IEEE Sensors Letters*, 3(2):1–4.

PSoC CapSense Guide (2021). Psoc4 and psoc6 mcu capsense design guide. https://www.infineon.com/assets/row/public/documents/30/42/infineon-an85951-psoc-4-psoc-6-capsense-design-guide-applicationnotes-en.pdf. Accessed: 2021-10-01.

Ramalingame, R., Lakshmanan, A., Müller, F., Thomas, U., and Kanoun, O. (2019). Highly sensitive capacitive pressure sensors for robotic applications based on carbon nanotubes and pdms polymer nanocomposite. *Journal of Sensors and Sensor Systems*, 8(1):87–94.

Rana, A., Roberge, J. P., and Duchaine, V. (2016). Sensitive, robust, wide-range, and high-consistency capacitive tactile sensors with ordered porous dielectric microstructures. *IEEE Sensors Journal*, 16(22):7853–7863.

Salim, A. and Lim, S. (2017). Review of recent inkjet-printed capacitive tactile sensors. *Sensors*, 17(11).

Sethumadhavan, V., Saraf, S., Choudhari, A., and Gaikwad, R. (2017). Flexible capacitive based printed sensor using different dielectrics for real time applications. In *2017 International Conference on Trends in Electronics and Informatics (ICEI)*, pages 32–36.

Shi, J., Dai, Y., Cheng, Y., Xie, S., Li, G., Liu, Y., Wang, J., Zhang, R., Bai, N., Cai, M., Zhang, Y., Zhan, Y., Yu, C., and Fei Guo, C. (2023). Embedment of sensing elements for robust, highly sensitive, and cross-talk-free iontronic skins for robotics applications. *Science Advances*, 9(9).

Shu, Q., Pang, Y., Li, Q., Gu, Y., Liu, Z., Liu, B., Li, J., and Li, Y. (2024). Flexible resistive tactile pressure sensors. *Journal of Materials Chemistry A*, 12:9296–9321.

Shuai, X., Zhu, P., Zeng, W., Hu, Y., Liang, X., Zhang, Y., Sun, R., and Wong, C. P. (2017). Highly sensitive flexible pressure sensor based on silver nanowires-embedded polydimethylsiloxane electrode with microarray structure. *ACS Applied Materials & Interfaces*, 9(31):26314–26324.

Staiano, M., Baldini, G., Grella, F., Frascio, M., Maiolino, P., and Cannata, G. (2023). Mathematical model and experimental characterization of vertically stacked capacitive tactile sensors. *IEEE Sensors Journal*, 23(18):21341–21354.

Su, S., Zhang, X., Dang, D., Wang, Z., and Tong, Z. (2024). A high-performance flexible capacitive pressure sensor with 3-d printed hemispherical graded microstructures. *IEEE Sensors Journal*, 24(5):5966–5975.

System, B. I. (2023). Synchronization modes of an ethercat slave. https://infosys.beckhoff.com/english.phpcontent=./content/1033/ethercatsystem/2469122443.html&id=.

Thorlabs, I. (2024). Operating manual for the nrt150 motorized linear translation stage. *NRT Series Motorized Translation Stage User Guide*.

Viry, L., Levi, A., Totaro, M., Mondini, A., Mattoli, V., Mazzolai, B., and Beccai, L. (2014). Flexible three-axial force sensor for soft and highly sensitive artificial touch. *Advanced Materials*, 26(17).

Wang, C. C., Hung, C. H., Chen, Y. W., and Lo, C. Y. (2025). Force sensor for multiphysical quantity detection and its validation through random test. *IEEE Sensors Journal*, 25(13):23692–23699.

Wang, D., Zhao, N., Yang, Z., Yuan, Y., Xu, H., Wu, G., Zheng, W., Ji, X., Bai, N., Wang, W., Xue, C., and Gao, L. (2023a). Iontronic capacitance-enhanced flexible three-dimensional force sensor with ultrahigh sensitivity for machine-sensing interface. *IEEE Electron Device Letters*, 44(12):2023–2026.

Wang, H. L., Chen, T., Zhang, B., Wang, G., Yang, X., Wu, K., and Wang, Y. (2023b). A dual-responsive artificial skin for tactile and touchless interfaces. *Nano-Micro Small*, 19(21).

Wang, L., Guoli, M., and Wang, J. (2011). Implementing for networked motion control system with large-capacity data acquisition. *Procedia Engineering*, 15:28–32.

Wang, S., Gao, F., Hu, Y., Zhang, S., Shang, H., Ge, C., Tan, B., Zhang, X., Zhang, J., and Hu, P. (2024). Skin-inspired tactile sensor based on gradient pore structure enable broad range response and ultrahigh pressure resolution. *Chemical Engineering Journal*, 443(1).

Wolternik, G., Sanders, R., and Krijnen, G. (2018). Thin, flexible, capacitive force sensors based on anisotropy in 3d-printed structures. In *2018 IEEE Sensors*, pages 1–4.

Wu, J. Y., Hsu, T. Y., Ahmad, G., Malik, S., and Lo, C. Y. (2023). Novel multiaxial force decoupling strategy in vertically stacked force sensors with hybrid fabrication techniques. *IEEE Sensors Journal*, 23(124):30135–30142.

Xie, Y., Lin, L., Lu, L., Liang, Q., and Zhang, B. (2022). Flexible interfacial capacitive pressure sensor based on randomly distributed micro-pits electrode. *IEEE Transactions on Instrumentation and Measurement*, 71:1–9.

Xu, B., Zhong, L., Zhang, G., Liang, X., Virtue, D., Madan, R., and Bhattacharjee, T. (2024a). Cushsense: Soft, stretchable, and comfortable tactile-sensing skin for physical human-robot interaction. In *2024 IEEE International Conference on Robotics and Automation (ICRA)*, pages 5694–5701.

Xu, D., Hong, W., Hu, B., Zhang, T., Chen, D., Yan, Z., Yao, X., Zhang, X., Zhao, Y., and Sun, T. (2024b). River valley-inspired, high-sensitivity, and rapid-response capacitive three-dimensional force tactile sensor based on u-shaped groove structure. *Smart Materials and Structures*, 33(3).

Xu, W., Sun, J., Nie, L., Yang, L., Di, X., Zhang, L., Zhou, Q., and Pan, G. (2024c). Mxene porous nanocomposite based capacitive pressure sensor with high performance for human motion monitoring. *IEEE Sensors Journal*, 24(5):5915–5927.

Xu, Z., Wu, D., Chen, Z., Wang, Z., Cao, C., Shao, X., Zhou, G., Zhang, S., Wang, L., and Sun, D. (2023). A flexible pressure sensor with highly customizable sensitivity and linearity via positive design of microhierarchical structures with a hyperelastic model. *Microsystems & Nanoengineering*, 9(5).

Yan, Z., Zhang, H., Hu, B., Yao, X., He, J., Zhang, X., Zhu, S., Li, X., Hong, W., Hong, Q., Zhao, Y., Xu, Y., and Guo, X. (2024). High-linearity capacitive 3-d force-flexible tactile sensor inspired by mushroom structure for human motion monitoring and robotic gripping. *IEEE Sensors Journal*, 24(17):27309–27317.

Yang, M. J., Chung, H., Kim, Y., Park, K., and Kim, J. (2025). A body-scale robotic skin using distributed multimodal sensing modules: Design, evaluation, and application. *IEEE Transactions on Robotics*, 41(37):96–109.

Yin, A., Chen, R., Yin, R., Zhou, S., Ye, Y., Wang, Y., Wang, P., Qi, X., Liu, H., Liu, J., Yu, S., and Wei, J. (2024). An ultra-soft conductive elastomer for multifunctional tactile sensors with high range and sensitivity. *Materials Horizons*, 11:1975–1988.

Yoon, J. I., Choi, K. S., and Chang, S. P. (2017). A novel means of fabricating microporous structures for the dielectric layers of capacitive pressure sensor. *Microelectronic Engineering*, 179:60–66.

Yu, H., Guo, H., Wang, J., Zhao, T., Zou, W., Zhou, P., Xu, Z., Zhang, Y., Zheng, J., Zhong, Y., Wang, X., and Liu, L. (2023a). Skin-inspired capacitive flexible tactile sensor with an asymmetric structure for detecting directional shear forces. *Advanced Science*, 11(6).

Yu, J., Yao, S., Li, X., Ghaffar, A., and Yao, Z. (2024). Design of a 3-d tactile sensing array for incipient slip detection in robotic dexterous manipulation. *IEEE Transactions on Instrumentation and Measurement*, 73:1–14.

Yu, J., Yao, S., Li, X., Ghaffar, A., Zhang, Y., Jiang, X., Lin, H., and Yao, Z. (2023b). Soft capacitive tactile sensing array with high-robustness for three-axis pressure measurement. *Measurement*, 223.

Zhang, Y., Yang, J., Hou, X., Li, G., Wang, L., Bai, N., Cai, M., Zhao, L., Wang, Y., Zhang, J., Chen, K., Wu, X., Yang, C., Dai, Y., Zhang, Z., and Fei Guo, C. (2022). Highly stable flexible pressure sensors with a quasi-homogeneous composition and interlinked interfaces. *Nature Communications*, 13(1317).

Zheng, W., Liu, K., Guo, D., Yang, W., Zhu, J., and Liu, H. (2024). A large-area tactile sensor for distributed force sensing using highly sensitive piezoresistive sponge. In *2024 IEEE International Conference on Robotics and Automation (ICRA)*, pages 1063–1069.

Zhiyu, Y., Wenjie, W., Fengxian, G., Min, G., Liang, Z., Dongrui, W., Baochun, G., Liqun, Z., and Xiang, L. (2025). Flexible tactile sensing systems: Challenges in theoretical research tramsferring to practical applications. *Nano-Micro Letters*, 18(37).

Zhou, Y., Zhao, J., Lu, P., Wang, Z., and He, B. (2024). Tacsuit: A wearable large-area, bionispired multimodal tactile skin for collaborative robots. *IEEE Transactions on Industrial Electronics*, 71(2):1708–1717.

Zhu, Y., Chen, X., Chu, K., Wang, X., Hu, Z., and Su, H. (2022). Carbon black/pdms based flexible capacitive tactile sensor for multi-directional force sensing. *Sensors*, 22(2).

Zhu, Y. and Tairych, A. (2021). Using a flexible substrate to enhance the sensitivity of dielectric elastomer force sensors. *Sensors and Actuators A: Physical*, 332(2).